

A SATELLITE STUDY OF
DC ELECTRIC FIELD REVERSALS
IN THE MAGNETOSPHERE*

by

David Paul Cauffman

A thesis submitted in partial fulfillment of the
requirements for the degree of Doctor of Philosophy
in the Department of Physics and Astronomy
in the Graduate College of
The University of Iowa

May, 1971

Thesis supervisor: Associate Professor Donald A. Gurnett

*Research supported in part by the National Aeronautics and
Space Administration under contracts NAS5-10625, NAS1-8141,
NAS1-8144(f), NAS1-8150(f), and NGL-16-001-043(97); and by
the Office of Naval Research under contract N00014-68-A-
0196-0003.

Security Classification

(Security classification of title, body of abstract and indexing annotation must be entered when the overall report is classified)

DD FORM 1473
1 JAN 64

Security Classification

ACKNOWLEDGMENTS

I am grateful to Dr. Rita Sagalyn and Dr. Peter Wildman of Air Force Cambridge Research Laboratories for generously providing data on electron number densities measured with Injun 5. I wish to thank Dr. James A. Van Allen, the principal investigator on Injun 5, for his support and guidance of the project. To my advisor, Dr. Donald A. Gurnett, I owe special thanks, as the conception, design, and construction of the experiment were his accomplishments. I appreciate his continued patience, advice, explanations, and support.

I am indebted to nearly every one of the staff of the University of Iowa Physics Research Center, for at some time during the collection and publication of this data almost everyone helped directly or indirectly. R. Brechwald patiently volunteered his aid in debugging my programs. I am particularly grateful to S. Harrold, W. Kurth, G. Voots, and C. Yankovich for their industry and efficiency in helping to reduce the data. Mrs. S. Van Engelenhoven typed the final manuscript in her usual cheerful and efficient manner. The encouragement and assistance of my wife, Mavis, was invaluable.

This research was supported in part by the National Aeronautics and Space Administration under contracts NAS5-10625, NAS1-8141, NAS1-8144(f), NAS1-8150(f), and NGL-16-001-043(97); and by the Office of Naval Research under contract N00014-68-A-0196-0003.

ABSTRACT

This paper reports on the convection electric fields observed with the double-probe type DC electric field experiment on the low altitude (677-2528 km) polar orbiting Injun 5 satellite. Simultaneous measurements of antenna impedance by the spacecraft make it possible to investigate in detail the operation of the electric antenna system and errors caused by sunlight shadows on the probes, wake effects, and other factors. Electric field magnitudes as small as ± 10 mV/meter can be measured under favorable conditions.

Reversals in the DC electric field at auroral zone latitudes are the most significant convection electric field effect identified in the Injun 5 data. Electric field magnitudes of typically 30 mV/meter, and sometimes 100 mV/meter, are associated with reversals. Electric field reversals occur on $\sim 36\%$ of auroral zone traversals, at about 70° to 80° invariant latitude, and at all local times. They have been identified at magnetically conjugate points in both hemispheres. The latitude and structure of a reversal often change markedly on

time scales less than 2 hours. Electric potentials of greater than 40 keV are associated with these high latitude electric fields. Reversals occur at the boundary of measurable intensities of >45 keV electrons and are coincident with inverted 'V' type low energy electron precipitation events. In almost all cases the $\vec{E} \times \vec{B}/B^2$ plasma convection velocities associated with reversals are directed east or west, with anti-sunward components at higher latitudes and sunward components at lower latitudes. Maximum convection velocities are typically ~ 1.5 km/sec and ordinarily occur at the auroral zone near the reversal. Two extreme (and many intermediate) configurations of anti-sunward plasma convection have been observed to occur on the high latitude side of electric field reversals: (1) Ordinarily, large-scale (>0.75 km/sec) convection is limited to narrow ($\sim 5^\circ$ INV wide) zones adjacent to the reversal. (2) For $\sim 14\%$ of reversals measurable anti-sunward convection has been observed across the entire polar cap along the trajectory of the spacecraft. A summary pattern of >0.75 km/sec polar thermal plasma convection is presented.

TABLE OF CONTENTS

	Page
LIST OF TABLES	viii
I. INTRODUCTION	1
II. DESCRIPTION OF THE EXPERIMENT	3
A. Instrumentation	3
B. Theory	4
C. Operation	10
D. Errors	16
E. Data Analysis	37
F. Improvements	43
III. OBSERVATIONS	45
A. General Observations	45
B. Observations of DC Electric Field Reversals	45
IV. CONCLUSIONS	60
A. Comparison with Barium Cloud Measurements	60
B. Comparison with Magnetospheric Models	60
C. Comparison with Models of Sub- storms and Aurorae	63

TABLE OF CONTENTS (cont'd.)

	Page
APPENDIX Solution for Photo-Electron Current . .	66
LIST OF REFERENCES	69
TABLES	74
FIGURE CAPTIONS	84
FIGURES	90

LIST OF TABLES

		Page
Table 1	Parameters of the DC Electric Field Experiment	74
Table 2	Injun 5 Orbital Data	75
Table 3	Occurrence of Wake Effects	76
Table 4	Probe Potential in the Spacecraft Wake	77
Table 5	Standard Parameters Used in Probe Model Calculation	78
Table 6	DC Electric Field Phenomena Observed at the Auroral Zone	80
Table 7	Average Invariant Latitude of Reversals	81
Table 8	Directions of Convection Components	82

I. INTRODUCTION

The importance of electric field measurements for studying the convection of plasma in the magnetosphere has been recognized for a number of years (Dungey, 1961; Axford and Hines, 1961; Piddington, 1962; Alfvén, 1967; Boström, 1967; and Axford, 1969). However, only recently have techniques for the measurement of magnetospheric electric fields been developed. These techniques include (1) observations of the relative drift of neutral and ionized components of artificial barium clouds (Haerendel et al., 1967; Föppl et al., 1968; Mende, 1968; and Wescott et al., 1969), (2) measurements of potential differences between Langmuir probes on rockets and satellites (Mozer and Bruston, 1967; Fahleson et al., 1970; Gurnett, 1970; Maynard and Heppner, 1970; and Potter, 1970), (3) subionospheric electric field measurements with metal probe pairs carried by high altitude balloons (Mozer and Serlin, 1969), and (4) various other more indirect methods such as observations of whistler duct motions from spectral analysis of radio noise measurements (Carpenter, 1970), and simultaneous charged particle energy spectrum

observations at different points in space (Van Allen, 1970). Electric 'field mill' devices (Wildman, 1965) have not yet proved practical in the magnetosphere. Of these techniques, the most extensive and sensitive measurements have been obtained from artificial barium cloud releases. Unfortunately, barium cloud experiments are limited to dusk local times. Satellite measurements provide much more extensive spatial coverage and quantities of data than is possible with either sounding rockets or barium cloud releases but cannot determine small time scale temporal effects.

This paper reports on the operation and results of the double-probe type DC electric field experiment on the low altitude (677 to 2528 km) polar orbiting Injun 5 satellite. In particular, electric field phenomena which persist for long times (\geq hours) are studied and interpreted in terms of magnetospheric thermal plasma convection. The results are examined for their implications concerning various magnetospheric models.

II. DESCRIPTION OF THE EXPERIMENT

A. Instrumentation

The electric field sensors on Injun 5 consist of two spherical aluminum Langmuir probes 0.203 meters in diameter. The spheres are separated by 2.85 meters between centers, along an axis parallel to the spacecraft y axis. A high impedance differential amplifier is used to determine the potential difference between the electric field probes. The average AC impedance of the two spheres is measured by differentially driving the spheres with a constant amplitude AC current source while measuring the AC potential difference between the spheres. As indicated in Figure 1, the spacecraft is oriented by an internal bar magnet such that the x axis of the spacecraft is maintained parallel to the geomagnetic field. The DC electric field experiment is therefore sensitive to a component of the electric field, E_1 , perpendicular to the geomagnetic field. Most data presented in this paper were stored by a tape recorder on the satellite and transmitted to ground later, on command, at high speed. In this manner, up to 3.8 orbits of continuous data are obtainable.

Table 1 summarizes the parameters of the DC electric field experiment. Details of the orbit of the Injun 5 satellite are given in Table 2. For more information about the VLF experimental package on Injun 5 see Gurnett et al. (1969).

B. Theory

A review of current theories of spacecraft interaction with the ionosphere has been given by Kasha (1969). Fahleson (1967) and Aggson (1966) have discussed the theory of magnetospheric DC electric field measurements with double-probe type antennas on satellites. The rudiments of the theory as presented by Fahleson (1967) are given here in order to form the basis for a discussion of the probe operation in orbit (Section C) and the errors associated with the measuring instrument (Section D).

The problem to be considered is that of a high impedance metal sphere moving in a plasma of high conductivity. The theory involved employs the approximations of (1) a Maxwellian two-component plasma, (2) ion velocity \ll spacecraft velocity \ll electron velocity, and (3) small deviations of the probe potential from neutrality. MKS units will be used. A high impedance probe immersed in

a highly conducting plasma has four principal current constituents in its current-balance equation,

$i = i_e - i_i - i_p$, as shown in the top of Figure 2. The electron current to a spherical electrode is given by

$$i_e = I_e e^{V/U_e} \quad \text{for } V \leq 0 \quad (1a)$$

$$i_e = I_e \quad \text{for } V \geq 0 \quad (1b)$$

where $I_e = -4\pi r^2 n e \left(\frac{kT_e}{2\pi m_e} \right)^{1/2}$
 $U_e = kT_e/e$

V = probe floating potential

r = probe radius

e = magnitude of electron charge

n = electron number density

T_e = electron temperature

and m_e = electron mass.

The ion current to a moving probe is given by

$$i_i = I_i = 4\pi r^2 n e \left(\frac{kT_i}{2\pi m_i} + \frac{|\vec{V}_s|^2}{16} \right)^{1/2} \quad (2)$$

where \vec{V}_s = probe (satellite) velocity

m_i = ion mass

and T_i = ion temperature.

When the probe is in sunlight there will also be a photo-electron current

$$i_p = I_p \quad \text{for } V \leq 0 \quad (3a)$$

$$i_p = I_p e^{-V/U_p} \quad \text{for } V \geq 0 \quad (3b)$$

where $U_p = kT_p/e$ = photo-electron potential, and I_p is a constant depending only the probe surface properties.

Using the relations above, the current balance equation may be solved for the floating potential, V , defined as the probe potential when $i = 0$:

$$V = -U_e \ln \frac{I_e}{I_i + I_p} \quad \text{for } V \leq 0 \quad (4a)$$

$$V = U_p \ln \frac{I_p}{I_e - I_i} \quad \text{for } V \geq 0 \quad (4b)$$

The current-voltage characteristic of a probe is represented schematically in the bottom of Figure 2. Zero potential

has been defined to be the 'space' or 'plasma' potential, where $I_e - I_i - I_p = 0$, which would hold for a spherical surface of radius r in the plasma if no physical probe were present. When a bias current I_B is drawn to a sphere, the condition $I_B \leq I_e - I_i - I_p$ (alternatively $I_B \geq I_e - I_i - I_p$) determines that the probe will be negative (positive) and that Equations (1) through (4) part a (part b) will hold. If the floating potential V is positive, an inhomogeneous 'sheath' of electrons forms around the probe, which we shall refer to as a photo-electron sheath. A negative probe repels electrons, so its 'sheath' is composed of an excess number of positive ions. The characteristic thickness of a sheath is approximately

$$t = \lambda_D \left(-\frac{V}{U_e} \right)^{1/2} \quad \text{for } V \leq 0$$

$$t = \lambda_D \left(\frac{V}{U_p} \right)^{1/2} \quad \text{for } V \geq 0$$

where $\lambda_D = \left(\frac{\epsilon_0 U_e}{ne} \right)^{1/2}$ is the Debye length.

The top diagram in Figure 3 schematically illustrates the inhomogeneous sheath, which forms around the entire spacecraft as well as around the probes and booms. The bottom diagram in Figure 3 shows a Thevenin equivalent circuit of the probe-plasma system for a plasma containing an electric field E_y parallel to the spacecraft $+y$ axis. The voltage drops V_{s+} and V_{s-} across the sheaths of the spheres are given by the floating potentials V_+ and V_- of each probe. The subscripts $+$ and $-$ are added when necessary to identify the probes on the spacecraft $+y$ or $-y$ axes, respectively. The sheath resistances $R_s = \frac{\partial V_s}{\partial i}$ are given in terms of plasma parameters by

$$R_s = \frac{U_e}{I_i + I_p} \quad V \leq 0 \quad (5a)$$

$$R_s = \frac{U_p}{I_e - I_i} \quad V \geq 0 \quad (5b)$$

The voltage sources

$$E_y (\ell/2) \quad \text{and} \quad E_y (-\ell/2)$$

represent the plasma potential at the center of the two spheres. As long as the sheath thickness t is small compared to the antenna length, the effective length, ℓ ,

of the antenna will be equal to the distance between the centers of the spheres. R_B represents the input resistance of the differential amplifier, which is the same for each branch, $R_{B+} = R_{B-}$. From the circuit diagram in Figure 3 it can readily be shown that the observed potential difference between the spheres is given by

$$\Delta V_M = - \frac{E_y \ell}{2} \left[\left(1 + \frac{R_{s+}}{R_{B+}} \right)^{-1} + \left(1 + \frac{R_{s-}}{R_{B-}} \right)^{-1} \right] \quad (6)$$

$$+ \left[V_{s+} \left(1 + \frac{R_{s+}}{R_{B+}} \right)^{-1} - V_{s-} \left(1 + \frac{R_{s-}}{R_{B-}} \right)^{-1} \right]$$

Ideally, the voltage drops across the sheaths of the two spheres are identical, $V_{s+} = V_{s-}$, and the sheath resistances are small compared to the differential amplifier input impedances, $R_{s+}, R_{s-} \ll R_B$. It follows from Equation (6) that in this case the potential difference between the spheres is directly proportional to the y component of the electric field

$$\Delta V_M = - E_y \ell. \quad (7)$$

C. Operation

In this section we describe the features of the data taken with the Injun 5 DC electric field experiment believed to be associated with errors or instrumental effects. Several of these features are shown in Figures 4 and 5. Each figure displays both the electric field and the electric antenna impedance measured during one orbit of the spacecraft. The data are presented in terms of 'measured' electric field, E_M , defined by

$$E_M = - \frac{\Delta V_M}{\ell} . \quad (8)$$

If the sheath resistance R_s is much less than the bias resistance R_B and the two probes are sufficiently identical that their floating potentials V_+ and V_- are equal, then Equation (7) holds and $E_M = E_y$. General features of the impedance measurements are discussed by Gurnett et al. (1969). The impedance is found to be almost entirely resistive at 32 Hz and is attributed to the resistance of the plasma sheath around each probe. The impedance given in the figures is the average of the resistances of the sheaths around the two spheres. Also shown in Figures 4

and 5 is the electron number density, n , of the thermal plasma as measured by the Air Force Cambridge Research Laboratories (AFCRL) experiment on Injun 5. (A constant electron temperature of 2500 °K is assumed in calibrating this data.)

1. $\vec{V}_s \times \vec{B}$

The dashed lines in Figures 4 and 5 represent the magnitude of the $\vec{V}_s \times \vec{B}$ electric field in the reference frame of the satellite. \vec{V}_s is the satellite velocity calculated from the Injun 5 orbit relative to a coordinate system co-rotating with the earth, and \vec{B} is the magnetic field at the spacecraft position computed using the 1965 Cain et al. (1967) expansion for the geomagnetic field. Neglecting wake and shadow effects, the measured electric field E_M in Figure 4 has a sinusoidal shape modulated by the $\pm|\vec{V}_s \times \vec{B}|$ envelope. This sinusoidal shape is due to the satellite spin about the geomagnetic field with a period of about 20 minutes. When the +y axis of the spacecraft is aligned parallel to $\vec{V}_s \times \vec{B}$, there is a peak in the E_M curve; when the -y axis is parallel to $\vec{V}_s \times \vec{B}$, there is a valley.

In Figure 5 the spacecraft is almost not rotating. In the northern hemisphere the y axis of the satellite is nearly aligned with $\vec{V}_s \times \vec{B}$, so $E_y \approx +|\vec{V}_s \times \vec{B}|$. Since the $\vec{V}_s \times \vec{B}$ direction reverses at the magnetic equator, $E_y \approx -|\vec{V}_s \times \vec{B}|$ in the southern hemisphere. During Injun 5's lifetime the spin rate has increased and decreased several times. Both senses of spin about the geomagnetic field direction have been observed.

2. Shadow Effects

The large perturbations in Figures 4 and 5 labeled 'spacecraft shadows' occur when the photo-electron current to one of the spheres changes as the sphere enters the sunlight shadow of the spacecraft body. Figure 6 illustrates that small increases in the impedance often accompany the occurrence of shadows on the spheres. Also shown are the angles θ_{s+} and θ_{s-} between the sun direction and the vectors to each sphere from the spacecraft center. Since, from Figure 1, the spacecraft subtends a 20° half-angle as seen from a sphere, shadow effects are predicted to occur when θ_s exceeds 160° . Shadows on the +y (-y) sphere cause positive (negative) perturbations in

the measured electric field. Shadow effects are wider when the satellite is spinning slower. The magnitude of the offsets in E_M caused by shadows is larger at high latitudes and smaller near the equator. Occasionally one sphere is shadowed by the other, as occurs in Figure 4 at 1340 UT. A shadow of one of the joints in the electric antenna booms falls on a probe at 2017 UT in Figure 5.

For orbits in the dawn-dusk plane, such as that shown in Figure 4, shadowing of the spheres by the supporting booms (cf. Figure 1) is unequal for the two spheres at orientations corresponding to peaks and valleys in the $\hat{y} \cdot \vec{V}_s \times \vec{B}$ electric field. As illustrated in Figure 4, this asymmetrical boom shadowing effect adds to peaks in $\hat{y} \cdot \vec{V}_s \times \vec{B}$ in one hemisphere and subtracts from peaks in $\hat{y} \cdot \vec{V}_s \times \vec{B}$ in the other hemisphere, because $\vec{V}_s \times \vec{B}$ reverses direction at the equator. For noon-midnight orbits, boom shadowing is symmetrical on the two spheres at $\hat{y} \cdot \vec{V}_s \times \vec{B}$ peaks and valleys. Figure 7 shows that, in this case, E_M equals $\pm |\vec{V}_s \times \vec{B}|$ at peaks and valleys to within 10 mV/meter.

3. . Umbra Effects

Figure 5 shows an orbit of electric field data in which Injun 5 passes through the earth's umbra. In Figure 5, as the spacecraft enters the earth's umbra, a peculiar perturbation occurs. It consists of two separate effects: (1) a change in the electric field toward zero (which in Figure 5 is a positive change in E_M), and (2) several periodic negative spikes in the electric field measurement. These spikes correspond exactly to the times that the impedance measurement is made. Figure 8 shows two more examples of both the spikes (negative in both cases) and the change toward zero. These effects occur only when the spacecraft is in the umbra and simultaneously very low electron number densities are measured, as illustrated by Figure 5. Impedance values of about 10^6 ohms or greater invariably accompany the phenomenon.

When the spacecraft leaves the umbra in Figure 5, a negative step in E_M occurs. Such steps occur commonly at umbra transitions, with E_M greater inside the umbra.

4. Wake Effects

The large negative perturbation in Figure 4 labeled 'spacecraft wake' occurs when the +y sphere

enters the satellite's rarefied velocity wake. Figure 9 shows the correlation between wake effects and the angle between the +y sphere and $-\vec{V}_s$, on three successive passes over the north polar cap. $\hat{y} \cdot \vec{V}_s \times \vec{B}$ has been subtracted from the electric field data shown. The wake effects shown occur while the probe is within 80° of $-\vec{V}_s$. Tables 3 and 4 give the results of a study of 451 occasions when one sphere came closer than $\pm 30^\circ$ to the $-\vec{V}_s$ vector. Any clearly distinguishable electric field perturbation which correlated with the minimum angle to $-\vec{V}_s$ was classified as a wake effect in this study, so some naturally occurring electric field events may be included by chance. Table 3 shows that virtually all wake effects are accompanied by impedances greater than 10^6 ohms and that most of the wake effects in the study occurred at high altitude. Table 4 shows that more than 88% of the time the perturbation was such that the potential of the probe in the wake was more positive than the potential of the probe outside the wake region, and that wake effects occurred more than twice as often when the +y sphere was in the wake as when the -y sphere was in the wake. The example of a wake effect shown in Figure 4 occurs when the

impedance is greater than 10^6 ohms. Figure 4 also shows the low electron number density, as measured by the AFCRL experiment on Injun 5, which is commonly observed whenever wake effects or high impedances occur. During the orbit shown in Figure 4 the electric antenna spheres entered the wake region seven times, in both hemispheres. Nevertheless only one wake effect occurred, and that event occurred when the +y sphere was in the wake, at high altitude, high impedance, and low electron number density.

D. Errors

In this section we shall explain the occurrence of the instrumental effects described in Section C and we shall investigate other possible sources of error in the DC electric field measurements. Because variations in measured electric fields not otherwise explained will be attributed to magnetospheric phenomena, considerable detail is justified in discussing errors.

1. Theoretical Predictions of Probe Behavior

To help delineate the relative conditions under which various effects may be expected to occur, we shall develop a numerical model of the response of the double

probe system in terms of plasma parameters. The theory presented in Section B comprises the mathematical basis of the model. Equation (6) depends, through Equations (4) and (5), on parameters which are constant, except for the medium parameters n (number density), T_e (electron temperature), T_i (ion temperature), and E_y (electric field component). In Equation (9), Equations (6) and (8) are rewritten to show explicitly the linear dependence of the measured quantity, E_M , on the electric field E_y and the floating potentials, V_+ and V_- .

$$E_M = E_1(E_y) + E_2(V) \quad (9a)$$

$$E_1(E_y) = \frac{E_y}{2} \left[\left(1 + \frac{R_{S-}}{R_{B-}} \right)^{-1} + \left(1 + \frac{R_{S+}}{R_{B+}} \right)^{-1} \right] \quad (9b)$$

$$E_2(V) = \frac{V_-}{2} \left(1 + \frac{R_{S-}}{R_{B-}} \right)^{-1} - \frac{V_+}{2} \left(1 + \frac{R_{S+}}{R_{B+}} \right)^{-1} \quad (9c)$$

Since the Injun 5 orbit includes altitudes from 677 to 2580 kilometers, the electron number density may vary by several orders of magnitude. The electron densities, as measured by the AFCRL experiment on Injun 5, are commonly in the range 10^4 to 10^5 electrons/cm³, but

may be higher at perigee near the equator and occasionally as low as 10^3 electrons/cm³ at apogee over the polar caps (R. Sagalyn, private communication, 1970). In the model we shall therefore independently vary n . The electron temperature T_e is less well known. Brace et al. (1967) have reported average values of 500 - 3000 °K at 1000 km at solar minimum. The preliminary results of Sagalyn's experiment (private communication, 1970) on Injun 5 indicate a typical electron temperature of 2500 °K, with temperatures sometimes as high as 10,000 °K and frequently about 5000 °K above 1500 km over the polar caps (at solar maximum). In the model we assume $T_e = 2500$ °K, or else vary T_e independently. The calculation is insensitive to the ion temperature T_i , which is taken to be 1500 °K.

It is obvious from Equation (9c) that asymmetries in V , R_s , or R_B for the two spheres may be important sources of errors. V and R_s are dependent on plasma parameters (see Equations (4) and (5)) except for the photo-electron current I_p . The photo-electron current may differ for the two spheres at a given time due to either (1) differential shadowing or (2) unequal surface

properties of the spheres. Assuming that the latter effect is constant in time, shadowing may be exploited to find approximate values of I_p for each sphere. A study has been made of 86 occasions when the spacecraft body shadowed one of the electric antenna spheres. Flat-topped shadow perturbations were selected to ensure that a sphere was completely shadowed. Figure 10 shows the results of the study. In the bottom drawing, using the Ohm's Law approximation,

$$\Delta I_p \cong \frac{|\Delta V_M|}{R_s} = \frac{2|\Delta E_M|}{R_s}$$

photo-electron currents of $I_{p+} = 4 \mu\text{amps}$ and $I_{p-} = 3 \mu\text{amps}$ are suggested. The top drawing shows the results of an analytic solution (described in the Appendix) for the photo-electron currents, which gives $I_{p+} = 3 \pm 1 \mu\text{amps}$ and $I_{p-} = 2 \pm 1 \mu\text{amps}$. The latter values have been adopted for use in the model. The difference $I_{p+} - I_{p-}$ can be checked by examining transitions from the umbra region into sunlight (excluding situations with shadowing). A study of 26 such transitions implies that $I_{p+} - I_{p-} = 1.5 \pm 0.5 \mu\text{amps}$ in the linear approximation (which will

tend to overestimate the currents). The asymmetry presumably arises from surface contamination of the spheres, perhaps during the launch. Because sunlight strikes different areas of each sphere as the spacecraft rotates, the magnitude of the photo-electron asymmetry and its consequences may be orientation dependent. In the model, however, any orientation dependence of I_p has been neglected. Table 5 summarizes the values of parameters employed in the numerical model.

Figures 11 through 18 show results calculated using the probe system model. Figure 11 shows values for the floating potential, V , of a sphere as a function of electron number density, n , for a range of electron temperature values. The curves were calculated using Equation (4). The potentials are typically a fraction of a volt negative, so the condition that V be small is satisfied. For the values of T_i and T_e used in the calculation the inequality ion velocity $<$ satellite velocity $<$ electron velocity is also satisfied. Typical Debye lengths and sheath thicknesses encountered in the Injun 5 orbit are shown in Figure 12. Sheath widths less than the probe radius are predicted. In Figure 13 V is compared

for the two spheres and the spacecraft body. The effects of the obvious asymmetry will be discussed below. Figure 14 shows that in sunlight conditions there is also an asymmetry in the corresponding sheath resistances for the two spheres.

The principal test which may be applied to determine the extent to which the model is quantitatively correct is to compare predicted and measured values of the sheath impedance. The points plotted in Figure 15 correspond to sheath resistances measured around the Injun 5 orbit and electron number densities measured simultaneously with the AFCRL experiment on Injun 5. Because T_e varies strongly with altitude, latitude, and local time (cf. Brace et al., 1967), it is not expected that the measured points $R_s(n)$ will fall on any one calculated curve $R_s(n, T_e)$. In general the highest T_e will occur at high altitudes where n is low, and conversely. An examination of the measured versus computed values in Figure 15 verifies that this occurs. Furthermore, the values of R_s observed fall on theoretical curves corresponding to reasonable values of T_e . These facts suggest that there is reasonable quantitative correspondence

between the model predictions and actual probe behavior. Additional verification of the validity of the model is its ability to explain the various instrumental sources of error.

2. Shadow Effects

Figure 16 shows the calculated magnitudes of the quantities $E_1(E_y)$ and $E_2(V)$ introduced in Equation (9), for darkness, sunlight, and shadow conditions. If $R_s \ll R_B$, $E_1 = E_y$ represents the real electric field y-component measurable in the satellite reference frame. Under ideal conditions of sphere symmetry in every respect, $E_2 = 0$.

It is evident from Figure 16 that the behavior of E_2 when either sphere is shadowed explains the larger magnitudes of polar (lower n) versus equatorial (higher n) shadow effects. (Consistency is expected because shadows were used to estimate I_p .) Since the electric field antenna booms and boom joints can shadow as much as 20% of the surface of a probe, the effects of boom shadows are proportionately smaller than those indicated for total sphere shadowing. Maximum boom shadowing errors are therefore expected to be about 40 mV/meter.

3. Umbra Effects

The discrepancy of 2 mV/meter between E_x in sunlight and E_y , for large n , shown in Figure 16 is due to finite bias resistance in the factor $(1 + R_s/R_B)^{-1}$ in Equation (9). This factor is negligible for usual n values. When n is low, the discrepancy increases because R_s becomes large (see Figure 14). In daylight the effect is important only below $n = 2 \times 10^3$ electrons/cm³ (which rarely occurs). At night, when the I_p term disappears from Equation (5), the effect of large sheath resistance is much greater. We attribute the change towards zero electric field which appears in Figures 5 and 8 (ignoring the spikes) as the satellite enters the earth's umbra, to this cause. It is consistent with this explanation that as n rises towards lower latitudes in the umbra, the effect disappears. In the example in Figure 5 the magnitude of the change is about 50 mV/meter, while the AFCRL number density experiment indicates $n = 2 \times 10^3$ electrons/cm³. The agreement with the model prediction is good. Figure 14 shows the accompanying large increase in impedance predicted (and observed; see Figures 5 and 8) as the spacecraft goes from sunlight into darkness while n is low.

Figure 16 verifies that in darkness, E_2 is nearly zero. However, in sunlight, the sphere floating potentials are different, as shown in Figure 11, due to asymmetric photo-electron emission. Excluding values when densities are below 2×10^3 electrons/cm³, E_2 may be as great as -30 mV/meter in sunlight. This is in exact agreement with the magnitude and direction of the jump in the measured electric field observed when the spacecraft undergoes the transition from the earth's umbra into sunlight at 2127 UT in Figure 5. The spheres were not shadowed at this time by the spacecraft booms or body. E_2 for both spheres in sunlight may vary by up to 20 mV/meter as n varies slowly with altitude and latitude around the Injun 5 orbit. Like boom shadowing, this error contributes to the difference between E_m and $\hat{y} \cdot \vec{V}_s \times \vec{B}$, and is virtually impossible to calculate. The method for eliminating these effects will be discussed in Section E. The combination of 20 mV/meter due to the response of the asymmetric probe system to slow plasma variations around the Injun 5 orbit, and 40 mV/meter boom shadowing, gives a maximum of 60 mV/meter for $E_M - \hat{y} \cdot \vec{V}_s \times \vec{B}$. This is in good agreement with the 50 mV/meter maximal discrepancies observed.

In Figure 5 the satellite crosses the earth's umbra while its y axis is nearly parallel to the $\vec{V}_g \times \vec{B}$ direction in the northern hemisphere. The measured electric field fails to go through zero at the midnight equator where $\vec{V}_g \times \vec{B}$ changes direction, by about 50 mV/meter. This difference corresponds to a 0.14 volt constant 'contact potential'. This constant offset should not affect the results of the DC electric field experiment beyond shifting its zero point. In sunlight the contact potential is counteracted almost completely by the effects of the photo-emission asymmetry of the two spheres. As shown in Figure 5, at the sunlit equator the electric field measurement misses zero by just 20 mV/meter. (Prior to the boom joint shadow indicated at 2018 UT, neither sphere was shadowed.) The difference between the amounts by which E_M exceeds zero at the two equators is 30 mV/meter, which corresponds exactly to the 30 mV/meter jump attributed to photocurrent asymmetry evident at 2127 UT in Figure 5. Furthermore, the sheath impedance at the sunlit equator is $R_s \approx 8 \times 10^4$ ohms. In the linear approximation, therefore, the photo-current asymmetry should be

$$\Delta I_p \cong \frac{2|\Delta E|}{R_s} = 1.1 \text{ } \mu\text{amps.}$$

This value is in agreement with the results of the shadow study previously discussed. The consistency evident in the observations of contact potentials, umbra transition discontinuities, shadowing magnitudes, and sheath impedances promotes confidence in the numerical model, which correctly reproduces their interrelationship.

The so-called 'rectification effect' observed in the umbra region (see Figures 5 and 8) may be explained as follows. The potential of a sphere due to the sinusoidally varying current of magnitude $i_z = V_{z0}/R_B$ impressed briefly on each sphere by the impedance measurement (see Gurnett et al., 1969) may be expanded in a Taylor series:

$$V = V_0 + \frac{\partial V}{\partial i} (\Delta i) + \frac{1}{2} \frac{\partial^2 V}{\partial i^2} (\Delta i)^2 + \dots$$

where $i = i_z \cos \omega t$ and V_0 is the floating potential from Equation (4). The DC electric field measurement effectively averages this potential over time, so we obtain

$$\begin{aligned}
 V &= \langle V_0 \rangle + \left\langle \frac{\partial V}{\partial i} i_z \cos \omega t \right\rangle + \frac{1}{2} \left\langle \frac{\partial^2 V}{\partial i^2} i_z^2 \cos^2 \omega t \right\rangle + \dots \\
 &= V_0 + \frac{1}{4} \frac{\partial^2 V}{\partial i^2} i_z^2 \\
 &= V_0 + V_z
 \end{aligned} \tag{10}$$

V_z is an additional term present only when the impedance measurement is made. In terms of plasma parameters we have, for $V < 0$,

$$V_z = \frac{1}{4} \frac{U_e}{(I_p + I_i)^2} \frac{V_{zo}^2}{R_B^2}$$

We shall investigate the effects of this term in darkness for low electron densities. Figure 13 verifies that the sphere floating potential will be negative. $I_p = 0$ in darkness, and I_i is proportional to n , so V_z under the specified conditions will become very large and can dominate the floating potential term V_0 in Equation 10. If $V_{z+} \neq V_{z-}$, which in darkness could happen due to an asymmetry in the bias resistances (see Equation (9c)), E_2 will change when the impedance measurement is on. If R_{B+} were greater than R_{B-} then the resulting perturbation

in E_2 would always be negative. This effect, which constitutes a rectification of the impedance measurement driving current by the electric antenna system, qualitatively explains the negative spikes observed when the impedance measurement is made in the umbra at low number densities as shown in Figures 5 and 8. Because umbra effects generally occur at middle to low latitudes, they do not interfere with the measurement of auroral zone and polar cap electric fields.

4. Wake Effects

The satellite velocity \vec{V}_s exceeds the thermal ion velocity at Injun 5 altitudes. As a result, ions are swept away by the moving spacecraft and a rarefied wake region exists behind the satellite. Because approximate charge neutrality must be maintained, electrons cannot enter the wake until the heavier, slower, ions do. Hence the wake region is rarefied and has a slightly negative potential.

The model of probe behavior predicts that when the electron number density in the probe vicinity drops below $\sim 2 \times 10^3$ electrons/cm³, the probe floating potential

becomes positive with respect to the space potential and a photo-electron sheath is formed (see Figure 13). Equation (9) indicates that if the $+y$ ($-y$) sphere potential rises, E_M , through E_2 , will drop (rise). This is in agreement with the observations of wake effects reported in Section C. Furthermore, as shown by Figure 13, a photo-sheath forms around the $+y$ sphere at higher n than for the $-y$ sphere. It is therefore expected that wake effects should be observed more frequently when the $+y$ sphere is in the wake region than when the $-y$ sphere is in the wake. This prediction, also, agrees with observations (see Table 4). Figures 14 and 15 show that the impedance should rise dramatically, to $\sim 10^6$ ohms, when a photosheath forms. High measured impedances have been reported to be a feature of wake effects (see Figure 4). Quantitative comparisons are not possible because the densities and temperatures in the wake regions are unknown. However, on the basis of the excellent qualitative agreement of these predictions of wake effects with the observations discussed in Section C, we conclude that wake effects are in fact caused when one probe develops a photo-electron sheath in the rarefied region behind the moving spacecraft.

5. Variations and Gradients in Plasma Parameters

The effect of variations in n and T_e (at both spheres) may be investigated by taking partial derivatives of Equation (9) with respect to these quantities. The top diagram in Figure 17 shows the numerical evaluation of terms of the equation

$$\Delta E_M = \frac{\partial E_1}{\partial T_e} \Delta T_e + \frac{\partial E_2}{\partial T_e} \Delta T_e$$

as functions of n , for an arbitrarily chosen, but large, $\Delta T_e = 100$ °K, evaluated at $T_e = 2500$ °K. ΔE_M is clearly very small everywhere except for a small interval at low n which corresponds to just the +y sphere having a photo-sheath. In the bottom diagram of Figure 17, the terms of

$$\Delta E_M = \frac{\partial E_1}{\partial n} \Delta n + \frac{\partial E_2}{\partial n} \Delta n$$

are shown for $\Delta n = 0.1 n$. The results are similar in that ΔE_M is negligible except while just one sphere has a photo-sheath.

Figure 18 illustrates the effects of gradients in the plasma such that n or T_e is different at the two spheres. In the top diagram of Figure 18 the changes in E_1 and E_2 are shown which would occur if the $+y$ sphere encountered temperatures of 2450°K while at the $-y$ sphere the temperature was 2500°K . It is unlikely that such a large, 2%, gradient would be encountered in the 2.85 meters between spheres. The magnitude of ΔE_M predicted remains less than 6 mV/meter, so the effect for actual gradients is probably negligible. The bottom of Figure 18 shows the change ΔE_M resulting from lowering n at the $+y$ sphere by 10%. This unphysically large gradient in only 2.85 meters produces less than 10 mV/meter change in the measured electric field above $n = 2 \times 10^3$ electrons/cm³. We conclude that the effects of gradients in electron temperature or number density are not serious except at densities low enough to cause photo-sheaths to occur.

In addition to these plausibility arguments, experimental evidence can be given that n and T_e variations and gradients have negligible effects on the DC electric field measurement. Although electron number densities

or temperatures measured by the AFCRL experiment on Injun 5 frequently exhibit fluctuations in the same intervals when electric field noise is observed, the AFCRL data and the DC electric field variations do not correlate on a one-to-one basis. Figures 19 through 22 show 'worst-case' examples of both electric field and number density fluctuations. These data were taken in the high data rate mode during apogee polar passes in the northern hemisphere in winter. The DC electric field is measured 16 times per second in this mode while the AFCRL experiment in fact measures a quantity proportional to $n\sqrt{T_e}$. A constant electron temperature of 2500 °K has been assumed in calibrating the data. It is evident that the fluctuations shown as due to number density variations could alternatively be due to electron temperature variations. The lack of correlation of the AFCRL and DC electric field data may therefore be taken as an indication that neither n nor T_e variations which exist directly affect the DC electric field measurement. In Figures 19 and 20 large (≥ 50 mV/meter) electric field fluctuations occur but only small variations in n (or T) occur. Figures 21 and 22 show number density (or

temperature) fluctuations of $\geq 100\%$, but these fluctuations show no relationship to the variations in electric field observed.

6. Energetic Charged Particles

Over the auroral zones Injun 5 encounters intense fluxes of energetic charged particles. In order to affect the operation of the DC electric field experiment the current contribution from energetic ions minus the current contribution from energetic electrons must be different for each sphere. Because the gyroradius of a 50 eV electron is about one meter or greater at Injun 5 altitudes, no significant gradients are expected in the 2.85 meters between spheres. An upper limit for > 50 eV electron flux encountered in the Injun 5 orbit is $J_e = 5 \times 10^8$ particles/cm²-sec. (L. A. Frank, private communication, 1971). This flux corresponds to a density of

$$n_e (> 50 \text{ eV}) = \frac{J_e}{|\vec{v}_e|} = 1 \text{ electron/cm}^3$$

assuming 50 eV electrons. As this density is about 0.1% of the thermal electron densities encountered in the Injun 5 orbit, energetic particle contributions are neglected.

7. Interference

On just a few occasions during the Injun 5 lifetime, small (20 mV/meter) oscillations with ~30 second period were detected by the DC electric field experiment. These oscillations were found to coincide precisely with the voltage sweep of the AFCRL electron number density experiment on Injun 5. The exact cause of the interference has not been determined. As the oscillations are unmistakable in appearance, no further efforts are necessary to eliminate them.

Most errors in the data which originate in telemetry or recording electronics also cause parity errors and are eliminated by a parity check. It is not uncommon, however, to encounter single data points considerably different from the $\hat{y} \cdot \vec{V}_s \times \vec{B}$ electric field value. These isolated points are eliminated from the data because they are believed to be caused by telemetry or recording errors which involved no parity change.

Thermal noise due to the bias resistances is evidently small, as the electric field measured at low latitudes varies smoothly down to the 2.75 mV/meter minimum measured step size.

8. Summary

With the aid of a numerical model of Langmuir probe response to plasma parameters based on ranges of values of plasma parameters encountered in the Injun 5 orbit, we have explained, qualitatively, and, where appropriate measurements exist, quantitatively, all of the various instrument-associated effects evident in the Injun 5 DC electric field experiment data. The amounts by which the measured electric field misses the $\pm |\vec{V}_g \times \vec{B}|$ limit have been accounted for by the slowly-varying errors due to shadowing by the spacecraft booms and changes in plasma parameters around the Injun 5 orbit. Other observed effects we have explained include (1) perturbations associated with shadows of the spacecraft body or boom joints on the electric antenna spheres, (2) perturbations associated with the spacecraft velocity wake, (3) discontinuities upon entering or leaving the earth's umbra caused by differences in the photo-emission properties of the two spheres, (4) negative spikes due to rectification of the impedance measurement driving current, (5) changes in the measured field magnitude due to finite bias resistance, (6) contact potentials, and

(7) interference phenomena. In addition, we have examined the possibility of errors due to other effects, such as energetic charged particle fluxes, electron density and temperature gradients between the spheres, and plasma variations along the satellite path.

Spacecraft shadows and steps at the edge of the umbra can be easily identified from spacecraft attitude and orbital parameters. All remaining errors are found to be less than 10 mV/meter except at electron densities predicted by the model to be less than about 2×10^3 electrons/cm³, below which photo-sheaths begin to form around the spheres. However, a criterion for the possibility of large errors based on observations, rather than on the model, can be determined. When a photo-sheath forms around either sphere, the antenna impedance rises sharply. The study of 451 spacecraft wake predictions discussed in Section C and summarized in Tables 3 and 4 shows that wake effects (and hence photo-sheaths) occur only when impedances are greater than 10^6 ohms. The impedance measurement thus provides a rigorous observational test of the quality of the DC electric field data. If the impedance is less than 10^6 ohms, the DC electric field measurements

may be interpreted using Equation (7). When the impedance is greater than 10^6 ohms, caution must be exercised because large impedances can result from either unusually high electron temperatures or low number densities. Only the latter will result in the formation of photo-sheaths and the associated susceptibility to various large errors. For impedances less than 10^6 ohms, a limit on the contributions due to all errors except the various manifestations of shadowing and slow changes in plasma parameters around the Injun 5 orbit may be set at ± 10 mV/meter. In the next section the method used to eliminate the larger, slowly changing errors, as well, will be discussed.

E. Data Analysis

1. Magnetospheric Electric Field Determination

In order to determine naturally occurring electric fields it is necessary to subtract the $\vec{V}_s \times \vec{B}$ electric field and other instrumental effects from the measured electric field. In this study electric field effects are disregarded when the sheath resistance exceeds 10^6 ohms. As described in Section D, this condition eliminates

virtually all wake and umbra effects and assures that the differential amplifier impedance is much larger than the sheath resistance. Since spacecraft shadow effects are predictable from the spacecraft orientation, data are also discarded when a probe is close to the anti-sun vector. The component of the $\vec{V}_s \times \vec{B}$ electric field parallel to the antenna axis, $\hat{y} \cdot \vec{V}_s \times \vec{B}$, is easily calculated also from knowledge of the spacecraft orientation. The only serious problem which remains is to correct for the smooth long term variations responsible for the amount (≈ 50 mV/meter) by which the measured electric field misses $\hat{y} \cdot \vec{V}_s \times \vec{B}$, as discussed in the last section. Because of uncertainties in the various plasma parameters involved, this factor cannot be calculated with sufficient accuracy to be useful.

The procedure which has been adopted for subtracting $\hat{y} \cdot \vec{V}_s \times \vec{B}$ and the boom shadowing error is the following: a smooth curve E_s is hand-drawn through the measured electric field subject to the following requirements:

- (1) It has a sine wave shape which is qualitatively the same as the computed $\hat{y} \cdot \vec{V}_s \times \vec{B}$ field.

- (2) The modulation amplitude and phase are adjusted to provide a good fit at low latitudes where no convection electric fields are expected.
- (3) In cases of uncertainty the curve is drawn closer to the average measured field.

This procedure takes into account both $\hat{y} \cdot \vec{V}_s \times \vec{B}$ and the smooth changes due mostly to boom shadowing. In cases of uncertainty the residual electric field, $E_c = E_M - E_s$, attributed to magnetospheric electric fields, will in general underestimate the actual naturally occurring electric field. If natural electric fields occur which are small and uniform for times comparable to the rotation period of the spacecraft, they will unfortunately but unavoidably be subtracted out by this procedure and will not appear in E_c . However, when the spacecraft is rotating slowly, for some orientations boom shadowing is excluded and the magnitude of E_c can be determined to an accuracy of ± 10 mV/meter. The absolute values of E_s and E_c cannot usually be determined more accurately than about ± 30 mV/meter. Fluctuations in the E_c electric field which occur with periods much less than the satellite spin

period are significant if their magnitude exceeds 10 mV/meter. Figure 23 shows an example of E_S compared with E_M and $\hat{y} \cdot \vec{V}_S \times \vec{B}$ for a full orbit of Injun 5.

The left-hand side of Figure 24 illustrates the data reduction procedure used to determine the natural electric field, E_C , for a typical polar pass. E_S is the smooth curve drawn to best approximate the $\hat{y} \cdot \vec{V}_S \times \vec{B}$ field and the boom shadowing error. The difference electric field, $E_C = E_M - E_S$, has abrupt reversals of approximately ± 30 mV/meter at 2225 and 2234 UT. The angles between the probes and the sun vector, θ_S , verify that for these events neither probe was in a shadow. The angles between the probes and the velocity vector, θ_V , indicate that the +y sphere was in the wake region at 2234 UT, but because the impedance is much less than 10^6 ohms the event at this time could not be due to a wake effect. Hence, these electric field reversals are assumed to be due to naturally occurring magnetospheric electric fields.

2. Convection Velocity Determination

Axford (1969) has explained that at Injun 5 altitudes the conductivities are such that a DC electric field

is related to the convection velocity \vec{V}_c of the plasma by the equation

$$\vec{V}_c = \frac{\vec{E}_c \times \vec{B}}{B^2}.$$

The magnetic orientation of Injun 5 ($\hat{x} \parallel \vec{B}$) restricts the DC electric field experiment to measure only electric fields perpendicular to the geomagnetic field. Furthermore, since only the E_y component of the electric field is sensed, only the component of convection velocity parallel to the \hat{z} axis of the spacecraft can be inferred. The convection velocity component measured is computed from the relation

$$\vec{V}_c = \frac{(E_c \hat{y}) \times (B \hat{x})}{B^2} = - \frac{E_c}{B} \hat{z} \quad (11)$$

The convection velocity components associated with the electric fields shown in the left-hand side of Figure 24 are illustrated on a magnetic local time/invariant latitude polar diagram in the right-hand side of Figure 24. Each arrow represents the measured component of the convection velocity computed using

Equation (11). The length of the arrow is proportional to the magnitude of \vec{V}_c and the direction of the arrow is in the direction of the convection velocity sensed. If $|\vec{V}_c| < 0.25$ km/sec, a dot is drawn. The base of each arrow, or the location of each dot, gives the satellite position at half-minute intervals. Since variations in \vec{V}_c occur within the 30 seconds between arrows, each arrow corresponds to the maximum or 'envelope' convection velocity during the interval. It must be emphasized that the arrow represents only the component of the convection velocity detected; it does not represent the vector direction of the convection velocity since only one component is measured. Because of the orientation of the spacecraft during the events shown in Figure 24, the north-south component of the convection velocity cannot be determined.

Since the satellite is rotating very slowly and boom shadowing cannot occur for the orientations shown in Figure 24, the convection velocity component can be determined very accurately for this example. In general the magnitudes of convection velocity variations determined for intervals much smaller than the satellite rotation period are believed to be uncertain by about

0.25 km/sec and, as in the case of E_c , represent a lower limit. Uniform convection velocities for times comparable to the Injun 5 spin period are not expected to be detectable if the convection velocity is less than about 1 km/sec because slowly-varying electric fields are eliminated in the data reduction procedure.

F. Improvements

As an aid to future missions to measure magnetospheric DC electric fields, we briefly list some of the practical considerations we have found to be extremely important.

1. Symmetry for double-probe systems is obviously of paramount importance. Stub booms should be added to give the probes translational symmetry, as suggested by Fahleson (1967). This would eliminate the boom shadowing problems we encountered. Efforts should be made to achieve identical photo-emission properties for the surfaces of the two spheres (see Fahleson et al., 1970), and to ensure that the surfaces stay clean during launch. The spheres must be as similar as possible electrically, also, particularly with respect to having equal differential amplifier input resistances in each branch.

2. It is essential that the input impedance of the differential amplifier be very much higher than the sheath impedances encountered anywhere in the satellite orbit.

3. Accurate knowledge of satellite attitude is critical for calculation of $\hat{y} \cdot \vec{V}_s \times \vec{B}$ and shadowing conditions.

4. The measurement of plasma sheath impedance by Injun 5 proved to be a valuable adjunct to the DC electric field measurement, and quantitative error analysis would not have been possible without it. We suggest that future missions by other experimenters would also be improved by including an impedance measurement.

5. Simultaneous measurements of plasma parameters, such as electron number density and temperature, are also useful in evaluating the performance of the electric antenna, as well as for investigating the complex phenomena, such as aurorae, occurring in the magnetosphere.

6. The use of three orthogonal pairs of electric field probes would permit measurement of the vector direction of the DC electric field.

III. OBSERVATIONS

A. General Observations

Significant DC electric fields not attributable to any known instrumental effect are observed at middle and high latitudes on nearly every orbit of the Injun 5 satellite. At the plasmopause/light ion trough boundary small (10 - 20 mV/meter) electric field perturbations are sometimes observed, generally corresponding to westward convection outside the plasmasphere. At high altitudes, above about 1500 km, over the auroral zone/polar cap regions irregular electric field fluctuations called 'noise' with time scales generally less than 60 seconds are consistently detected. Figure 19 shows an example of electric field noise. The general characteristics of both electric field noise and plasmopause effects have already been discussed by Cauffman and Gurnett (1971a).

B. Observations of DC Electric Field Reversals

1. General Characteristics

Frequently at the auroral zone electric field perturbations are observed which take the form of reversals

in the electric field direction in a geostationary reference frame. The occurrence of such reversals does not depend on sheath impedance or spacecraft orientation. An example of an electric field reversal has been shown in the left-hand side of Figure 24 at 2125 UT. In the right-hand side of Figure 24 the same reversal is interpreted in terms of an $\vec{E} \times \vec{B}/B^2$ convection velocity. On either side of the reversal is a 'zone' of oppositely-directed thermal plasma convection. Table 6 gives the occurrence statistics, for 286 auroral zone crossings, of 'noise' (more than 2 zones; an example is shown in Figure 24 at ~2234 UT), reversals (2 zones), single zones, and quiet crossings ($|\vec{E}_c| < 10$ mV/meter). Reversals have been chosen as the subject of this study because they occur most frequently, they evidently identify a boundary which is of fundamental significance with regard to magnetospheric structure, and they are the most reliably measured electric field phenomenon. The signature of a reversal cannot arise due to a spurious shadow. Because the overall magnitude cannot be changed by an error in drawing E_g , uncertainty is confined to where the electric field crosses zero; the peak-to-peak magnitude is unaffected by the data reduction procedure.

Three examples of reversals which occurred on different days of January, 1969, are shown in Figure 25. In these three cases a reversal occurs at 75° INV at dawn, but, as is frequently true, no corresponding electric field perturbation is detected at dusk.

In Figure 26 reversals are shown which occur at similar latitudes at both dawn and dusk local times. The different polar diagrams in Figure 26 represent opposite hemispheres one hour apart. The reversals in the two hemispheres occur on opposite ends of the same magnetic field lines. On the dawn side, in the northern hemisphere (top and bottom diagrams in Figure 26), a reversal occurs at $\sim 73^{\circ}$ INV. In the opposite hemisphere (center diagram), a reversal occurs at 70° INV, again at ~ 3.5 hours MLT. The electric fields for these reversals (not shown) display several oscillations with ~ 20 second periods on the low latitude sides of each of the three reversals. On the dusk side of Figure 26 another, smaller, pair of conjugate reversals may be seen at 75° INV and ~ 15.5 hours MLT.

Special mention should be made of the observation at 1643 UT in Figure 26. Here, because the satellite

rotates, only the north-south component of convection is being measured. Simultaneously, the magnitude of convection measured becomes equal to zero, and afterwards again becomes non-zero. Both before and after 1643 UT, the convection is determined to have eastward components. This event is interpreted to mean that the true convection direction is eastward, with no north-south component. One hour later (at 1730 UT) at the magnetically conjugate location, only the east-west component is measured, and large eastward convection is observed.

In Figure 27 six successive polar cap crossings in the noon-midnight plane are shown. The plasma convection detected at auroral latitudes is consistent with the interpretation that the satellite path sliced through narrow longitudinal bands of convection which were directed sunward at latitudes below about 75° INV and anti-sunward at higher latitudes. The width of the convection zones observed appears greater before dawn and after dusk.

Figure 28 depicts an example of pairs of convection reversals occurring on both sides of the polar cap at about 75° INV, for three successive dawn-to-dusk passes

over the north polar cap. A large anti-sunward zone of convection appears to be directed across the center of the polar cap in the top diagram. At 1930 UT in the middle diagram the 04:00 - 16:00 hours MLT component of convection is being measured, and no electric field is measured. This does not rule out the possibility that convection in the 10:00 - 22:00 direction persists at 1930 UT. Some of the variation in velocity magnitude between passes in Figure 28 may be ascribed to the different orientations of the satellite. However, a close examination, for instance of the convection zones at 1924 and 2121 UT, shows that in the 2 hours between passes the magnitude of the eastward convection component changes significantly, the width of the zone changes, and the invariant latitude of the reversal shifts by several degrees. Thus the time scales of the phenomena in this example are shorter than the two hours between passes, although the overall pattern persists.

The peak magnitudes of convection velocities observed in individual zones average 1.5 km/sec and include speeds greater than 5 km/sec. The maximum magnitudes of convection observed do not vary

systematically as a function of local time. In general the maximum convection velocities at latitudes above and below reversals are unequal.

In Figure 29 the average width of convection zones (excluding zones extending across the entire polar cap) is displayed as a function of MLT. The zones appear to be widest just before dawn and just after dusk. Figure 30 shows that the widths of the zones on each side of 112 reversals are often, but not necessarily, equal.

In about 14% of the reversals studied, the convection zone on the high latitude side of the reversal does extend across the polar cap, as shown in the top diagram of Figure 28. Figure 31 shows the largest example of this trans-polar convection encountered in the Injun 5 data. In most cases the magnitude of convection across the polar cap cannot be determined more accurately than ± 0.75 km/sec. In a few cases, due to slow spacecraft rotation or orientations precluding boom shadowing, the absolute magnitude of polar cap convection can be determined to be less than 0.25 km/sec. Figures 32, 33, and 34 show three of these cases. In these examples E_s can be drawn more accurately than ± 10 mV/meter, so the

convection velocity components determined are accurate to less than ± 0.25 km/sec. Figures 32, 33, and 34 indicate both that (1) (in these cases) \vec{V}_c is small (< 0.25 km/sec) over the center of the polar cap and (2) that the major convection (except near midnight) is in relatively narrow zones separated by electric field reversals at auroral zone latitudes. Thus transpolar convection is normally less than 0.75 km/sec, and sometimes less than 0.25 km/sec.

A catalogue of 112 examples of electric field/convection velocity reversals has been compiled (Cauffman and Gurnett, 1971b). The points in Figure 35 show the locations of these reversals in invariant latitude and magnetic local time. The relative occurrence of reversals as a function of MLT is determined by the satellite orbit and data coverage. It is evident in the figure that reversals tend to occur at 75° to 80° INV near noon, at 60° to 75° INV near midnight, and at intermediate invariant latitudes near dawn and dusk. Individual exceptions do occur. It is not known whether or not the cluster of reversals observed between 80° and 85° INV at dawn and dusk is a result of the greater amount of data which is available in those sectors. Table 7 lists the average INV for the 112 reversals, by local time sectors.

2. Convection Directions

The convection shown in Figures 24, 25, 26, 27, 28, 31, 32, 33, and 34 illustrates the persistent occurrence of reversals in the east-west direction of the convection in the auroral zone. In most of these cases the primary convection pattern is limited to a region several degrees in latitude on either side of the reversal with sunward convection generally observed on the low latitude side of the reversal and anti-sunward convection on the high latitude side of the reversal. Broad convection zones with velocities greater than 0.75 km/sec over the polar region, such as those evident in Figure 31, are less common.

Although only one component of convection velocity is measured, it is possible to deduce the general direction of the plasma flow from large numbers of observations. The points in Figure 35 are coded to show which of the 112 reversals studied had eastward flow components measured on the high latitude sides of the reversals, and which had westward components. (The directions of flow components measured on the low latitude sides of the reversals are opposite to those indicated, because the spacecraft does not rotate significantly in the time

required to detect a reversal.) It is clear from the figure that nearly all reversals which occur at magnetic local times between 0 and 12 hours have westward convection components measured on the high latitude sides of the reversals. Similarly, between 12 and 24 hours MLT, most reversals possess eastward flow components on their high-latitude sides. In Figure 36 the 112 reversals are analyzed with respect to pole-ward versus equator-ward measured flow components. The distribution appears to be random. Randomness would be expected, due to arbitrary satellite orientation, if the true convection direction were east or west. The contention that the true convection direction is east or west is further supported by the large numbers of reversals (see Figure 36) which have no north-south component, as compared to the few (see Figure 35) which have no east-west component. (Midnight may be an exception.) Table 8 summarizes the statistics concerning the convection directions. We conclude, on the basis of these statistical results and on the basis of interpretation of individual cases such as that at 1643 UT in Figure 26, that true convection directions are primarily westward at local times less

than about 12 hours, and eastward at local times greater than 12 hours, on the pole-ward sides of reversals.

Figure 37 summarizes the directions of >0.75 km/sec plasma convection associated with DC electric field reversals. The diagram has incorporated the evidence that (1) convection is ordinarily less than 0.75 km/sec over the polar cap, (2) zones may be wider just before dawn and after dusk, (3) even near noon, convection directions are east or west, not north or south, (4) near midnight some equator-ward convection may occur, (5) convection magnitudes are greatest nearest reversals, and (6) convection magnitudes may be greater at night than in day local times. It must be emphasized that this diagram represents a gross simplification of the actual convection. Major departures include (1) temporal variations of the latitude of the reversal, (2) variations in the position of the sunward neutral point of the magnetosphere by ± 2 hours MLT (as shown by the region of 'overlap' of east-west convection in Figure 35), (3) the occasional occurrence of anti-sunward convection (>0.75 km/sec) across the entire

polar cap, (4) the existence of multiple reversals, possibly associated with turbulence, and (5) the occasional disappearance of one or both of the two convection zones associated with a reversal.

3. Magnetic Activity Dependence

Figure 38 shows the maximum convection velocity magnitude versus the magnetic index K_p . A weak dependence may be deduced. However, in many cases large convection velocities occur when K_p is low, and conversely. The relative occurrence of reversals as a function of K_p is shown in Figure 39. Again there is weak dependence evident. A detailed comparison of convection with substorm phenomena is required to determine better the relationship between the convection magnitudes and magnetic activity. Such a study is in progress. It should be pointed out that the large-scale convection shown in Figure 31 occurred on a disturbed day when K_p was +4. Large disturbances in 7 north polar cap magnetograms occurred about an hour after this large trans-polar convection was first observed. However, in Figure 27 convection velocities observed range from less than 0.25 km/sec to 1.75 km/sec while K_p was 1 and 0, respectively.

4. Potentials

Figure 40 shows two oppositely-directed electric field zones separated by a region of zero electric field. This pass is of interest because the satellite was not rotating, and the electric antenna axis was parallel to the velocity vector, as illustrated in Figure 41. The orientation is fortunately such as to exclude all shadow effects. Under this (rather rare) set of circumstances the potential across the polar cap may be integrated directly from the electric field, assuming that the electric field is a spatial effect:

$$\phi = - \int \vec{E}_c \cdot d\vec{s} \quad (13)$$

The potential, plotted in the top of Figure 40, reaches 44,000 volts in about 2500 kilometers. The polar diagram in Figure 41 shows the convection velocity components implied by the measured electric field zones. Only the sunward/anti-sunward convection component is measured. The anti-sunward flow above 75° INV and sunward flow below 75° INV is consistent with the general directions of convection already discussed.

Not all electric field reversals occur on time scales of minutes. Figure 42 shows a reversal which changes from minimum to maximum (117 mV/meter) in 8 seconds. As the y axis at this time was aligned parallel to \vec{V}_g , the potential may again be found as indicated by Equation (13). The top of Figure 42 shows the potential obtained, which reaches 3600 volts in less than 100 km. The electric field in this example was measured every 4/30 second.

5. Association with Energetic Charged Particles

The association between DC electric field reversals and energetic charged particles has been investigated by Frank and Gurnett (1971). They have found that electric field reversals are coincident with the high latitude termination of measurable intensities of >45 keV energetic electrons, as shown in Figure 43. Also shown in this figure are the intensities of low energy protons and electrons measured by the LEPDEA detector on Injun 5 (cf. Frank et al., 1966). The peaks in the low energy electron intensities are an index to the location of inverted 'V' type precipitation events described by

Frank and Ackerson (1970). The average position of electric field reversals as shown in Figure 37 correlates well with the average position of visual aurora as reported by Feldstein (1966).

6. Summary

Electric field reversals are the most significant convection electric field effect identified in the Injun 5 DC electric field data. Electric field reversals occur on ~36% of the auroral zone traversals, at about 70° to 80° invariant latitude, and at all local times. They have been identified at magnetically conjugate points in both hemispheres. Amplitudes are often greater than 30 mV/meter, and occasionally greater than 100 mV/meter. The latitude and structure of a reversal often change markedly on time scales less than 2 hours. Electric potentials of greater than 40 keV are associated with reversals. Frank and Gurnett (1971) have shown that reversals occur at the boundary of measurable intensities of >45 keV electrons and are coincident with inverted 'V' low energy electron precipitation events. Generally the plasma convection velocities associated with reversals are directed east or west, with anti-sunward

components at higher latitudes and sunward components at lower latitudes, as summarized in Figure 37. Maximum convection velocities generally occur near reversals and average ~ 1.5 km/sec. Over the polar region above the auroral zone the convection velocity is usually small (generally less than 0.75 km/sec, and sometimes less than 0.25 km/sec) compared to convection velocities in the region of the reversal. Large scale anti-sunward convection across the magnetic poles with convection velocities exceeding 0.75 km/sec is occasionally observed.

IV. CONCLUSIONS

A. Comparison with Barium Cloud Measurements

Haerendel and Lust (1970) summarize recent results of measurements of plasma convection by the barium cloud drift technique. The requirement of twilight conditions restricts barium cloud measurements to the midnight sector and invariant latitudes generally below 70° . However, at local times nearer dawn, eastward drifts are observed, and near dusk, westward drifts. These directions are entirely consistent with the 'sunward' convection reported in this paper at dawn and dusk at comparable latitudes. Several cases of high latitude clouds which reverse drift directions have been reported. The magnitudes of convection electric fields we observe are consistent with those quoted by Wescott et al., (1969), who report intensities of 10 - 130 mV/meter. These authors also report that large irregularities in the electric field exist most of the time.

B. Comparison with Magnetospheric Models

High latitude convection is intimately tied to the topology of the outer magnetosphere and tail, and

probably to events and magnetic field directions in the solar wind as well. DC electric field reversals and the 'simple' convection pattern (Figure 37) they imply may represent an equilibrium configuration of this generally dynamic system.

Dungey (1961) suggested that the solar magnetic field could merge with the earth's magnetic field in an 'open' magnetospheric model. Field lines merged at the bow of the magnetosphere would be pulled across the polar caps by the solar wind and would reconnect on the earth's night side. Consequently there would be a return flow of field lines to the sunward side of the earth at lower latitudes. As charged particles would remain attached ('frozen') to field lines except near reconnection regions, bulk motion, or convection, of the magnetosphere would result. The measurements presented here of DC electric fields related directly to plasma convection, indicate that the large-scale (>0.75 km/sec) anti-solar convection flow across the polar caps implied by Dungey's model is not a normal feature of the magnetosphere. Figures 28 and 31 indicate, however, that such a convective

flow does sometimes occur, but the velocities are less than would be expected from a geometrical reduction of the solar wind velocity to satellite altitudes.

Axford and Hines' (1961) 'closed' magnetospheric model more explicitly suggested convection across the polar cap with return flow at the auroral zone, but used 'viscous interaction' with the solar wind at the magnetospheric boundary as the principal driving force. To the extent that their trans-polar flow was concentrated at auroral zone latitudes, the observations presented herein are consistent with the Axford and Hines model.

Frank (1970, 1971) uses observed energetic particle distributions to trace geomagnetic field lines to different regions of the magnetosphere. Frank and Gurnett (1971) show the agreement of this 'observational' model of the magnetosphere (see Figure 44) based on the magnetic field structure deduced from the observed particle spectra, with the convection inferred from the observations of electric field reversals presented here. In this magnetospheric model the convecting field lines at latitudes just above reversals are those which have been connected to the interplanetary magnetic field at

the polar cusp (field lines B and b in Figure 44). These field lines are drawn back into the plasma sheet (field lines B' and b') by the solar wind. In the plasma sheet they become reconnected (field lines A) and return to the sunward side of the magnetosphere (field lines A'), convecting plasma in the ionosphere towards the sun on the low-latitude sides of reversals. The pattern of convection which results at ionospheric levels is thus in agreement with that presented in Figure 37.

C. Comparison with Models of Substorms and Aurorae

The short time scales we observe for major changes in the magnetospheric electric fields measured, suggest ties with magnetic substorm phenomena. The same essential features of high latitude convection, anti-sunward trans-polar flow and auroral zone return paths, appear in the magnetic substorm equivalent current systems derived by Nishida (1967), Heppner (1969), Wescott et al. (1969), and others, on the basis of ground magnetometer measurements. These currents are assumed to be concentrated in the ionosphere. Usually we observe >0.75 km/sec anti-solar convection to be concentrated in the auroral zone, rather than spread across the polar cap. However,

we do at times (cf. Figures 28 and 31) see trans-polar flow components, and since the substorm current pattern is presumably a transitory feature of the ionosphere, these theories may explain the strong convection sometimes observed across the polar cap.

A competing theory of magnetic substorms utilizes a 3-dimensional current system with field aligned currents (Boström, 1967; Bonnevier, et al., 1970; Akasofu and Meng, 1969). A current is assumed to flow through the ionosphere (auroral electrojet) from dawn to dusk, then outward along a dusk magnetic field line. There the ring current, which drives the system, connects dusk to dawn, where the current flows inward along a field line. The effects of such field-aligned currents in the ionosphere have been investigated theoretically by Block and Fälthammar (1968), leading to a theory of space-charge regions above aurorae (Carlqvist and Boström, 1970). One of the consequences of such a space-charge region is the existence of a current slab above the aurora containing a north-south electric field which reverses in the center of the slab. The fields will point towards the center if the field-aligned current

is upwards, and away from the slab center if the field-aligned current is downwards. The electric fields are then presumed to cause $\vec{E} \times \vec{B}/B^2$ drifts. With the current system postulated, these drifts will be sunward at latitudes below the aurora and anti-sunward at higher latitudes. These fields and drifts are entirely consistent with our observations of the predominant directions of reversals. Carlqvist and Boström predict potentials at the center of the slabs of $10^3 - 10^5$ volts, and this is consistent with the 3600 volt and 44,000 volt examples shown in Figures 40 and 42. However, one must assume slab widths of $10^2 - 10^3$ kilometers to make the range of convection velocities predicted encompass the range of velocities we observe.

The large potentials, >40 keV, observed between magnetic field lines associated with reversals, and the coincidence of inverted 'V' electron precipitation events with electric field reversals (Frank and Gurnett, 1971) suggest that an acceleration mechanism involving electric fields parallel to magnetic field lines is operating to energize magnetospheric plasma. This interpretation is discussed in detail by Frank and Gurnett (1971).

APPENDIX

Solution for Photo-Electron Current

The impedance measured by the Injun 5 VLF plasma impedance experiment at 30 Hz is the average of the resistances of the plasma sheaths around the two electric field probes. For the normal case of negative probe potential, Equation (5a) gives the sheath resistance in terms of plasma parameters and probe dimensions according to Fahleson (1967). In an unshadowed situation the measured impedance will be

$$Z_o = \frac{1}{2} \left[\frac{U_e}{I_i + I_{p+}} + \frac{U_e}{I_i + I_{p-}} \right].$$

We shall assume that $I_p = I_{p+} = I_{p-}$, so

$$Z_o = \frac{U_e}{I_i + I_p}. \quad (A1)$$

If one sphere is shadowed, the measured impedance will be

$$Z_s = \frac{1}{2} \left[\frac{U_e}{I_i + I_p} + \frac{U_e}{I_i} \right]. \quad (A2)$$

The change in measured electric field, ΔE_M , when $I_p = 0$ for just one sphere and $R_s \ll R_B$, is found from Equations (4a), (6), and (8) to be

$$\Delta E_M = \frac{U_e}{\ell} \ln \frac{I_i + I_p}{I_i} . \quad (A3)$$

The three equations (A1), (A2), and (A3) may be algebraically solved for the unknowns U_e , I_i , and I_p , in terms of Z_s , Z_o , and ΔE_M , in spite of the non-linearity evident in Equation (A3). The solution for I_p is

$$I_p = \frac{\left(\frac{Z_s}{Z_o} - 1 \right) \ell \Delta E_M}{\left(2Z_s - Z_o \right) \ln \left(\frac{2Z_s}{Z_o} - 1 \right)} . \quad (A4)$$

The photo-electron current I_p may be found from Equation (A4) when one sphere is completely shadowed by determining the change in measured electric field, ΔE_M , the impedance, Z_o , just before or after the shadow occurs, and the impedance, Z_s , measured during the shadow occurrence. While the accuracy of the solution is limited by the approximation $I_p = I_{p+} = I_{p-}$ and by the fact that the fundamental equations used are for 'small' bias currents, nevertheless the result should be more accurate than the linear 'Ohm's law' assumption

$$I_p = \frac{2 |\Delta E_M|}{Z_o} . \quad (A5)$$

Figure 10 shows that the effect of using Equation (A4) (top graph) instead of Equation (A5) (bottom graph) is to reduce I_p . There are fewer cases considered in the top graph because for many of the shadows in the study (see Section IID) the natural impedance variations were of the same magnitude as the changes produced by the shadow, and Equation (A4) is invalid if $Z_o \geq Z_s$.

LIST OF REFERENCES

- Aggson, T. A., A proposal for tri-axial electric field measurements on IMP spacecraft H, I, and J, NASA-Goddard Space Flight Center preprint (1966).
- Akasofu, S. I., and C. I. Meng, A study of solar magnetic substorms, J. Geophys. Res., 74(1), 293-313 (1969).
- Alfvén, H., On the importance of electric fields in the magnetosphere and interplanetary space, Space Science Reviews, 7, 140-148 (1967).
- Axford, W. I., Magnetospheric convection, Reviews of Geophys., 7, 421-259 (1969).
- Axford, W. I., and C. O. Hines, A unifying theory of high-latitude geophysical phenomena and geomagnetic storms, Can. J. Phys., 39, 1433-1464 (1961).
- Block, L. P., and C.-G. Fälthammar, Effects of field-aligned currents on the structure of the ionosphere, J. Geophys. Res., 73(15), 4807-4812 (1968).
- Bonnevier, B., R. Boström, and G. Rostocker, A three-dimensional model current system for polar magnetic substorms, J. Geophys. Res., 75(1), 107-122 (1970).
- Boström, R., Auroral electric fields, Aurora and Airglow, B. M. McCormac, ed., Reinhold Book Corp. (New York), 293-303 (1967).
- Brace, L. H., B. M. Reddy, and H. G. Mayr, Global behavior of the ionosphere at 1000 kilometer altitude, J. Geophys. Res., 72(1), 265-283 (1967).

LIST OF REFERENCES (cont'd.)

- Cain, J. C., S. J. Hendricks, R. A. Langel, and V. W. Hudson, A proposed model for the international geomagnetic reference field -- 1965, J. Geomagn. Geoelec., 19, 335 (1967).
- Carlqvist, P., and R. Boström, Space charge regions above the aurora, J. Geophys. Res., 75(34), 7140-7146 (1970).
- Carpenter, D. L., Whistler evidence of the dynamic behavior of the duskside bulge in the plasmasphere, J. Geophys. Res., 75(19), 3837-3847 (1970).
- Cauffman, D. and D. Gurnett, Double probe measurements of DC electric fields with the Injun 5 satellite, U. of Iowa 71-3 (University of Iowa Research Report, 1971a).
- Cauffman, D. and D. Gurnett, Catalogue of DC electric field reversals observed with the Injun 5 satellite, U. of Iowa 71-10 (University of Iowa Research Report, 1971b).
- Dungey, J. W., Interplanetary magnetic field and the auroral zone, Phys. Rev. Letters, 6, 47-48 (1961).
- Fahleson, U. V., Theory of electric field measurements conducted in the magnetosphere with electric probes, Space Sci. Rev., 7, 238-262 (1967).
- Fahleson, U. V., M. C. Kelley, and F. S. Mozer, Investigation of the operation of a DC electric field detector, Planet. Space Sci., 18, 1551-1561 (1970).
- Feldstein, Y. I., Peculiarities in the auroral distribution and magnetic disturbance distribution in high latitudes caused by the asymmetrical form of the magnetosphere, Planet. Space Sci., 14, 121-130 (1966).

LIST OF REFERENCES (cont'd.)

- Föppl, H., G. Haerendel, L. Haser, R. Lust, F. Melzner, B. Meyer, H. Neuss, H. Rabben, E. Rieger, H. Stocker, and W. Stoffregen, Preliminary results of electric field measurements in the auroral zone, J. Geophys. Res., 73, 21-26 (1968).
- Frank, L. A., Plasma in the earth's polar magnetosphere, U. of Iowa 70-55 (University of Iowa Research Report, 1970).
- Frank, L. A., Comments on a proposed magnetospheric model, J. Geophys. Res., 76(10), 2512-2515 (1971).
- Frank, L. A., and K. L. Ackerson, Observations of charged particle precipitation into the auroral zone, U. of Iowa 70-44 (University of Iowa Research Report, 1970).
- Frank, L. A. and D. A. Gurnett, On the distributions of plasmas and electric fields over the auroral zones and polar caps, U. of Iowa 71-5 (University of Iowa Research Report, 1971).
- Frank, L. A., W. W. Stanley, R. H. Gabel, D. C. Enemark, R. F. Randall, and N. K. Henderson, Technical description of LEPDEA instrumentation (Injun 5), U. of Iowa 66-31 (University of Iowa Research Report, 1966).
- Gurnett, D. A., Satellite measurements of DC electric fields in the ionosphere, Particles and Fields in the Magnetosphere, B. M. McCormac, ed., Reinhold Book Company (Dordrecht, Holland), 239-246 (1970).
- Gurnett, D. A., G. W. Pfeiffer, R. R. Anderson, S. R. Mosier, and D. P. Cauffman, Initial observations of VLF electric and magnetic fields with the Injun 5 satellite, J. Geophys. Res., 74(19), 4631-4648 (1969).

LIST OF REFERENCES (cont'd.)

- Haerendel, G., and R. Lüst, Electric fields in the ionosphere and magnetosphere, Particles and Fields in the Magnetosphere, B. M. McCormac, ed., Reinhold Book Company (Dordrecht, Holland), 213-228 (1970).
- Haerendel, G., R. Lüst, and E. Reiger, Motion of artificial ion clouds in the upper atmosphere, Planet. Space Sci., 15, 1-18 (1967).
- Heppner, J. P., Magnetospheric convection patterns inferred from high-latitude activity, Atmospheric Emissions, B. M. McCormac and A. Omholt, eds., Van Nostrand Reinhold Co. (New York), 251-266 (1969).
- Kasha, Michael A., The Ionosphere and its Interaction with Satellites, Gordon and Breach (New York), (1969).
- Maynard, N. C., and J. P. Heppner, Variations in electric fields from polar orbiting satellites, Particles and Fields in the Magnetosphere, B. M. McCormac, ed., Reinhold Book Company (Dordrecht, Holland), 247-253 (1970).
- Mende, S. B., Experimental investigation of electric fields parallel to the magnetic field in the auroral ionosphere, J. Geophys. Res., 73(3), 991-997 (1968).
- Mozer, F. S., and P. Bruston, Electric field measurements in the auroral ionosphere, J. Geophys. Res., 72(3), 1109-1114 (1967).
- Mozer, F. S., and R. Serlin, Magnetospheric electric field measurements with balloons, J. Geophys. Res., 74(19), 4739-4754 (1969).

LIST OF REFERENCES (cont'd.)

- Nishida, A., Average structure and storm-time change of the polar topside ionosphere at sunspot minimum, J. Geophys. Res., 72(23), 6051-6061 (1967).
- Piddington, J. H., A hydromagnetic theory of geomagnetic storms and auroras, Planet. Space Sci., 9, 947-957 (1962).
- Potter, W. E., Rocket measurements of auroral electric and magnetic fields, J. Geophys. Res., 75(28), 5415-5431 (1970).
- Van Allen, J. A., On the electric field in the earth's distant magnetotail, J. Geophys. Res., 75(1), 29-38 (1970).
- Wescott, E. M., J. D. Stolarik, and J. P. Heppner, Electric fields in the vicinity of auroral forms from motions of barium vapor releases, J. Geophys. Res., 74(14), 3469-3487 (1969).
- Wildman, P. J. L., A device for measuring electric field in the presence of ionisation, J. Atmos. Terres. Phys., 27, 417-423 (1965).

Table 1

Parameters of the DC Electric Field Experiment

Sphere separation distance	2.85 meters between centers
radius	0.1015 meters
coating	conducting silver paint with gold dots for thermal control
Boom coating	black insulating paint
diameter	0.019 meters
Differential amplifier dynamic range	± 1.0 volt
RC time constant	0.4 second
input impedance to each sphere	20 megohms
Electric field sampling rate	
normal data rate mode	every 4 seconds
high data rate mode	every 4/30 second
Tape recorder storage capacity (normal data rate only)	456 minutes of data
Impedance measurement frequency	32 Hz
sampling rate	every 30 seconds
constant current	0.1 μ amp RMS

Table 2

Injun 5 Orbital Data

Date of launch	August 8, 1968
Date of alignment with the geo-magnetic field	December 3, 1968
Maximum alignment error after alignment date	$\pm 15^\circ$
Orbital period	118 minutes
Inclination	80.7°
Apogee	2528 km
Perigee	677 km
Orbital precession rate	12 hours LT in 103 days
Velocity	6.4 to 7.9 km/sec

Table 3

Occurrence of Wake Effects

Altitude (Kilometers)	Impedance (Ohms)		
	$10^4 - 9 \times 10^5$	$10^5 - 9 \times 10^6$	$>10^6$
>2500	(0)	5% (22)	55% (11)
2000 - 2400	(0)	11% (27)	58% (52)
1500 - 1900	(0)	15% (106)	76% (21)
1000 - 1400	0% (2)	4% (119)	100% (1)
500 - 900	3% (31)	0% (53)	(0)
All Altitudes	3% (33)	8% (327)	62% (85)

Numbers in parentheses indicate number of samples

Total number of samples (probe within $\pm 30^\circ$ of $-\vec{V}_s$): 445

Table 4

Probe Potential in the Spacecraft Wake

	Sphere 1		Sphere 2	
+ potential ¹	95%	(54)	88%	(22)
- potential ¹	5%	(3)	12%	(3)
both potentials ²	26%	(57)	11%	(25)
total samples		(222)		(229)

Numbers in parentheses indicate number of samples (probe within 30° of $-\vec{V}_s$)

¹ Percent of samples for this sphere exhibiting wake effects

² Percent of total samples for this sphere

Table 5

Standard Parameters Used in Probe Model Calculation

<u>Symbol</u>	<u>Quantity</u>	<u>Value</u>
T_e	electron temperature	2500 °K
T_i	ion temperature	1500 °K
n	number density of ions or electrons	10^3 to 10^6 parti- cles/cm ³
\vec{V}_s	satellite velocity	7 km/sec
r	radius of sphere	0.1015 meter
l	sphere separation	2.85 meters
r_b	spacecraft body radius	0.305 meter
E_y	electric field component measured	350 mV/meter
R_{B+}	bias resistance: +y sphere branch	$2.0 \times 10^7 \Omega$
R_{B-}	bias resistance: -y sphere branch	$1.9 \times 10^7 \Omega$
U_p	photo-electron potential kT_p/e	1.5 volts
m_i	ion mass	16 amu
I_{p+}	photo-electron current to +y sphere	3×10^{-6} amp

Table 5 (cont'd.)

<u>Symbol</u>	<u>Quantity</u>	<u>Value</u>
I_{p-}	photo-electron current to -y sphere	2×10^{-6} amp
I_{pb}	photo-electron current to spacecraft body	7.5×10^{-6} amp

Table 6

DC Electric Field Phenomena Observed
at the Auroral Zone

	<u>number of cases</u>	<u>percent occurrence</u>
Single convection zones	66	23
Reversals (two oppositely- directed convection zones)	102	36
Noise (multiple convection zones)	57	20
Noise extending across the polar cap	25	9
Quiet ($ E_c < 10$ mV/meter)	<u>36</u>	13
Total	286	

Table 7

Average Invariant Latitude of Reversals

<u>MLT</u> <u>(hours)</u>	<u>number of</u> <u>cases</u>	<u>average invariant</u> <u>latitude (degrees)</u>
0 - 3	8	69.7
3 - 6	25	76.7
6 - 9	34	77.5
9 - 12	3	78.5
12 - 15	12	77.0
15 - 18	10	75.3
18 - 21	14	73.0
21 - 24	6	70.5

Table 8

Directions of Convection Components*

MLT Sector	Number of Cases			
	Eastward Components	Westward Components	No East-West Component	Total Cases
0 - 3	1	5	2	8
3 - 6	1	23	1	25
6 - 9	1	31	2	34
9 - 12	1	2	0	3
12 - 15	8	4	0	12
15 - 18	10	0	0	10
18 - 21	12	2	0	14
21 - 24	3	1	2	6

Table 8 (cont'd.)

MLT Sector	Number of Cases			Total Cases
	Pole-ward Components	Equator-ward Components	No North-South Component	
0 - 3	6	2	0	8
3 - 6	6	14	5	25
6 - 9	12	16	6	34
9 - 12	2	1	0	3
12 - 15	2	6	4	12
15 - 18	3	5	2	10
18 - 21	2	8	4	14
21 - 24	2	4	0	6

*Directions given correspond to the high latitude side of electric field reversals. Convection directions on the low latitude side of reversals are opposite to those indicated.

FIGURE CAPTIONS

- Figure 1 Orientation of electric antennas on the Injun 5 satellite.
- Figure 2 Top: Schematic representation of the currents to a Langmuir probe.
Bottom: Current-voltage characteristic of a probe.
- Figure 3 Top: Schematic illustration of the plasma sheath.
Bottom: Equivalent circuit of the probe-plasma system.
- Figure 4 Measured electric field, electric antenna impedance, and electron number density for a complete orbit of Injun 5 in the dawn-dusk plane.
- Figure 5 Measured electric field, electric antenna impedance, and electron number density for a complete orbit of Injun 5 in the noon-midnight plane.
- Figure 6 Examples of the effects of shadows of the spacecraft body on the electric field probes.
- Figure 7 Measured DC electric field E_M , subtracted curve E_s , and magnitude of electric field due to satellite motion, $\pm |\vec{V}_s \times \vec{B}|$, for a noon-midnight satellite orbit. The contact potential has been subtracted from the data shown.
- Figure 8 Examples of (1) change of E_M toward zero and (2) rectification spikes sometimes observed at the edge of the earth's umbra.

- Figure 9 Spacecraft wake effects observed on 3 successive high-altitude passes.
- Figure 10 Top: Photo-electron currents to the two electric antenna spheres for 47 shadow occurrences, calculated using the analytic solution for I_p described in the Appendix.
Bottom: Photo-electron currents for 86 shadow occurrences calculated using the linear approximation.
- Figure 11 Theoretical curves of probe floating potential as a function of electron number density and temperature.
- Figure 12 Values of the Debye length and sheath thickness calculated for electron number densities encountered in the Injun 5 orbit.
- Figure 13 Theoretical floating potential values of the electric antenna spheres and spacecraft body in sunlight and darkness.
- Figure 14 Sheath resistances $\frac{\partial V}{\partial I}$ corresponding to the potentials shown in Figure 13.
- Figure 15 Comparison of measured and calculated values of the probe sheath resistance.
- Figure 16 Values of the terms E_1 and E_2 (see Equation (9)) calculated for sunlight and shadow conditions.
- Figure 17 Calculated changes in the values of E_1 and E_2 (see Equation (9)) caused by large electron number density (top) and temperature (bottom) variations in the plasma at both probes.
- Figure 18 Calculated changes in the values of E_1 and E_2 caused by very large electron temperature (top) and number density (bottom) differences between the spheres.

Figure 19 Comparison of Injun 5 DC electric field and electron number density fluctuations taken at apogee.

Figure 20 Comparison of Injun 5 DC electric field and electron number density fluctuations taken at apogee.

Figure 21 Comparison of Injun 5 DC electric field and electron number density fluctuations taken at apogee.

Figure 22 Comparison of Injun 5 DC electric field and electron number density fluctuations taken at apogee.

Figure 23 Measured DC electric field E_M , subtracted curve E_S , and calculated $\hat{y} \cdot \vec{V}_S \times \vec{B}$ electric field for a complete dawn-dusk satellite orbit.

Figure 24 Example of a polar pass illustrating the data reduction procedure. Left: The convection electric field is assumed to be given by $E_c = E_M - E_S$. Right: Arrows representing the magnitude and direction of the component of convection velocity calculated from $\vec{V}_c = (\vec{E}_c \times \vec{B})/B^2$. The arrow does not represent the true convection velocity, but only the one component measured.

Figure 25 Convection velocity reversals inferred from DC electric field measurements on three days of January, 1969. (Only the one measured component of the actual convection velocity is shown).

Figure 26 Convection velocity reversals observed to occur on conjugate ends of the same geomagnetic field lines, one hour apart.

Figure 27 Components of plasma convection measured on six polar passes during a magnetically quiet period.

Figure 28 Pairs of convection velocity reversals observed at dawn and dusk MLT on three successive passes over the northern polar cap.

Figure 29 Average width of the convection zones on the high and low latitude sides of electric field reversals as a function of magnetic local time. The error bars give average deviations.

Figure 30 Comparison of the width of convection zones on the high and low latitude sides of 112 reversals.

Figure 31 Large-scale anti-sunward convection observed over both poles during a magnetically disturbed period.

Figure 32 DC electric fields and derived plasma convection velocity components observed when the satellite was slowly rotating. The accuracies of the measurements in these favorable circumstances are ± 10 mV/meter for $E_c = E_M - E_s$ and ± 0.25 km/sec for $\vec{V}_c = \vec{E}_c \times \vec{B}/B^2$.

Figure 33 DC electric fields and derived plasma convection velocity components observed when the satellite was slowly rotating. The accuracies of the measurements in these favorable circumstances are ± 10 mV/meter for $E_c = E_M - E_s$ and ± 0.25 km/sec for $\vec{V}_c = \vec{E}_c \times \vec{B}/B^2$.

Figure 34 DC electric fields and derived plasma convection velocity components observed when the satellite was slowly rotating. The accuracies of the measurements in these favorable circumstances are ± 10 mV/meter for $E_c = E_M - E_s$ and ± 0.25 km/sec for $\vec{V}_c = \vec{E}_c \times \vec{B}/B^2$.

Figure 35 Locations in invariant latitude and magnetic local time of 112 reversals. The points are coded to show whether the measured component of convection velocity on the high latitude side of each reversal had eastward or westward components.

Figure 36 Points corresponding to those in Figure 35 showing whether the measured component of convection velocity on the high latitude side of each reversal had pole-ward or equator-ward components.

Figure 37 Schematic diagram showing the average location and normal directions of >0.75 km/sec convection of thermal plasma at low altitudes in the magnetosphere as derived from measurements of DC electric fields with the Injun 5 satellite.

Figure 38 Maximum magnitude of the measured convection velocity component in the zones associated with 112 reversals, as a function of the magnetic index K_p .

Figure 39 Occurrence of reversals (see Table 6) for 286 auroral zone crossings, displayed as a function of the magnetic activity index K_p . The error bars give $\pm N^{-1/2}$.

Figure 40 Electric field measured parallel to the satellite path for a southern polar cap pass at low altitude, and the corresponding potential

$$\phi = - \int \vec{E}_c \cdot d\vec{s}.$$

Figure 41 Convection velocity components corresponding to the electric fields shown in Figure 40.

Figure 42 Example of a very rapid reversal in the north-south convection electric field.

Figure 43 (After Frank and Gurnett, 1971)
Simultaneous observations of proton and electron intensities at local pitch angle $\alpha = 90^\circ$ and of DC electric fields for a northern polar pass in March, 1970.

Figure 44 (After Frank and Gurnett, 1971)
Schematic diagram showing the relationship of plasma and convection regions at low altitudes with the topology and plasma regimes of the distant magnetosphere.

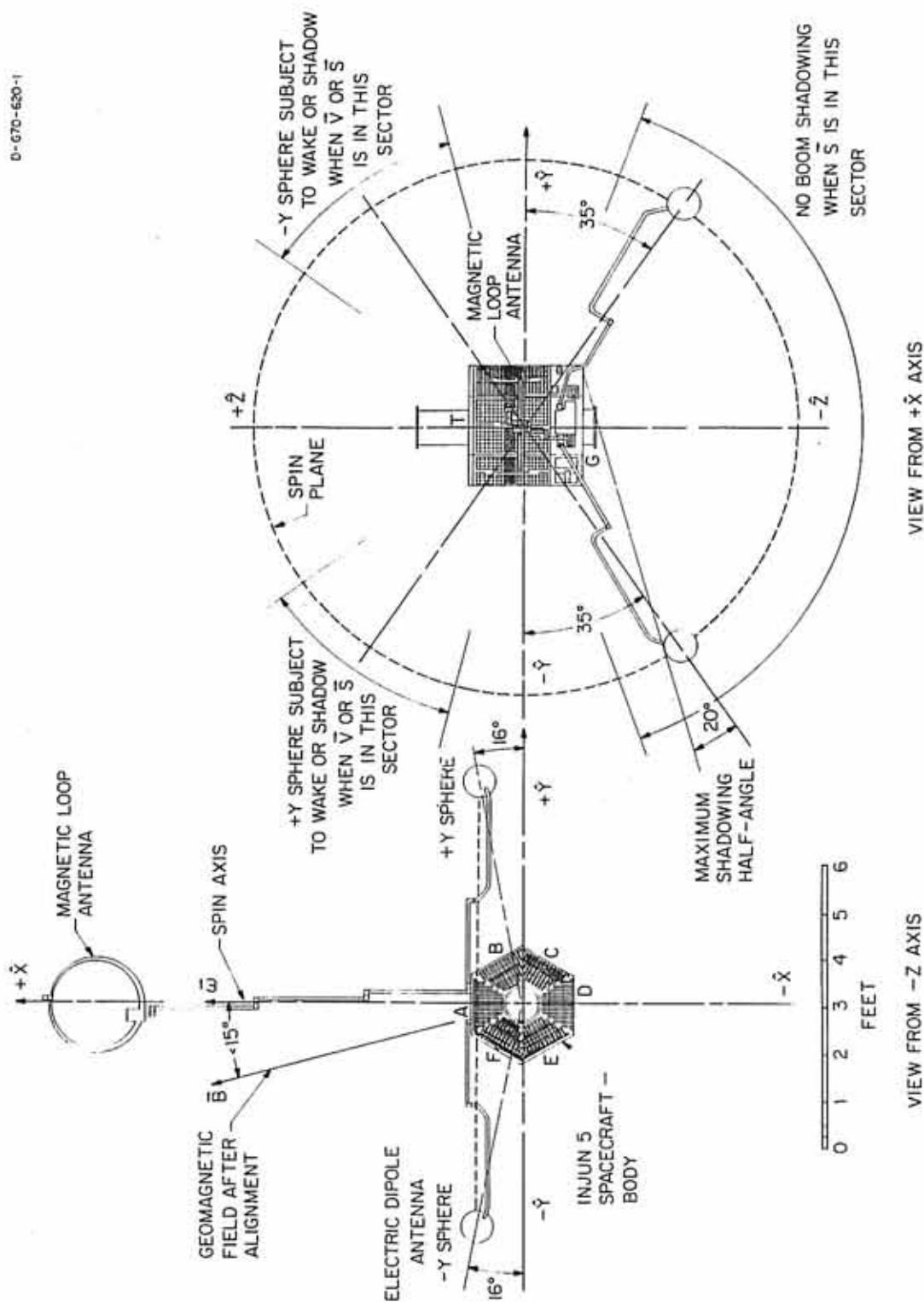


Figure 1

C - 671-63

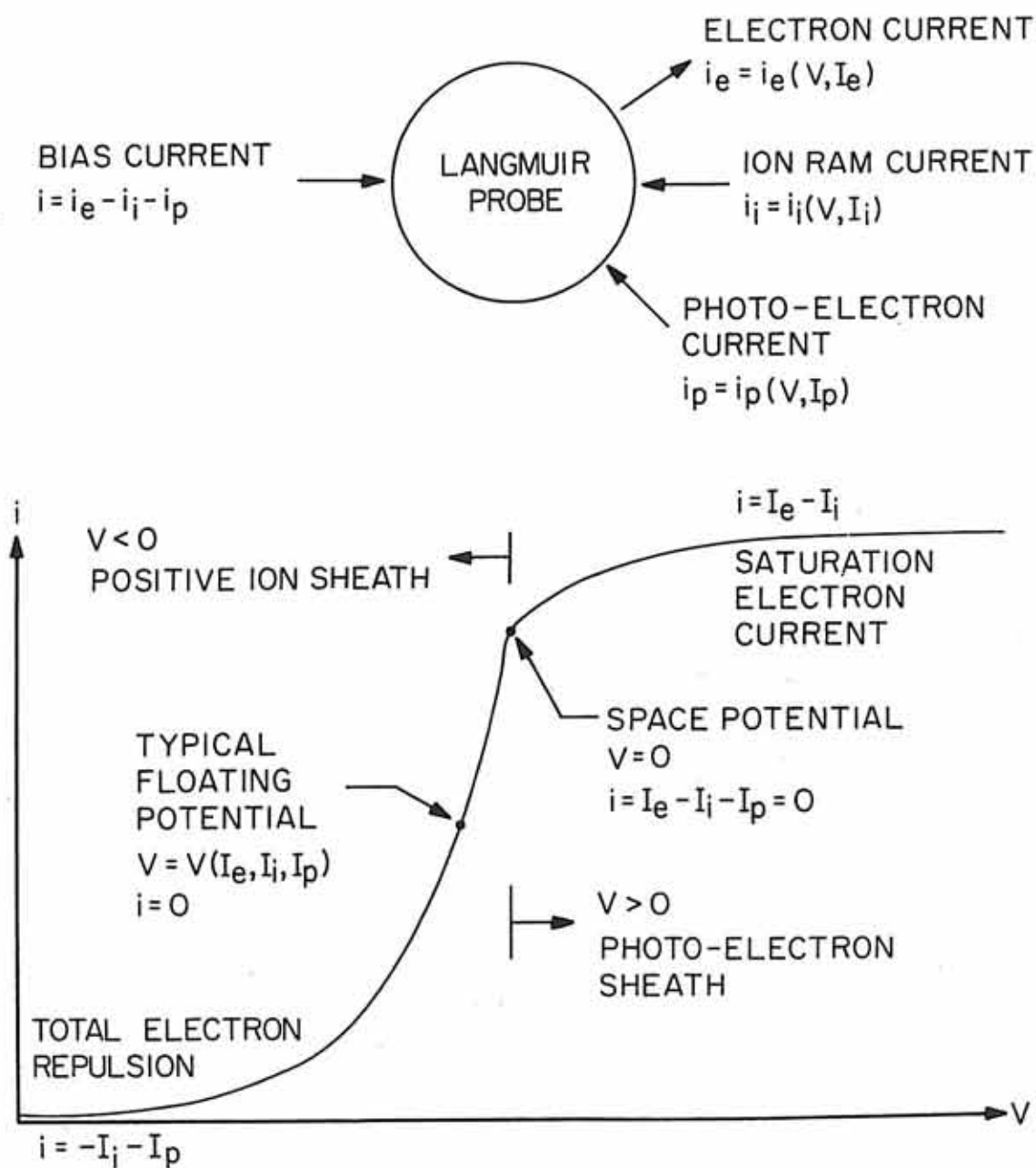


Figure 2

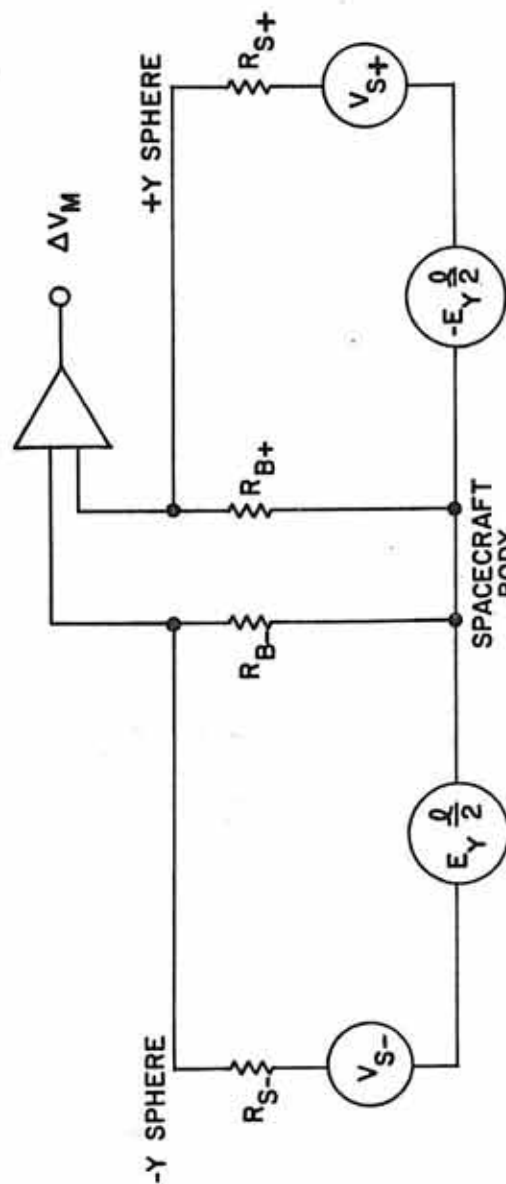
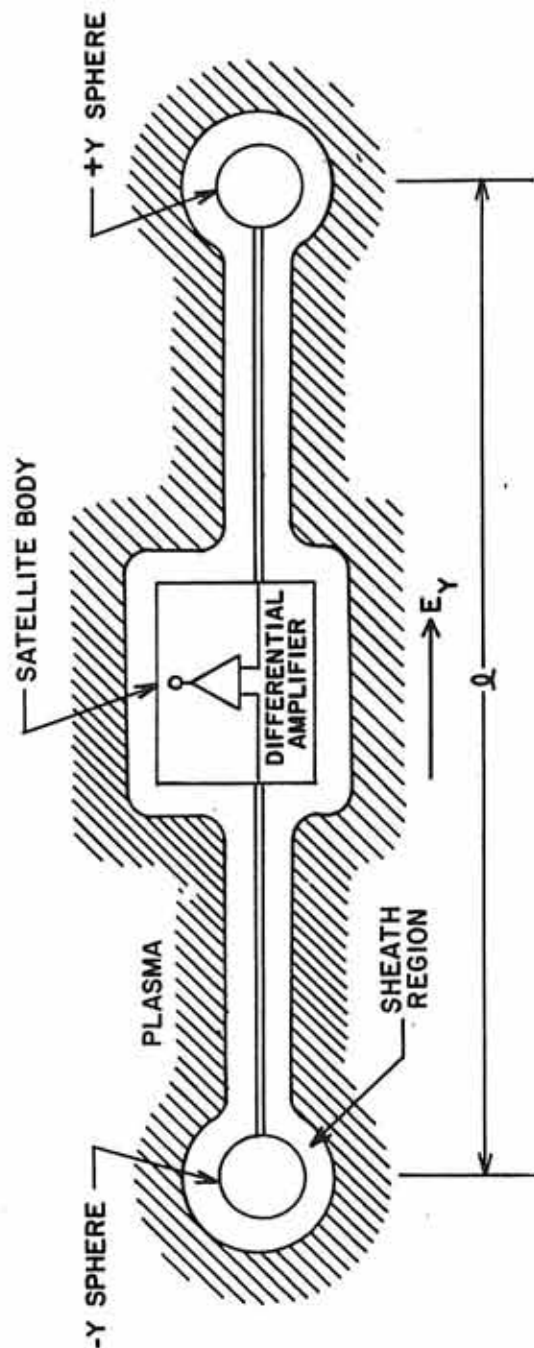


Figure 3

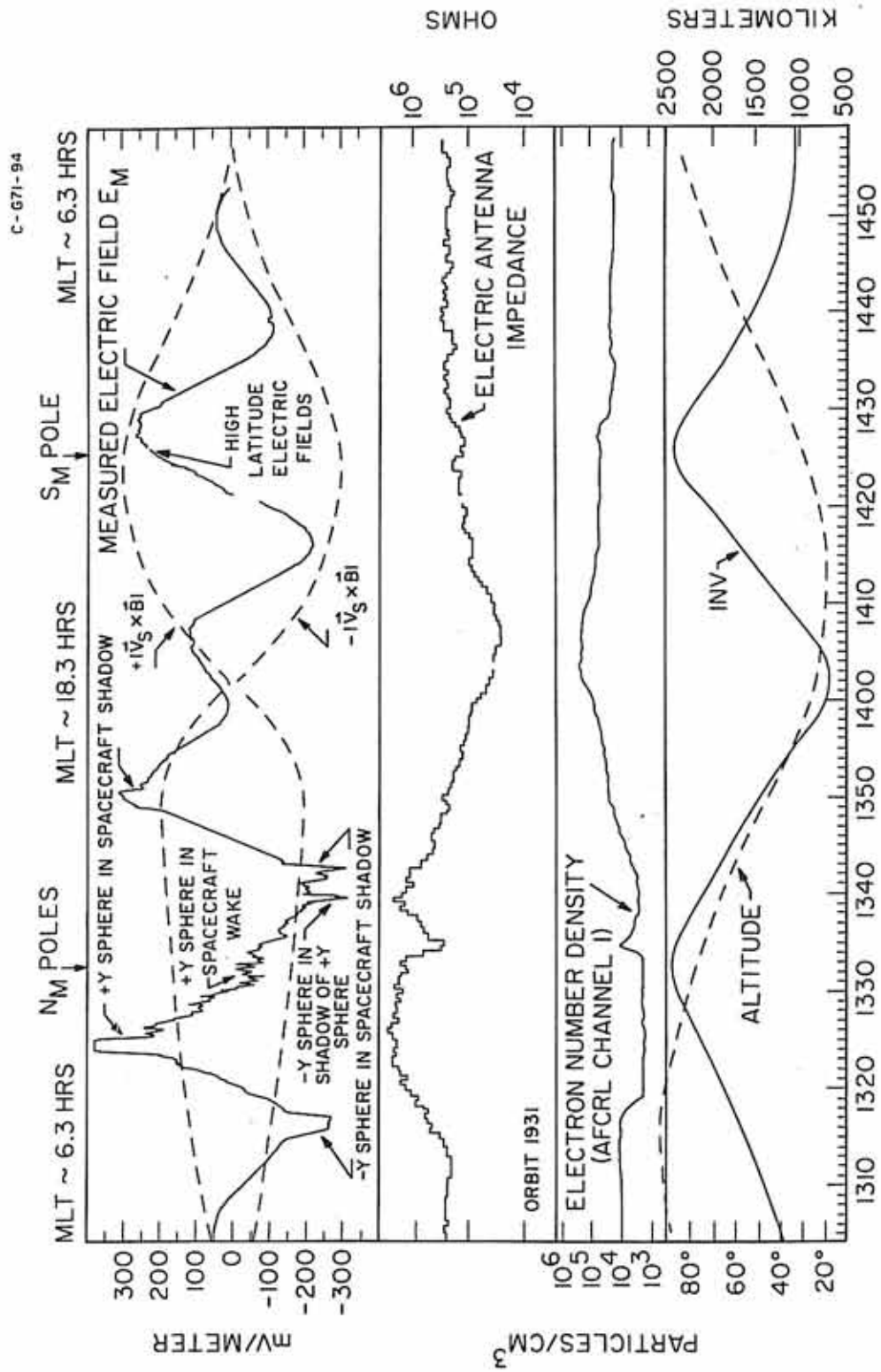


Figure 4

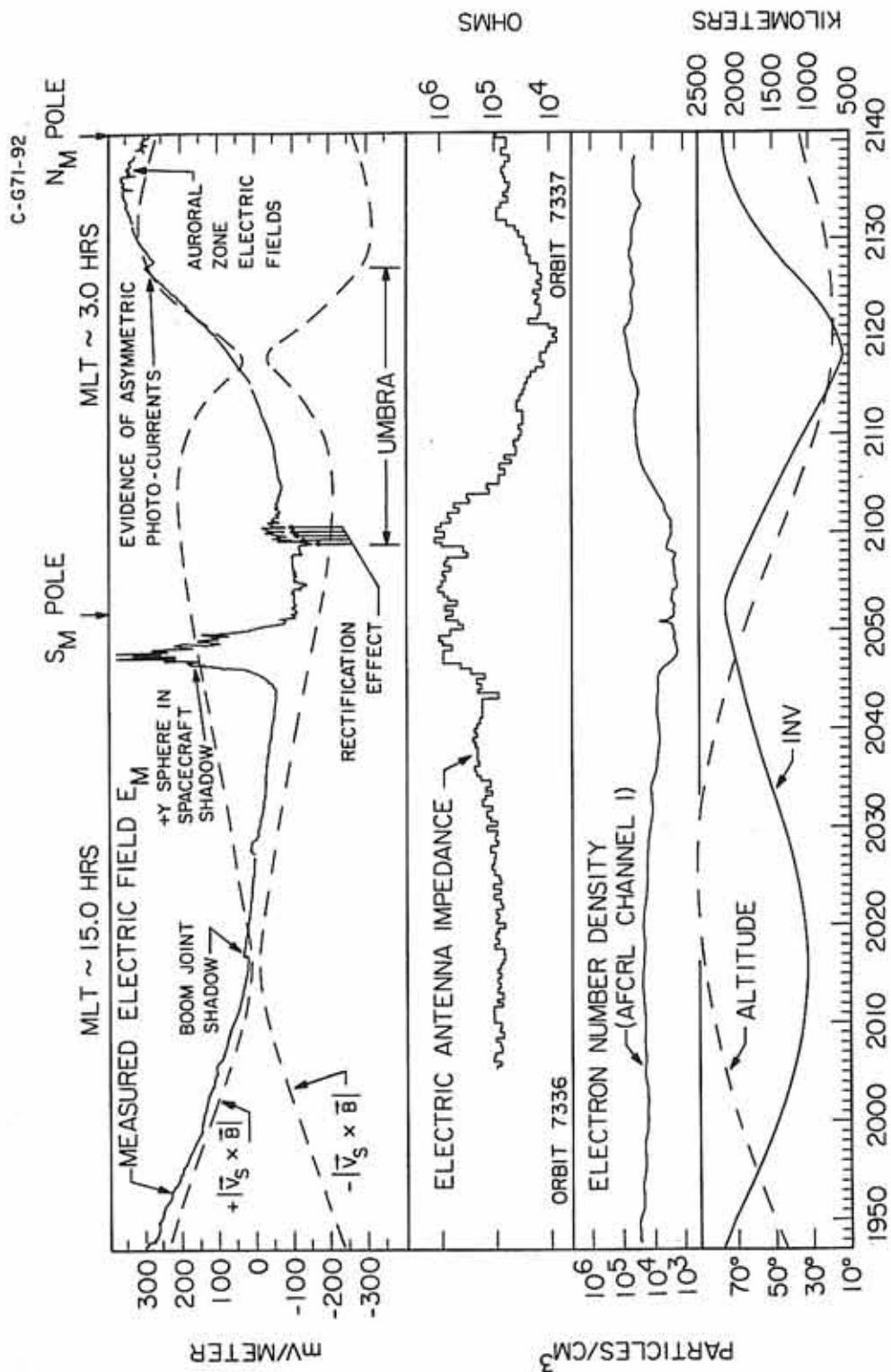


Figure 5

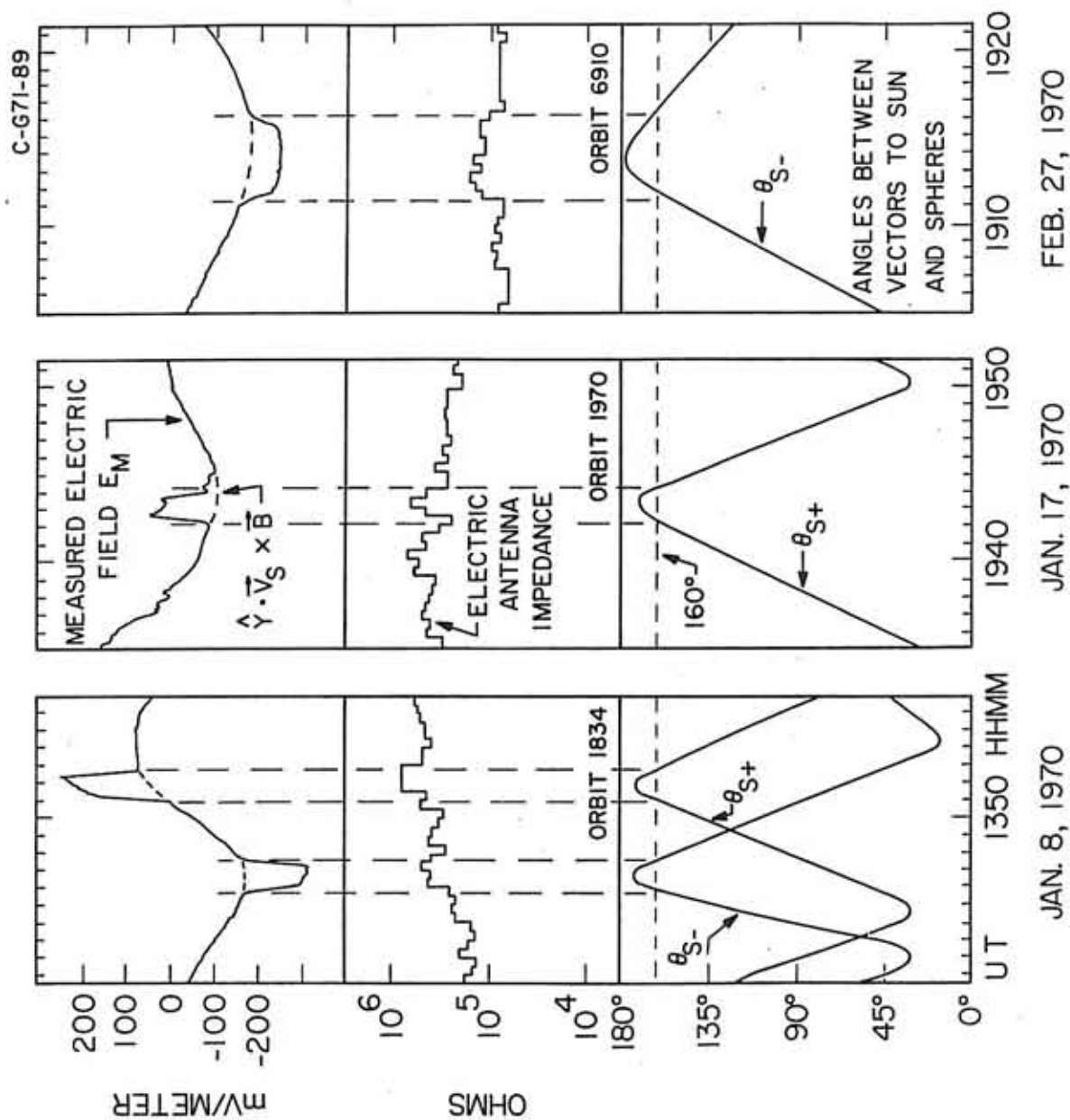


Figure 6

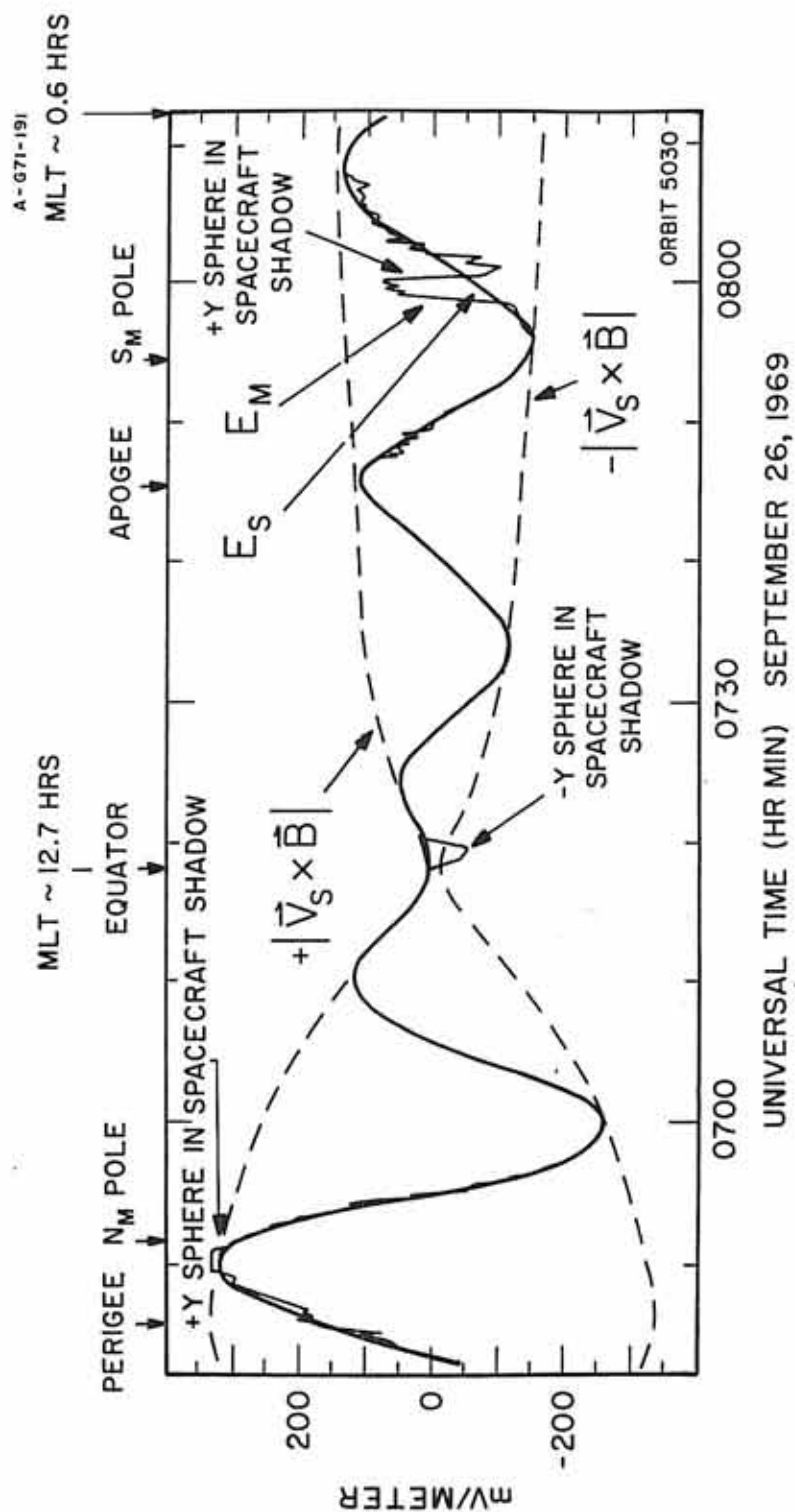
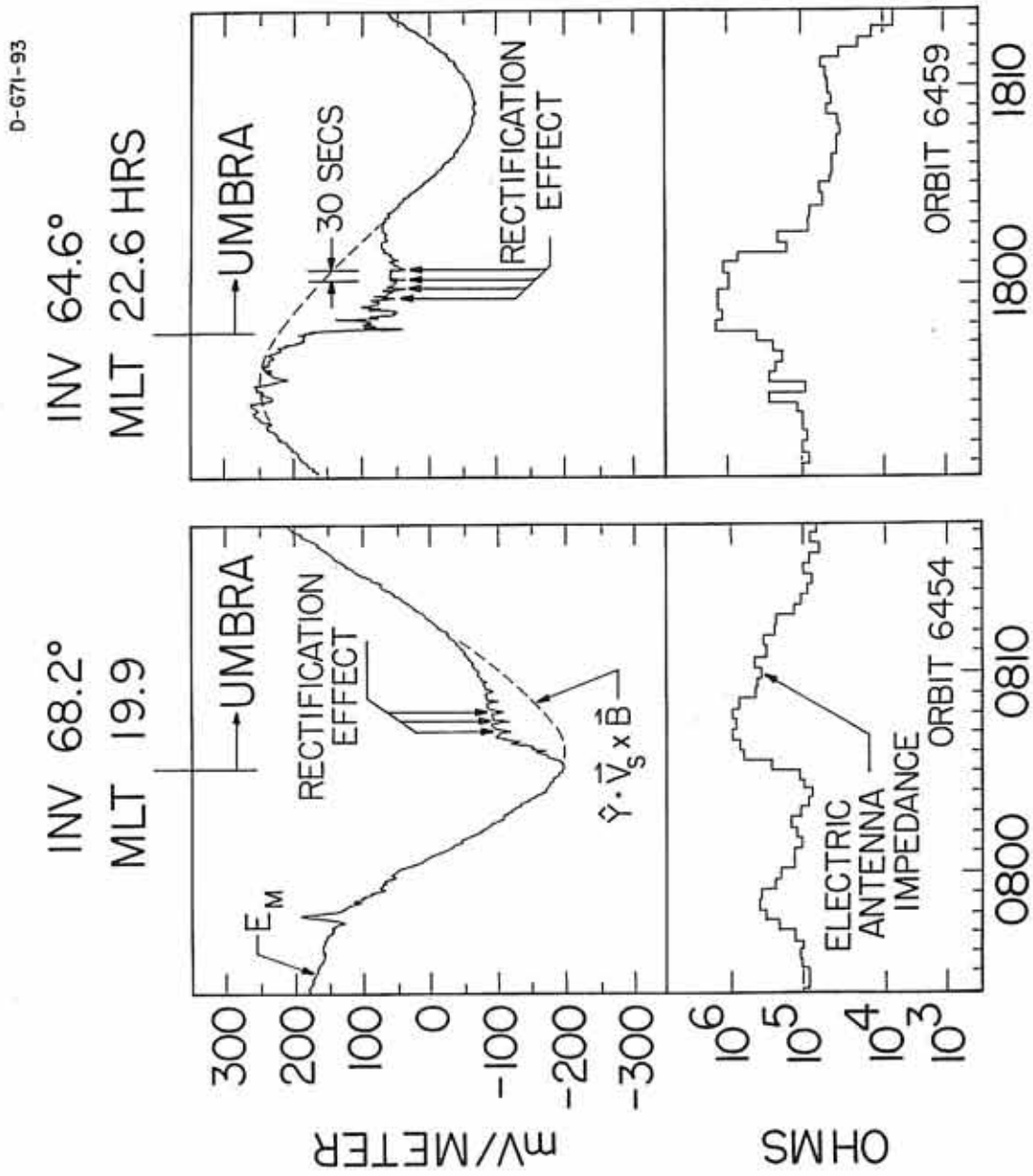


Figure 7



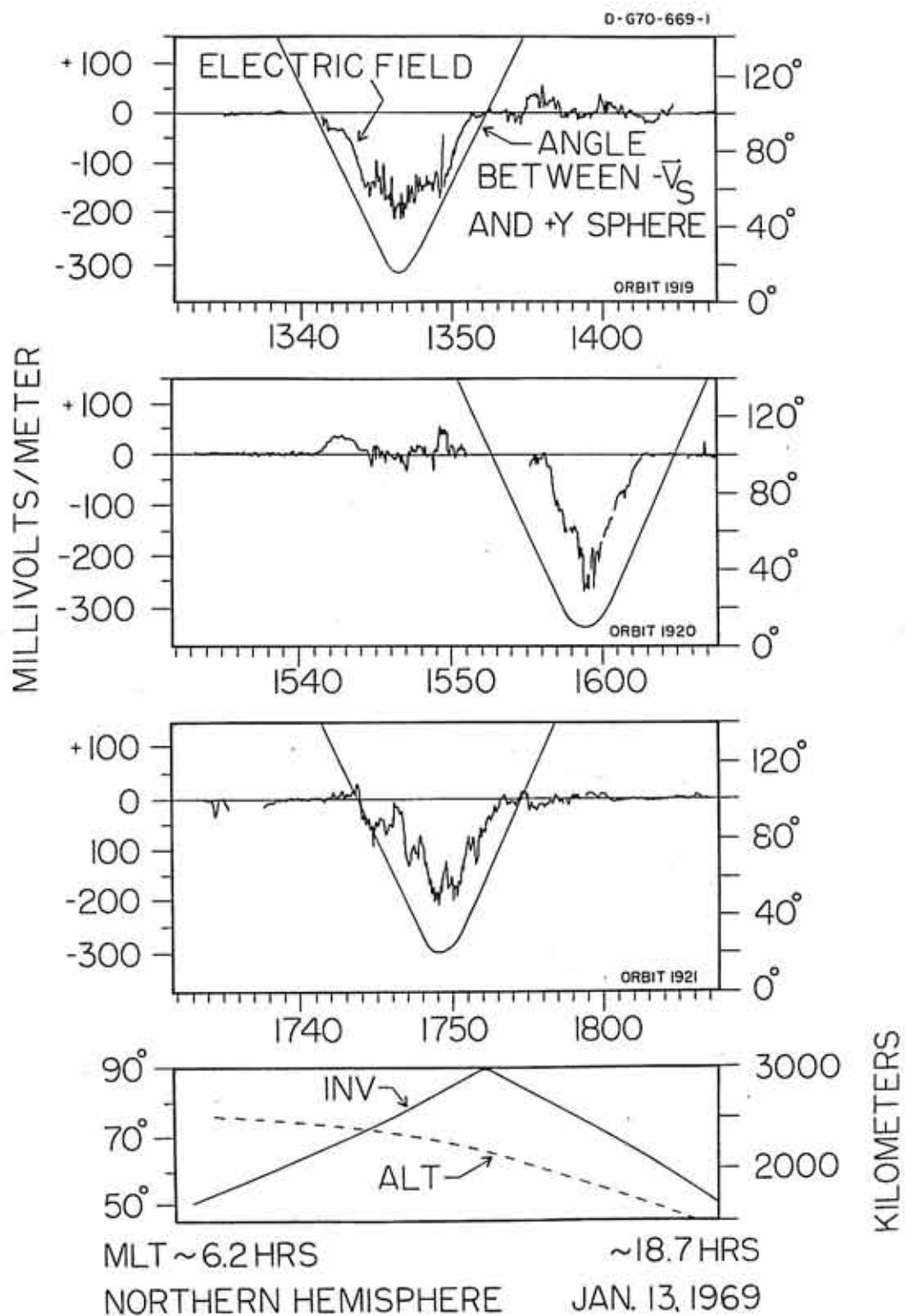


Figure 9

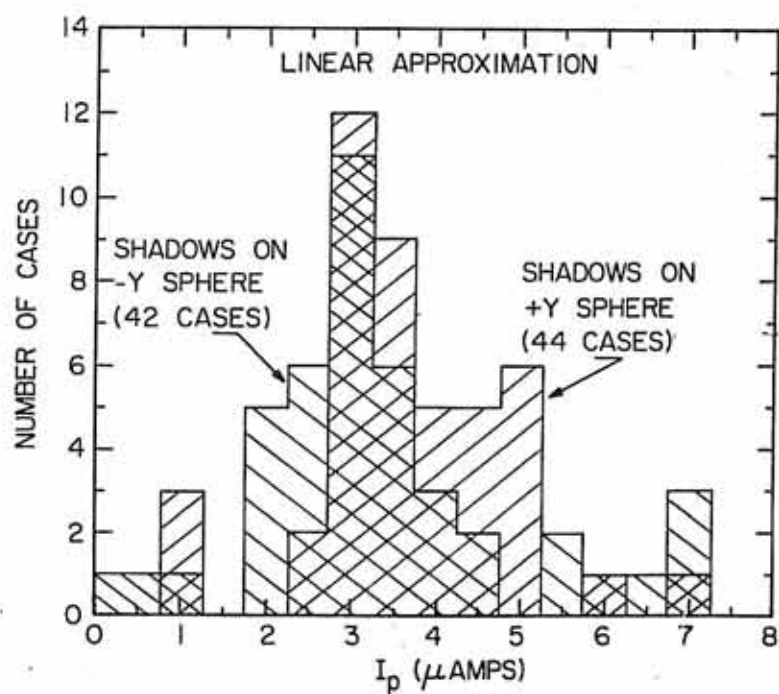
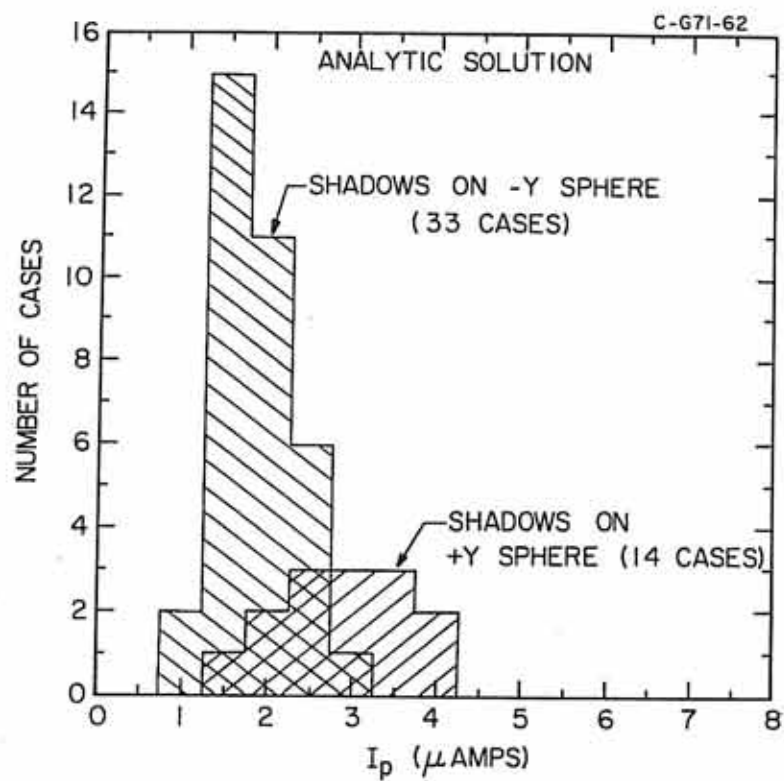


Figure 10

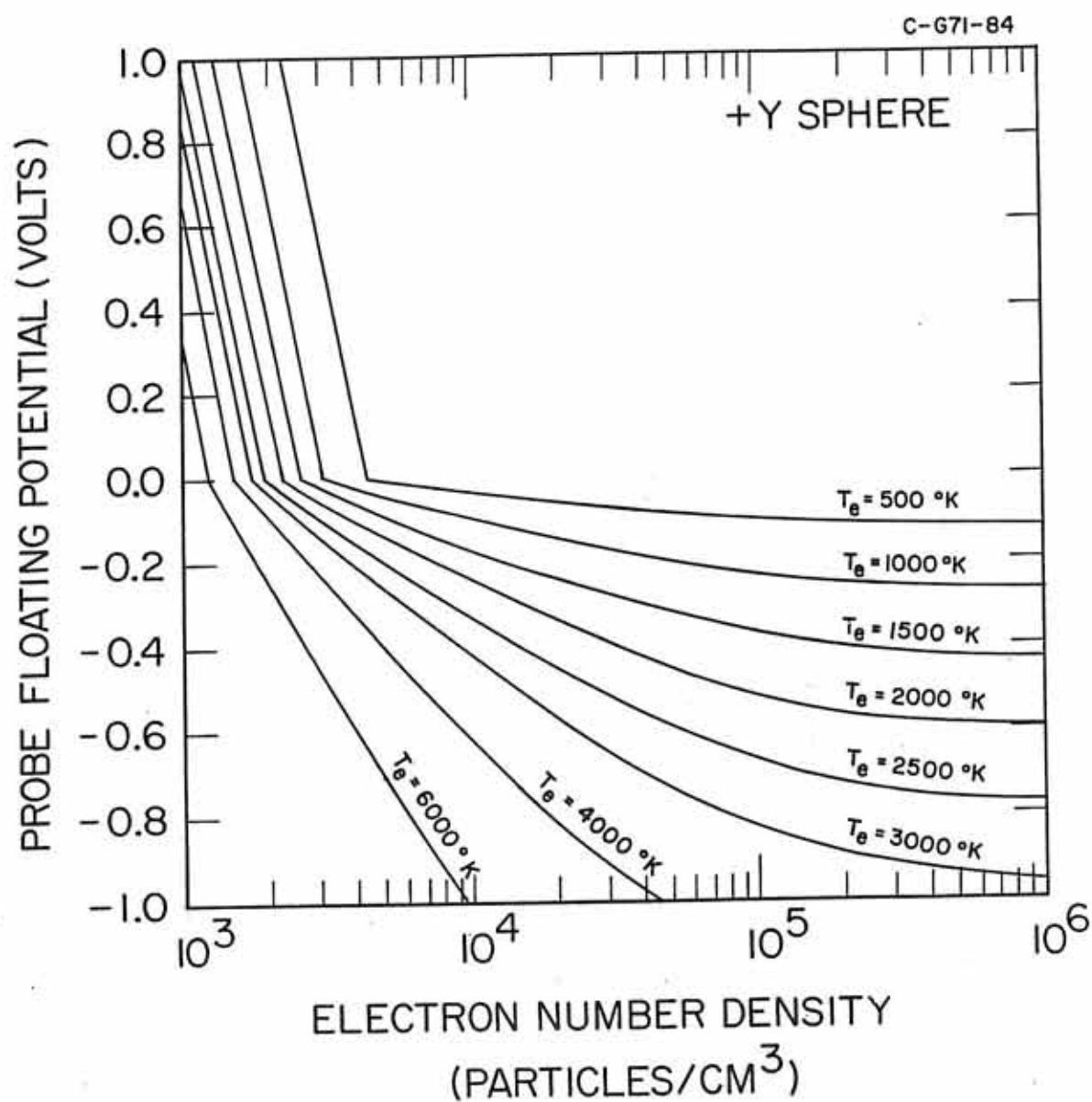


Figure 11

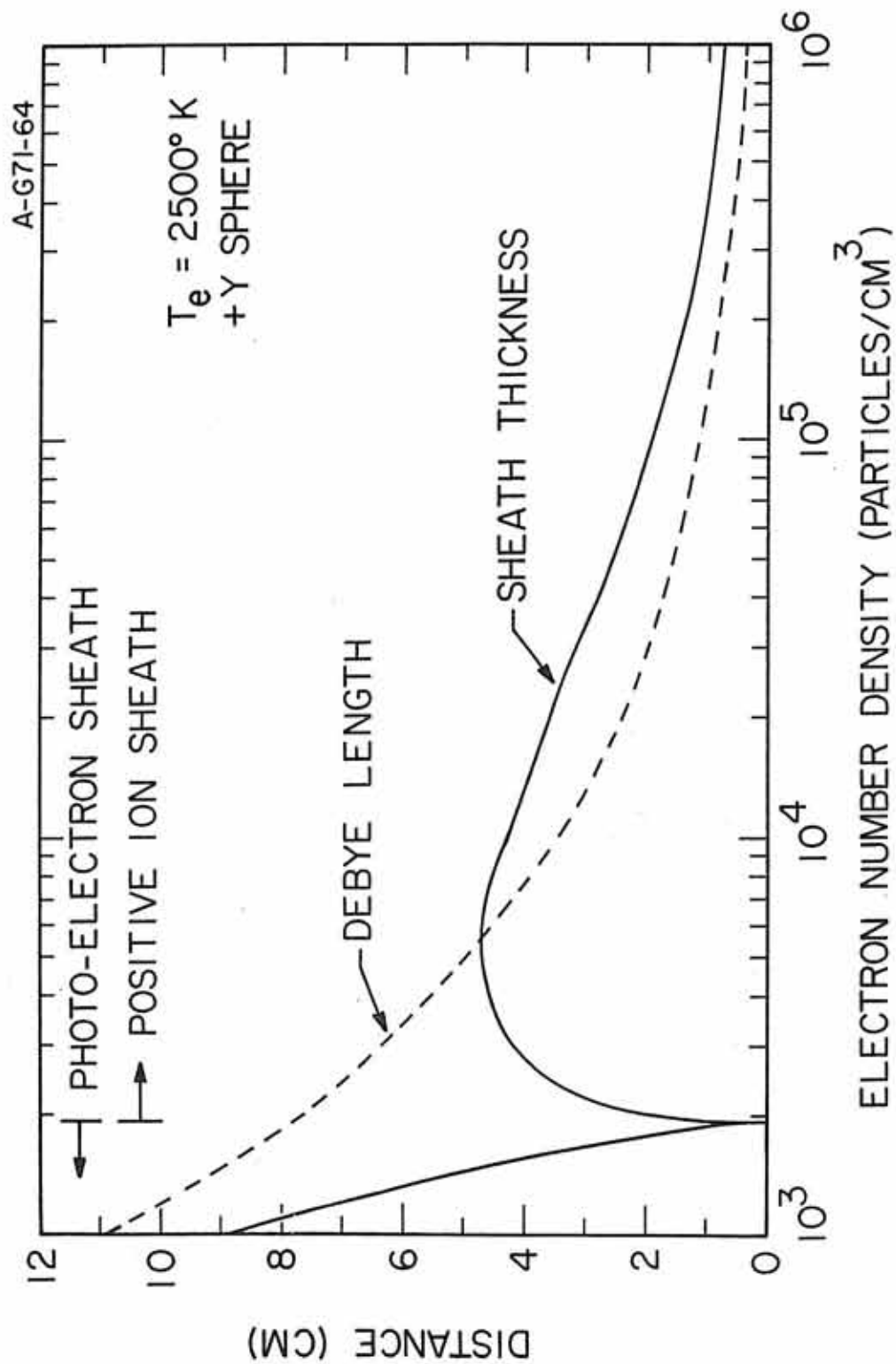


Figure 12

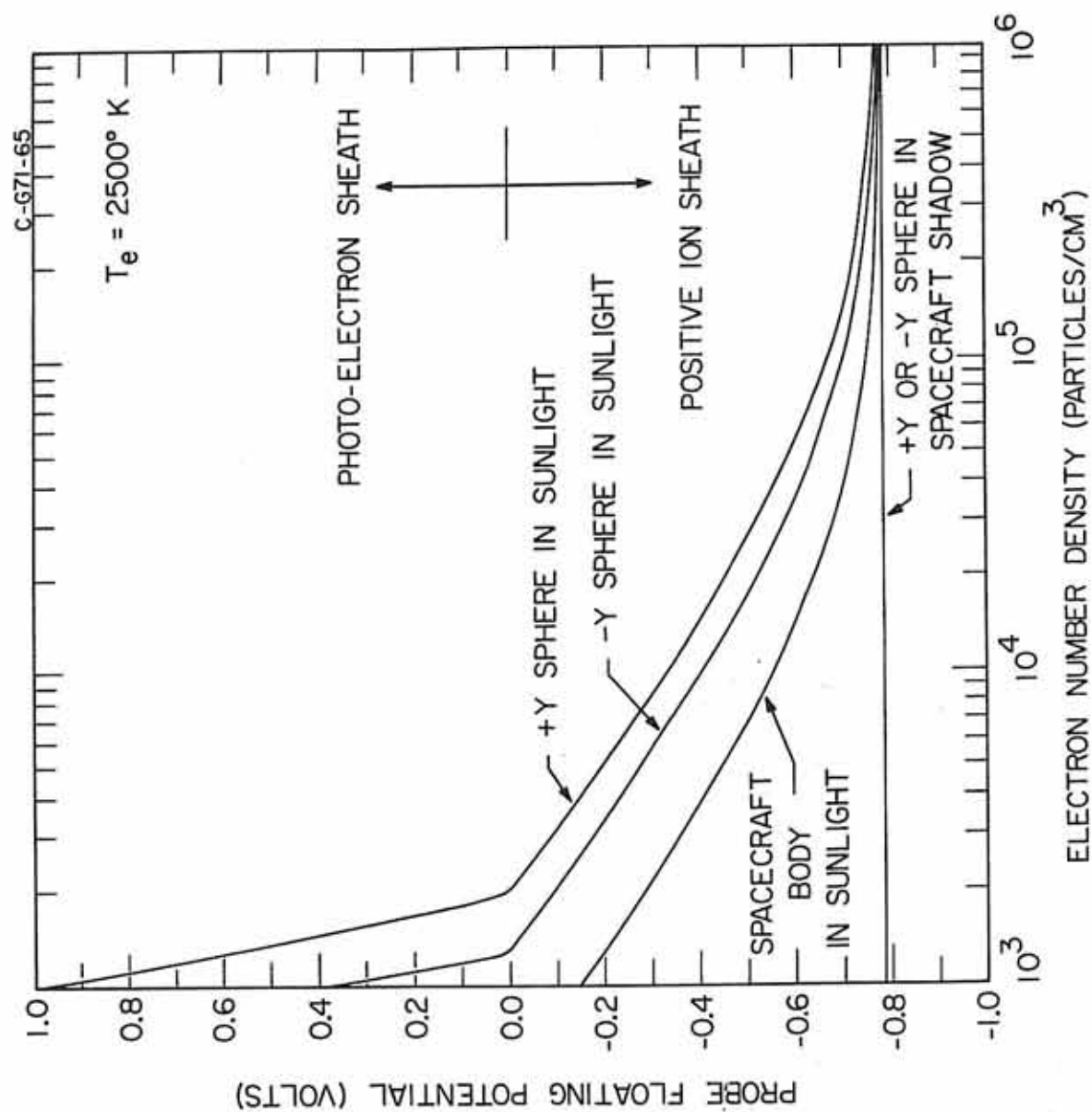


Figure 13

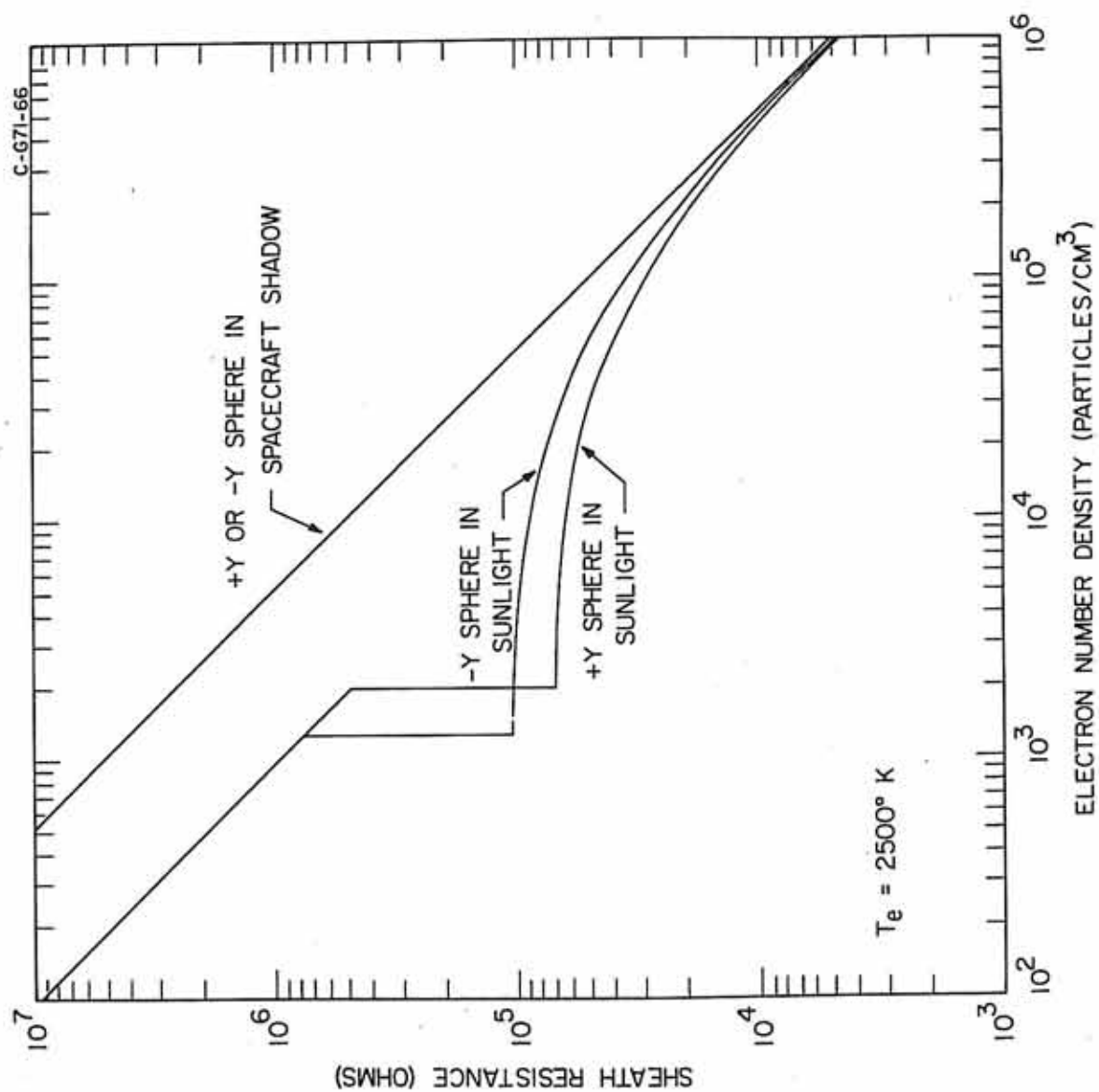


Figure 14

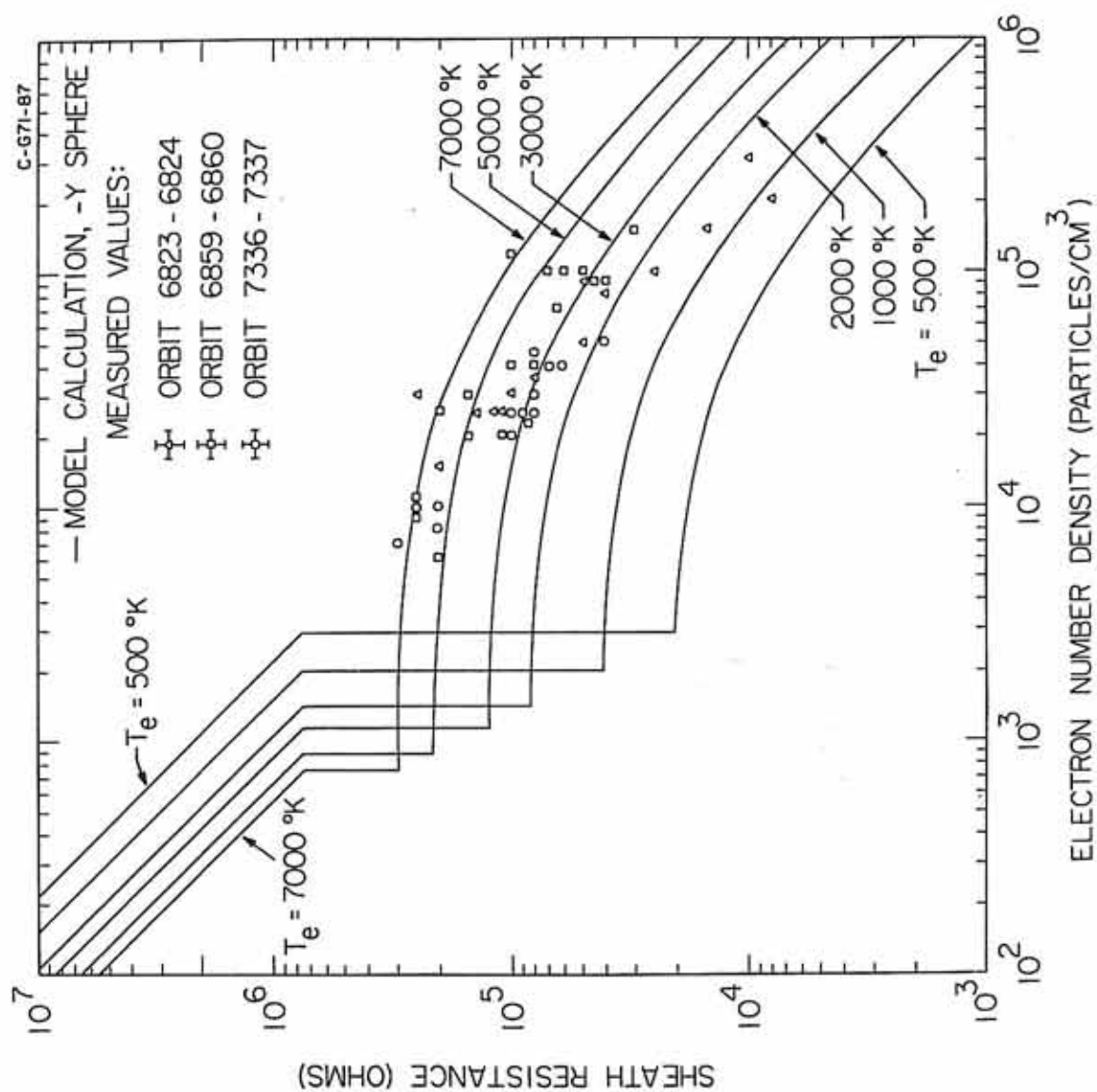


Figure 15

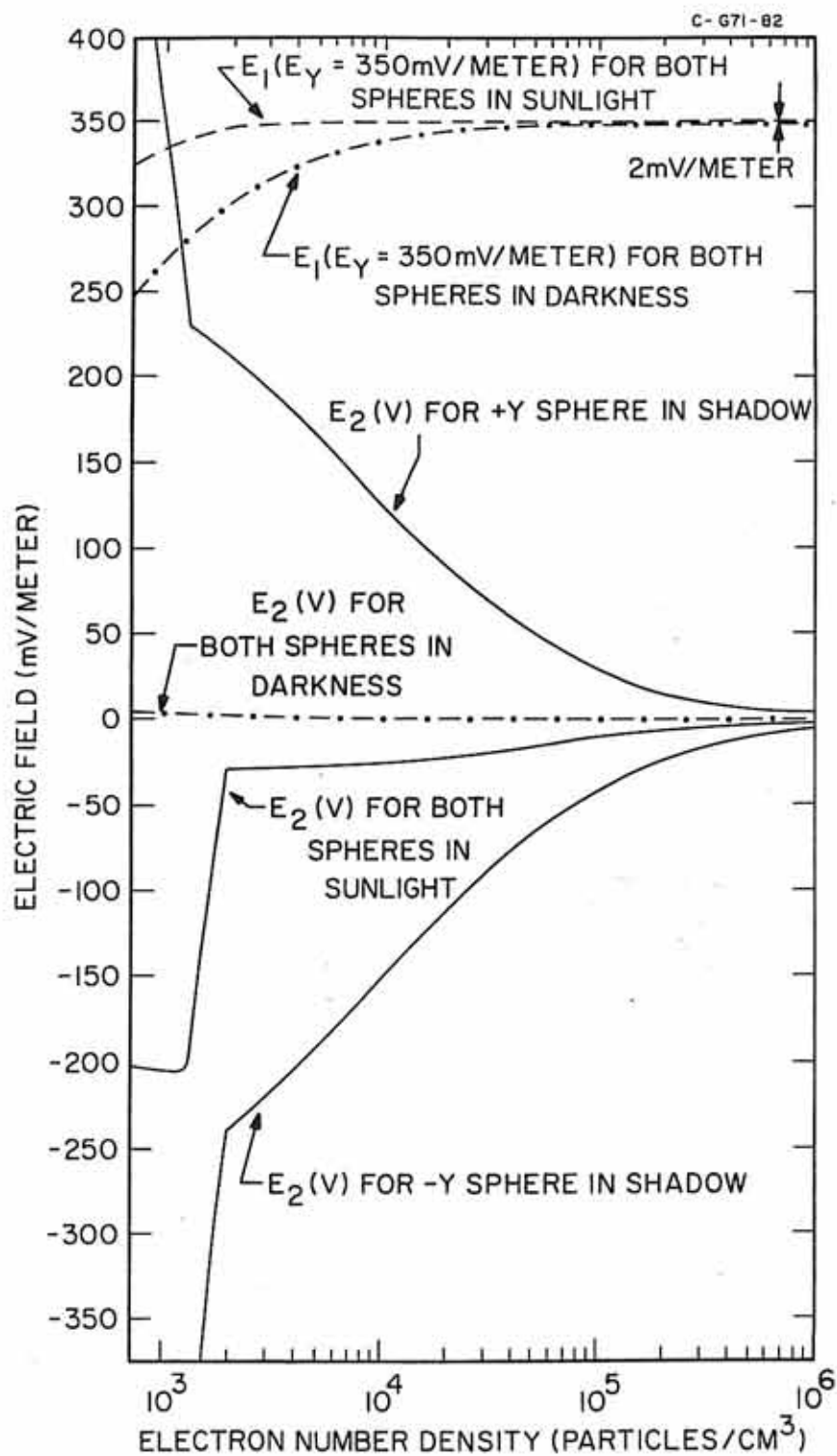


Figure 16

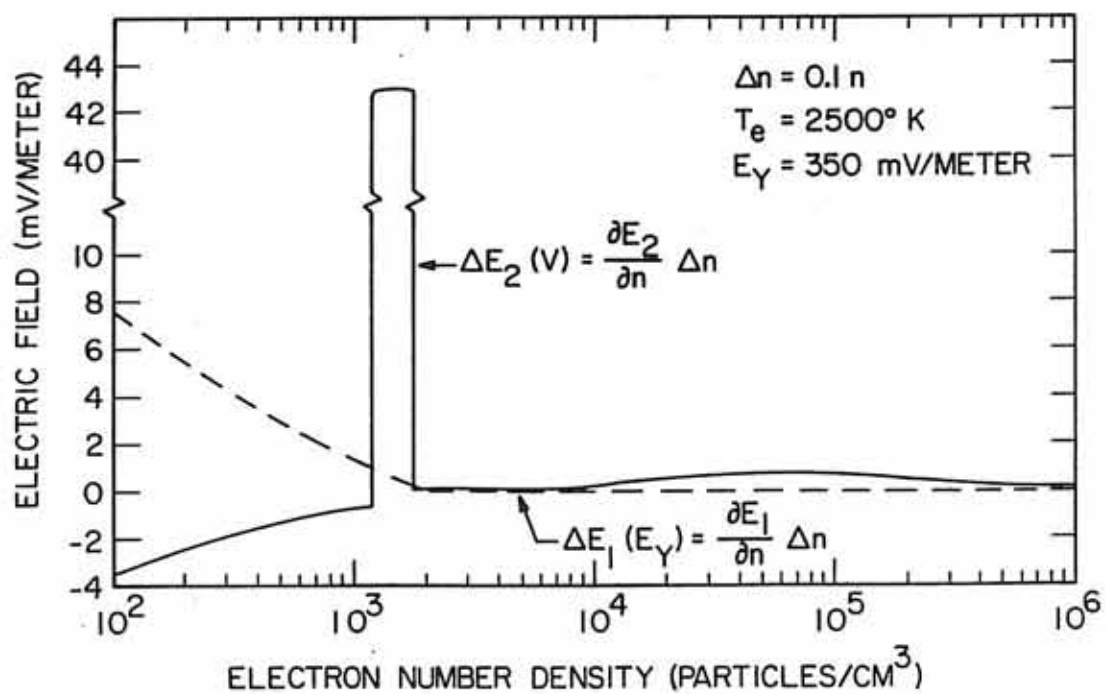
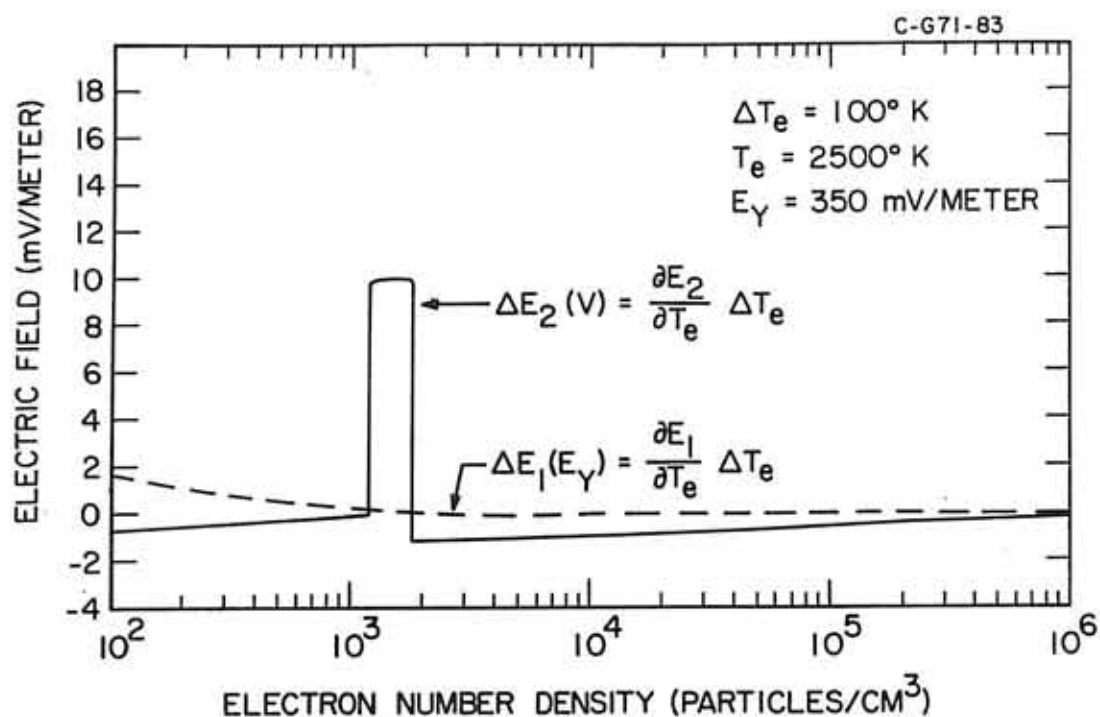


Figure 17

C-671-88

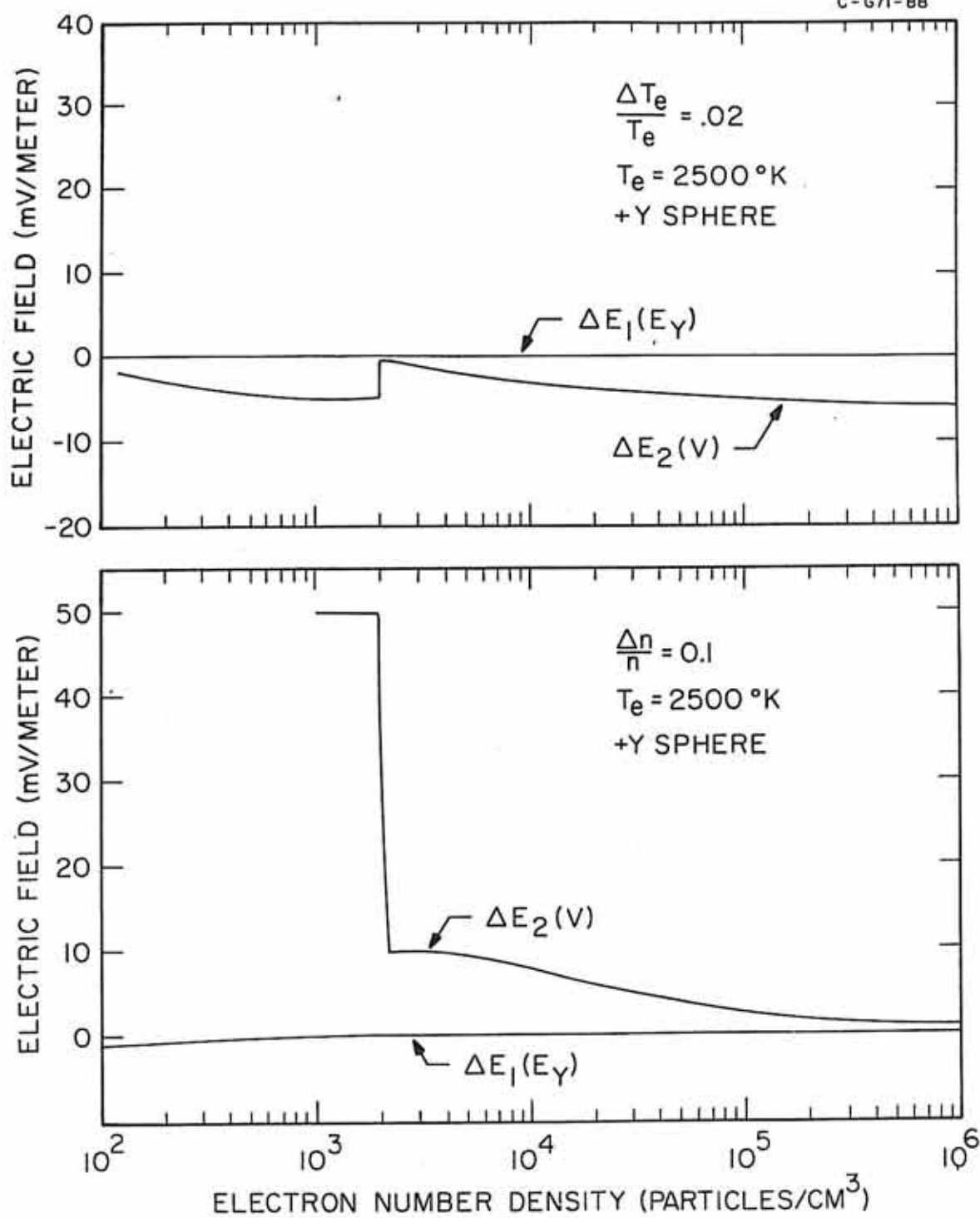
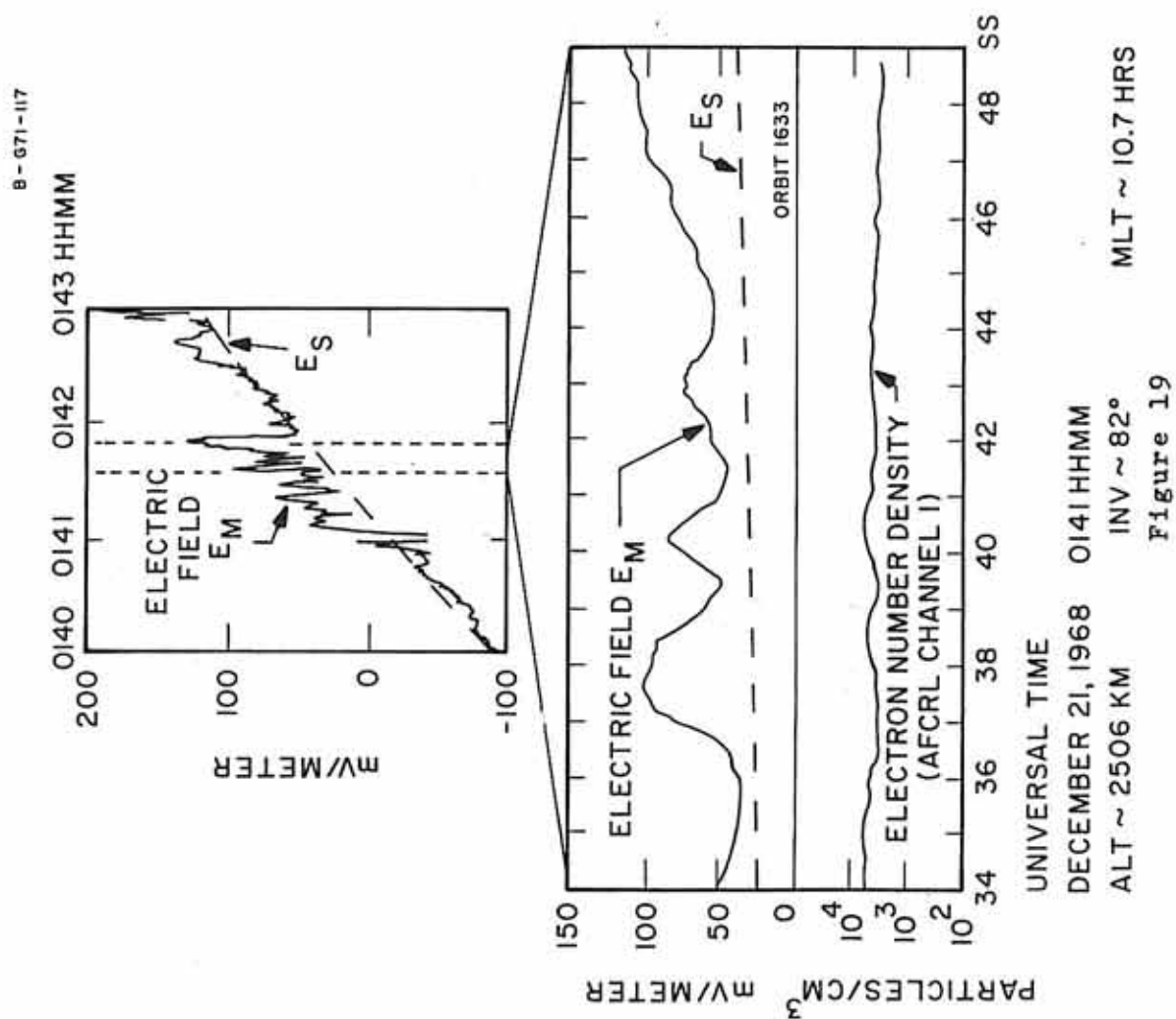
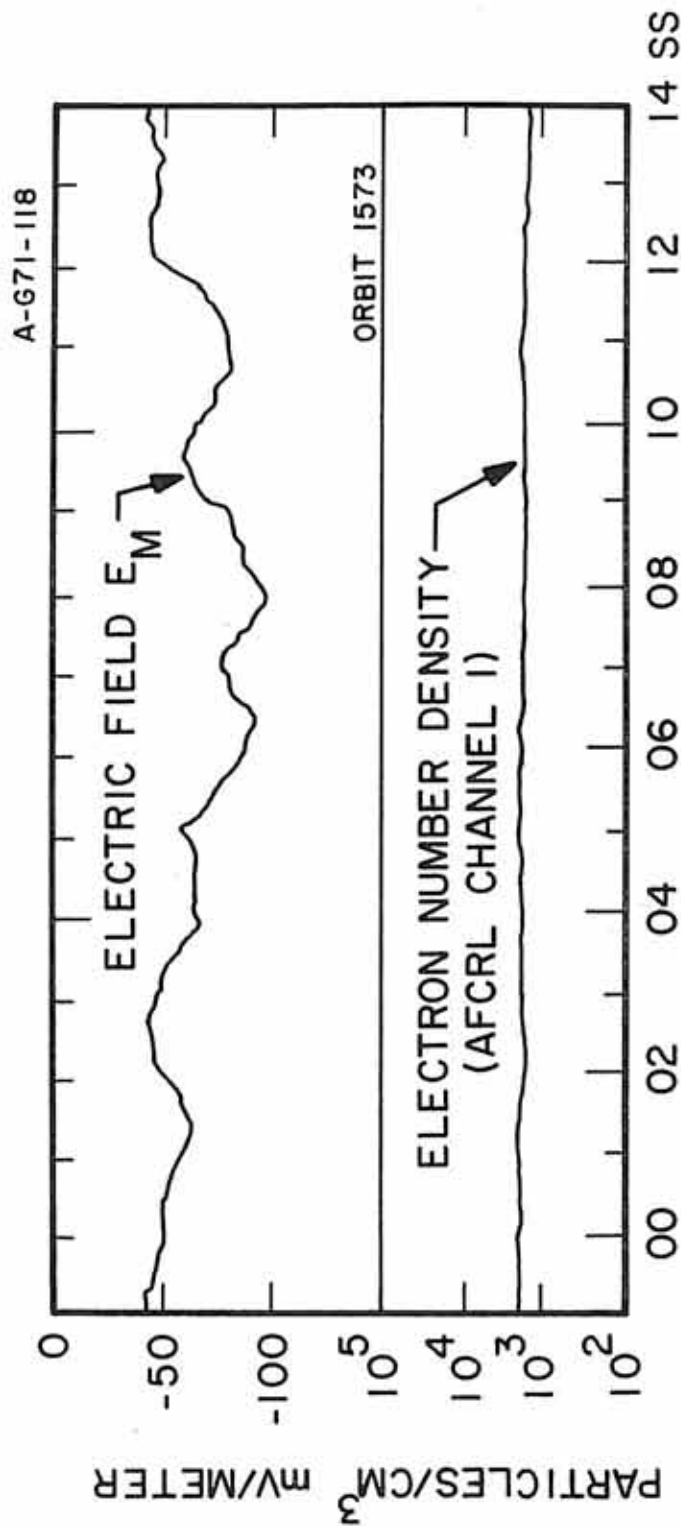


Figure 18





UNIVERSAL TIME

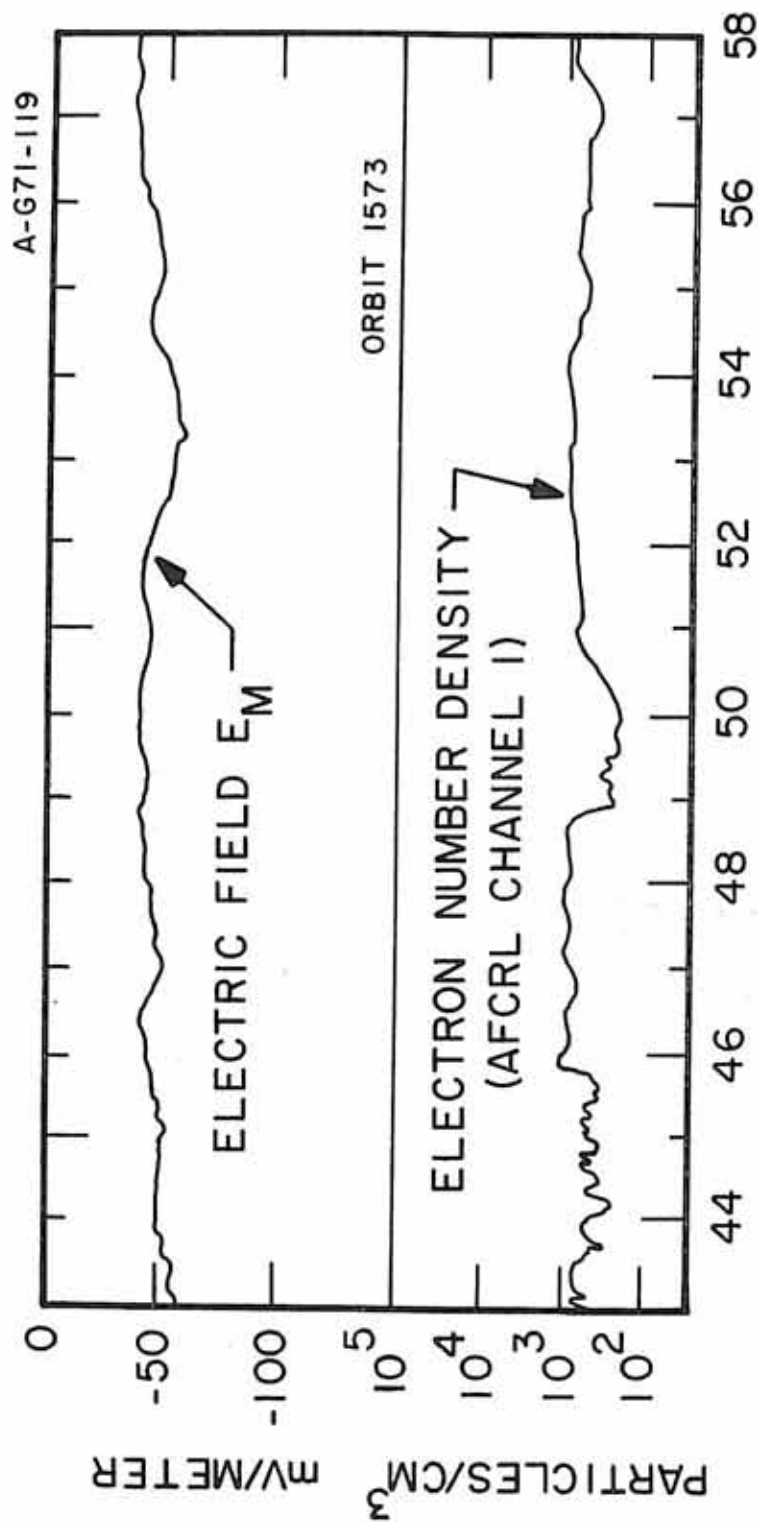
DECEMBER 16, 1968 0326 HHMM

ALT ~ 2456 KM

INV ~ 75°

MLT ~ 18.3 HRS

Figure 20



UNIVERSAL TIME

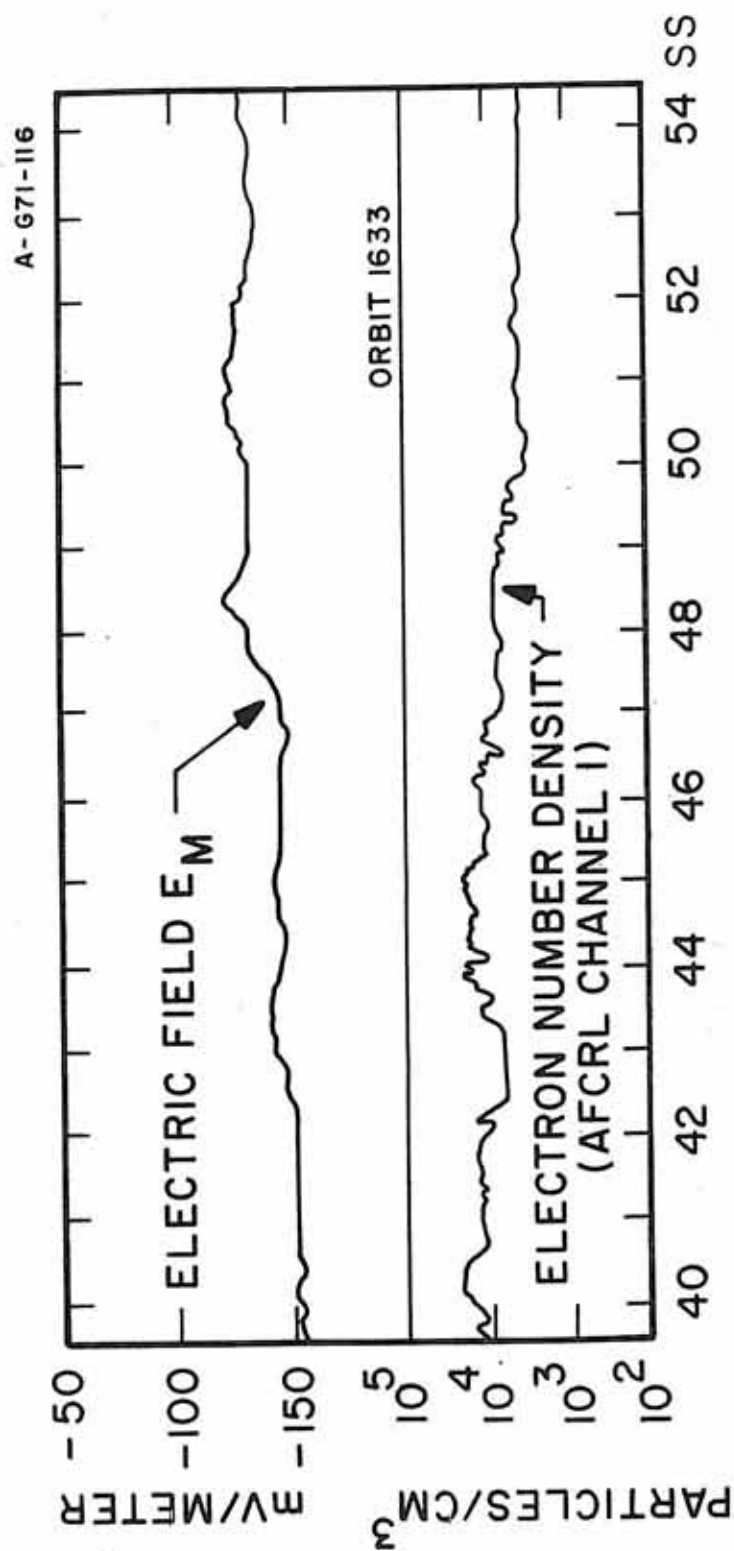
DECEMBER 16, 1968 0330 HHMM

ALT ~ 2341 KM

INV ~ 67°

MLT ~ 19.6 HRS

Figure 21



UNIVERSAL TIME

DECEMBER 21, 1968 0153 HHMM

ALT ~ 2211 KM

INV ~ 68°

MLT ~ 19.6 HRS

Figure 22

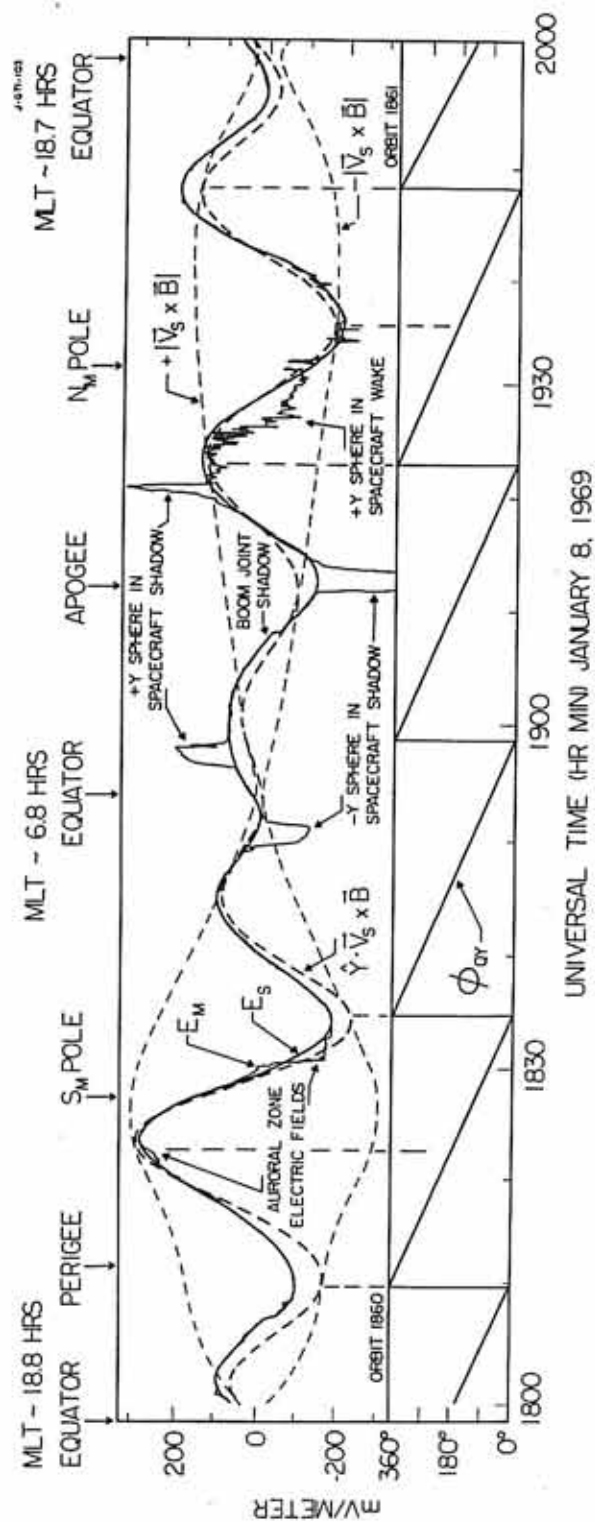


Figure 23

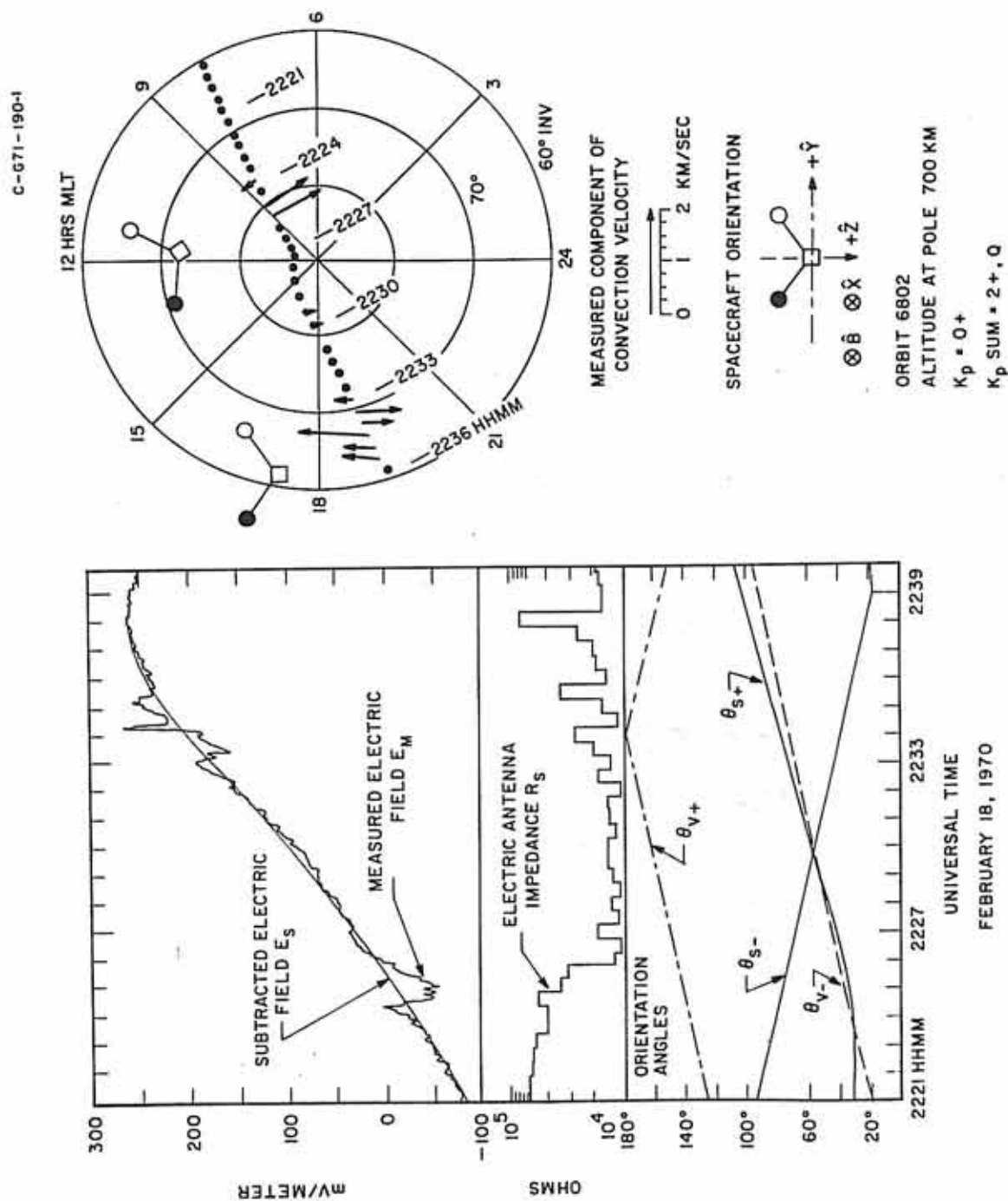
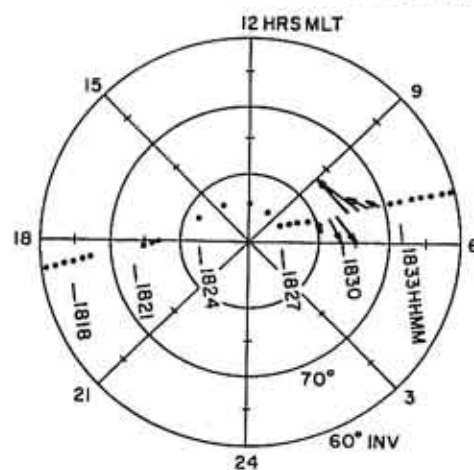


Figure 24

D-G70-673-1

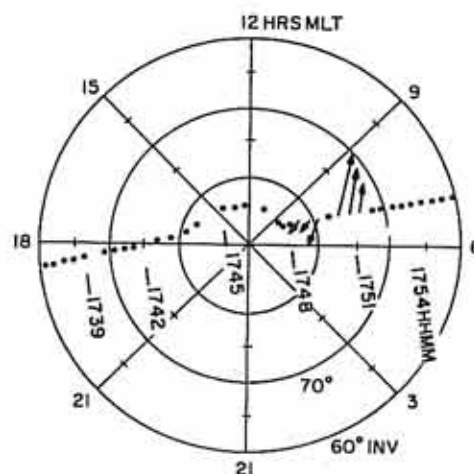
ORBIT 1860
 $K_p = 2+$
 $K_p \text{ SUM} = 16-$

SOUTHERN HEMISPHERE
 JANUARY 8, 1969
 ALTITUDE ~ 1200KM



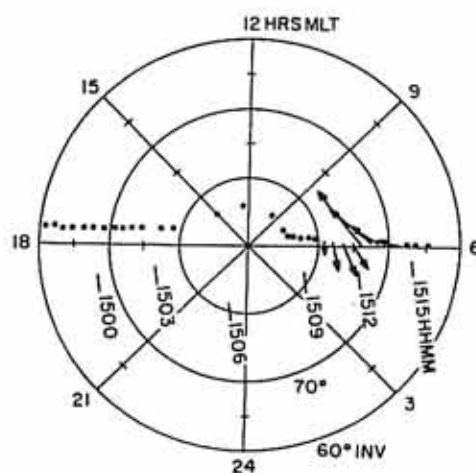
ORBIT 1884
 $K_p = 1-$
 $K_p \text{ SUM} = 6-$

SOUTHERN HEMISPHERE
 JANUARY 10, 1969
 ALTITUDE ~ 1200KM



ORBIT 1980
 $K_p = 3-$
 $K_p \text{ SUM} = 27, D$

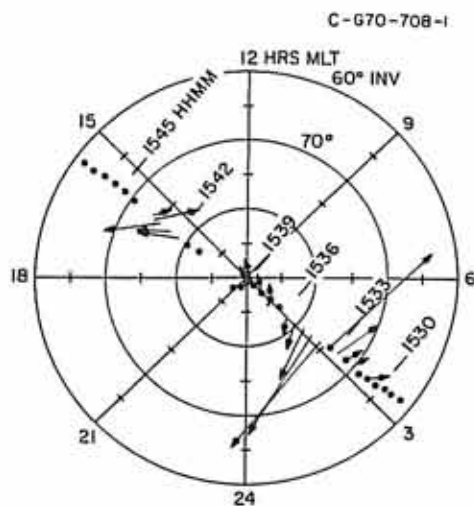
SOUTHERN HEMISPHERE
 JANUARY 18, 1969
 ALTITUDE ~ 1300KM



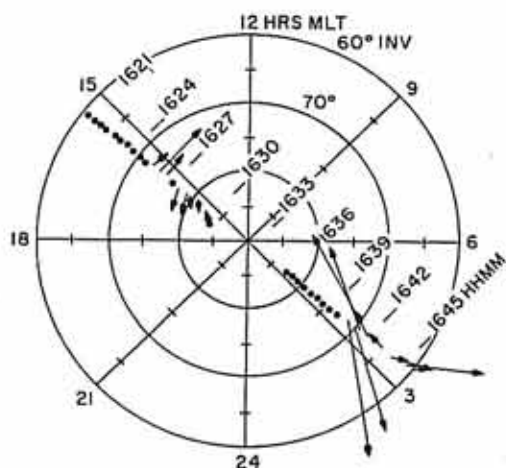
CONVECTION VELOCITY COMPONENT
 1 KM/S

Figure 25

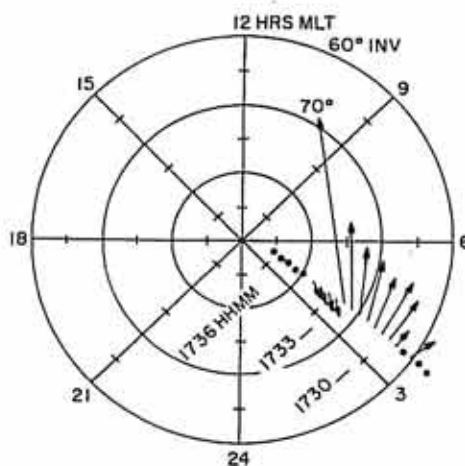
NORTHERN HEMISPHERE
ORBIT 2224
 $K_p = 1+$



SOUTHERN HEMISPHERE
ORBIT 2224
 $K_p = 1+$



NORTHERN HEMISPHERE
ORBIT 2225
 $K_p = 1+$
 $K_p \text{ SUM} = 16, M$



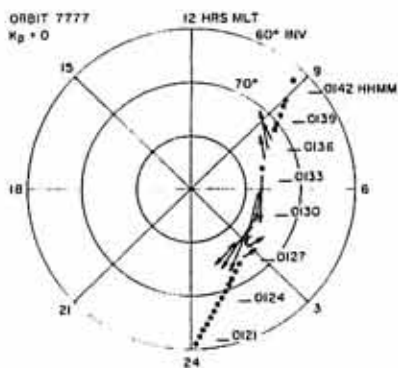
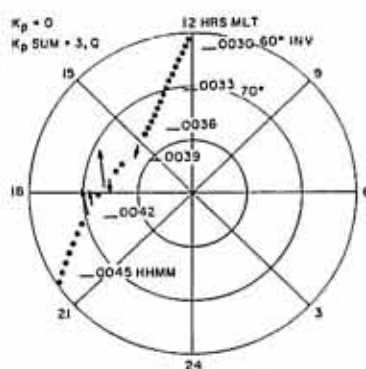
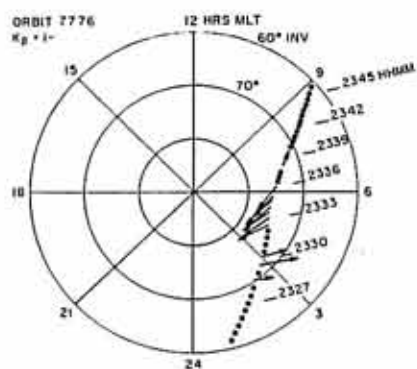
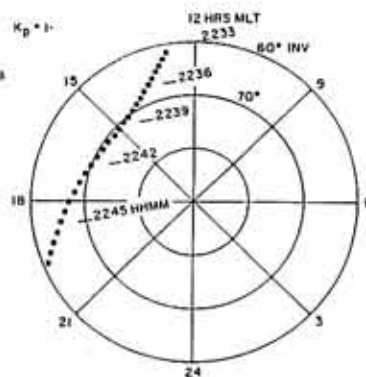
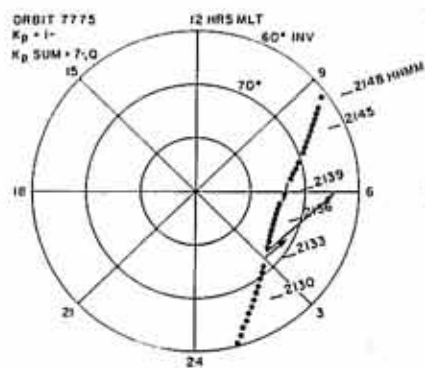
FEBRUARY 7, 1969
CONVECTION VELOCITY
COMPONENT
1KM/S

Figure 26

D-071-188

NORTHERN HEMISPHERE

SOUTHERN HEMISPHERE



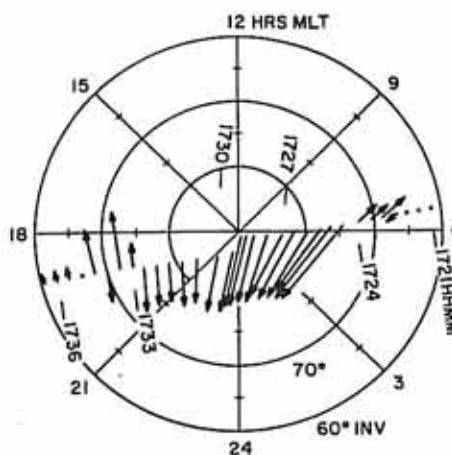
MAY 9 - 10, 1970
CONVECTION VELOCITY COMPONENT

0 1 2 KM/SEC

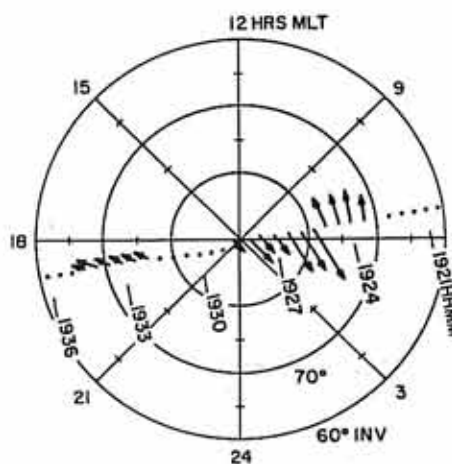
Figure 27

D-970-665-1

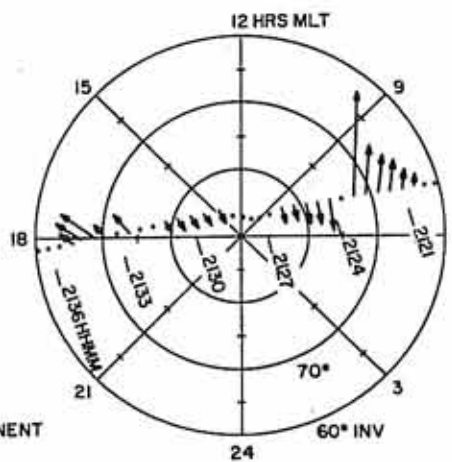
ORBIT 6909
 $K_p = 3$



ORBIT 6910
 $K_p = 3$



ORBIT 6911
 $K_p = 3+$
 $K_p \text{ SUM} = 14-$



NORTHERN HEMISPHERE
 FEBRUARY 27, 1970
 ALTITUDE ~ 700KM

CONVECTION VELOCITY COMPONENT

1 KM/S

Figure 28

C-671-177

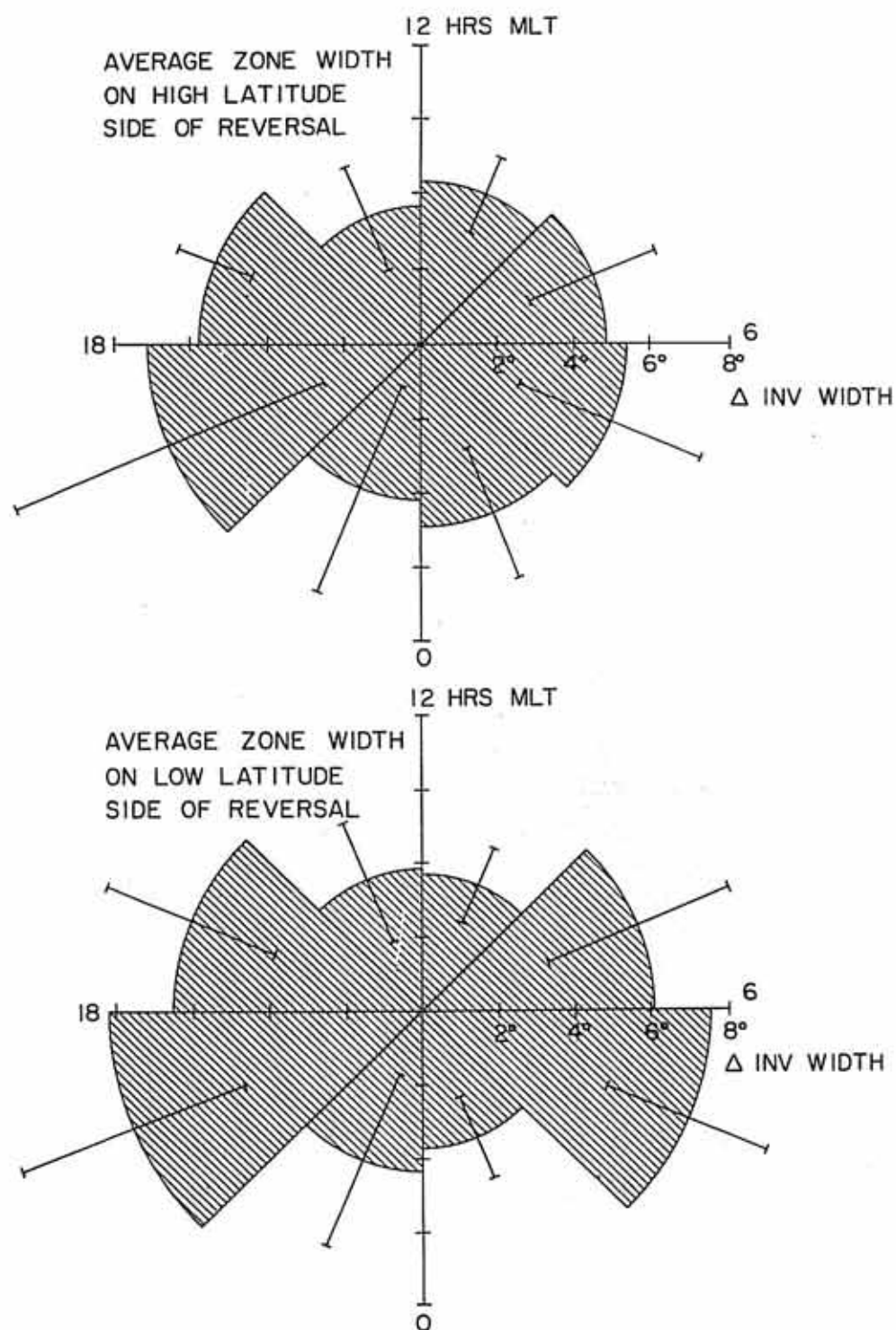


Figure 29

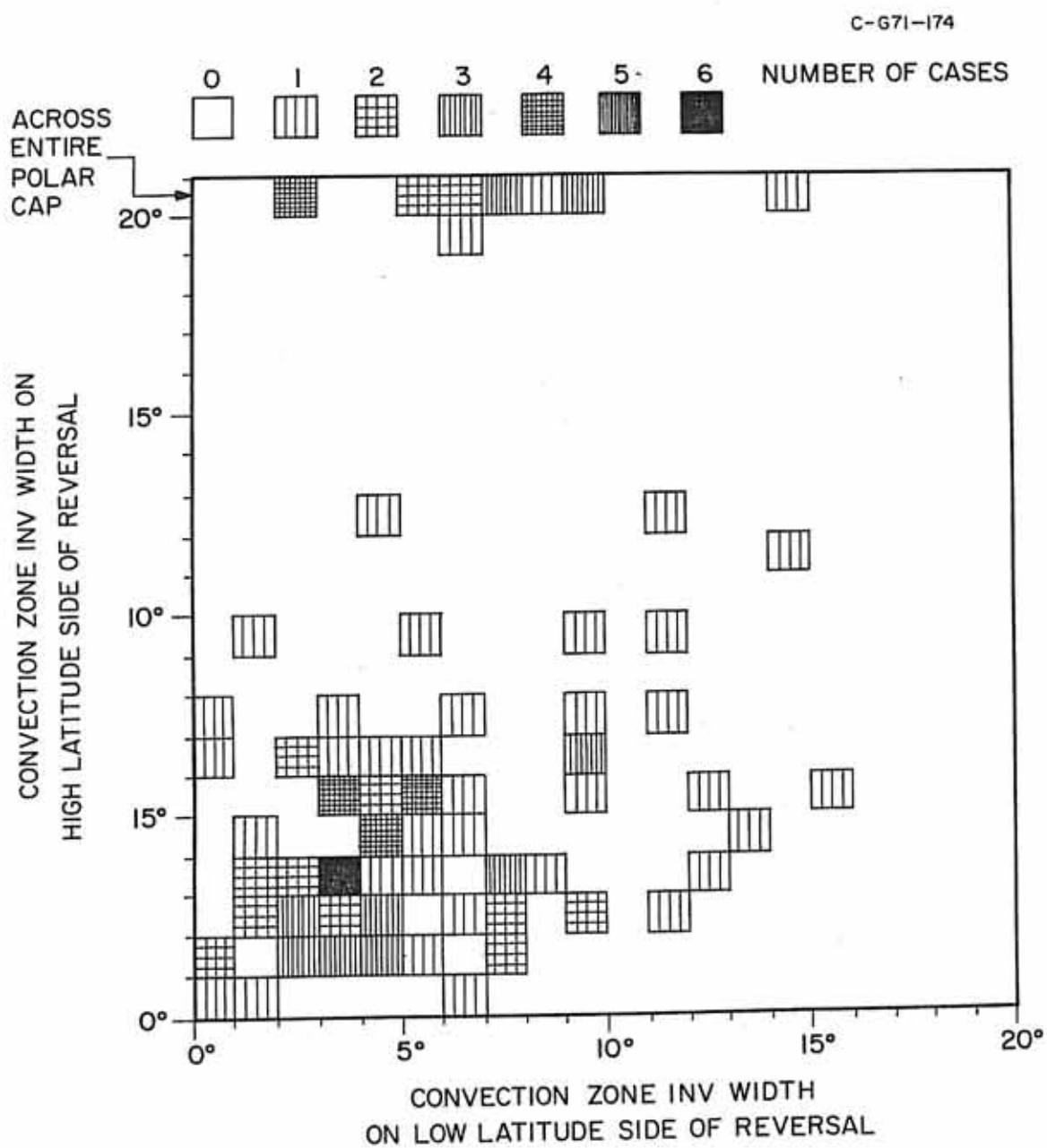
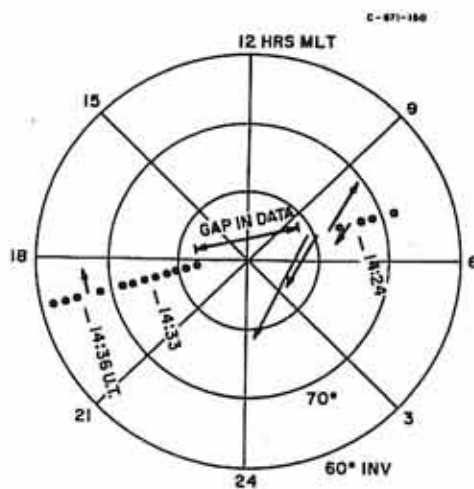
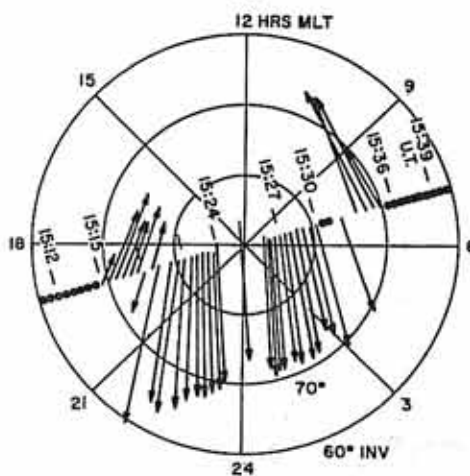


Figure 30

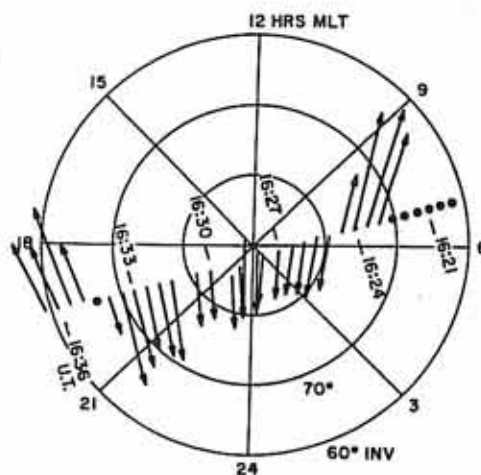
NORTHERN HEMISPHERE
ORBIT 6871
 $K_p = 3-$



SOUTHERN HEMISPHERE
ORBIT 6871
 $K_p = 4+$



NORTHERN HEMISPHERE
ORBIT 6872
 $K_p = 4+$



FEBRUARY 24, 1970
 $K_p \text{ SUM} = 17+, 0$

CONVECTION VELOCITY
COMPONENT

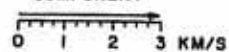
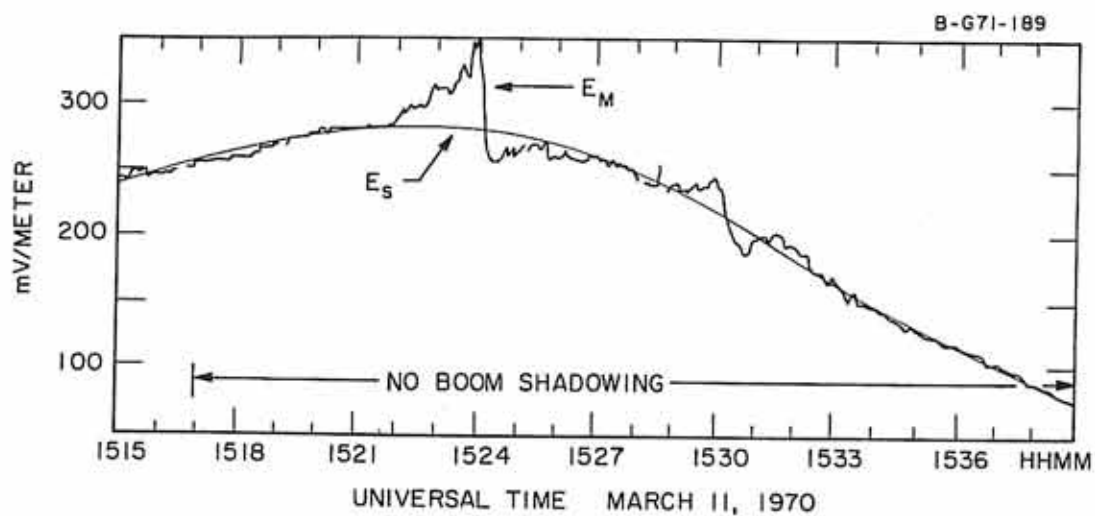


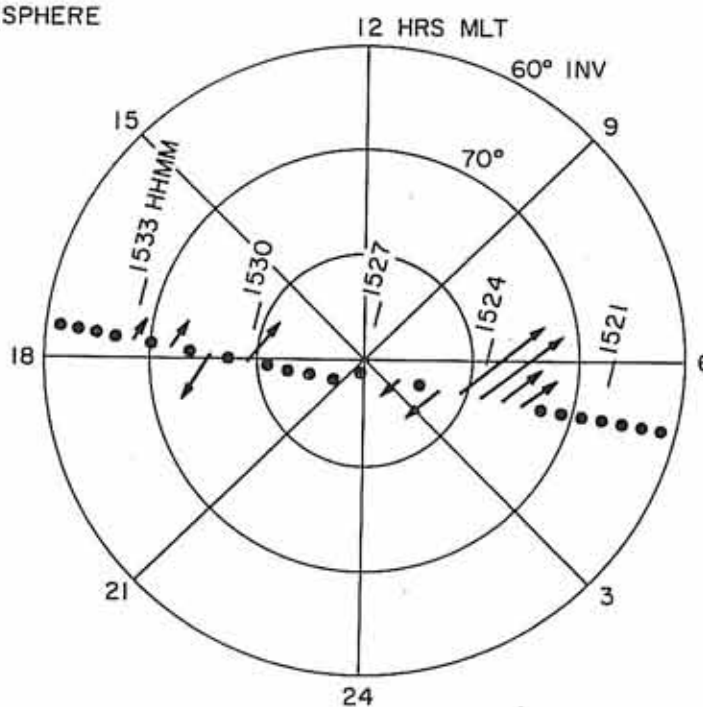
Figure 31



NORTHERN HEMISPHERE
ORBIT 7054

$K_p = 1-$

$K_p \text{ SUM} = 5+, M$



CONVECTION VELOCITY COMPONENT

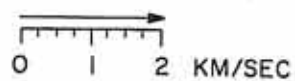
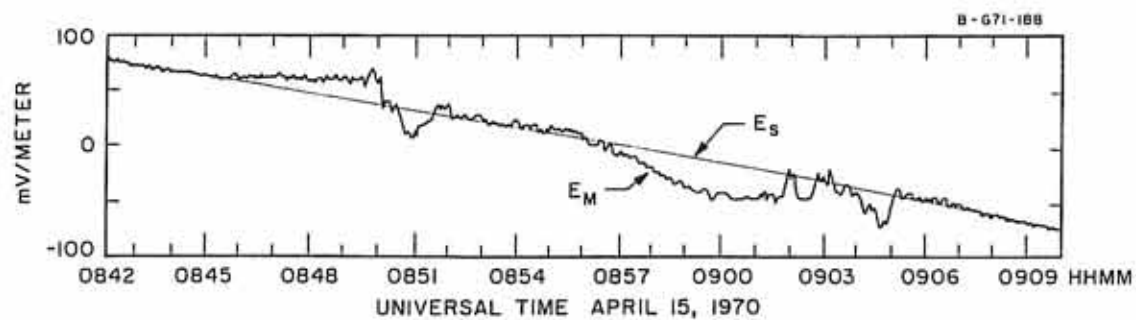


Figure 32



SOUTHERN HEMISPHERE
 ORBIT 7476
 $K_p = 1$
 $K_p \text{ SUM} = 11-, Q$

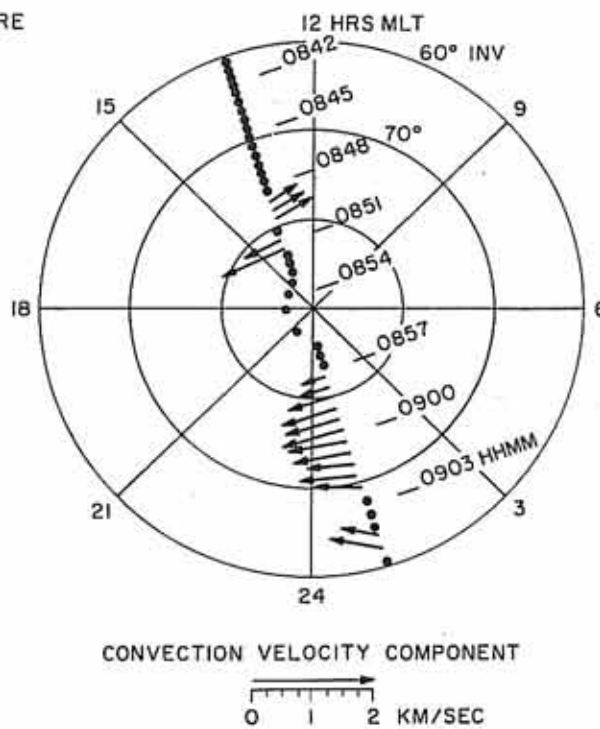
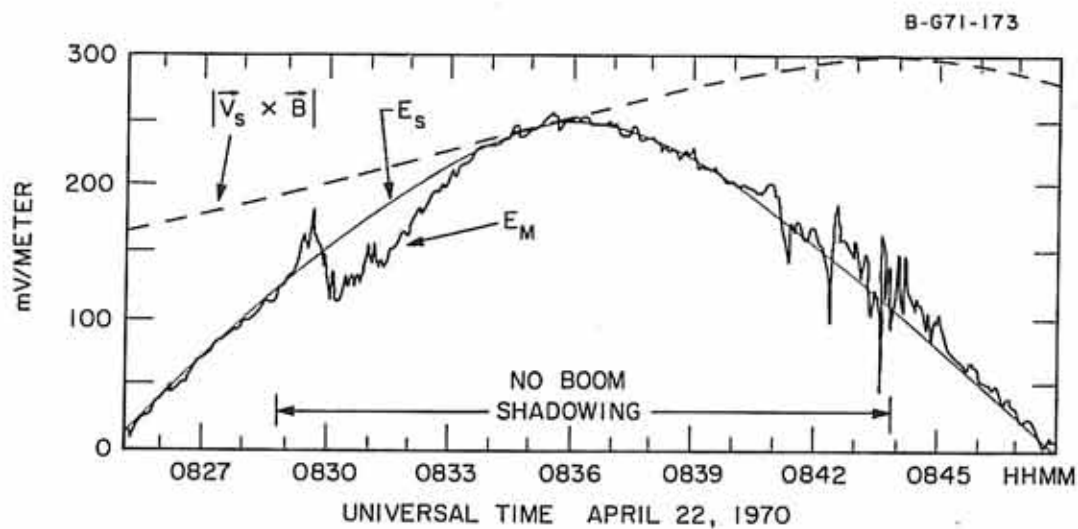


Figure 33



NORTHERN HEMISPHERE

ORBIT 7561

$K_p = 5$

$K_p \text{ SUM} = 28, D$

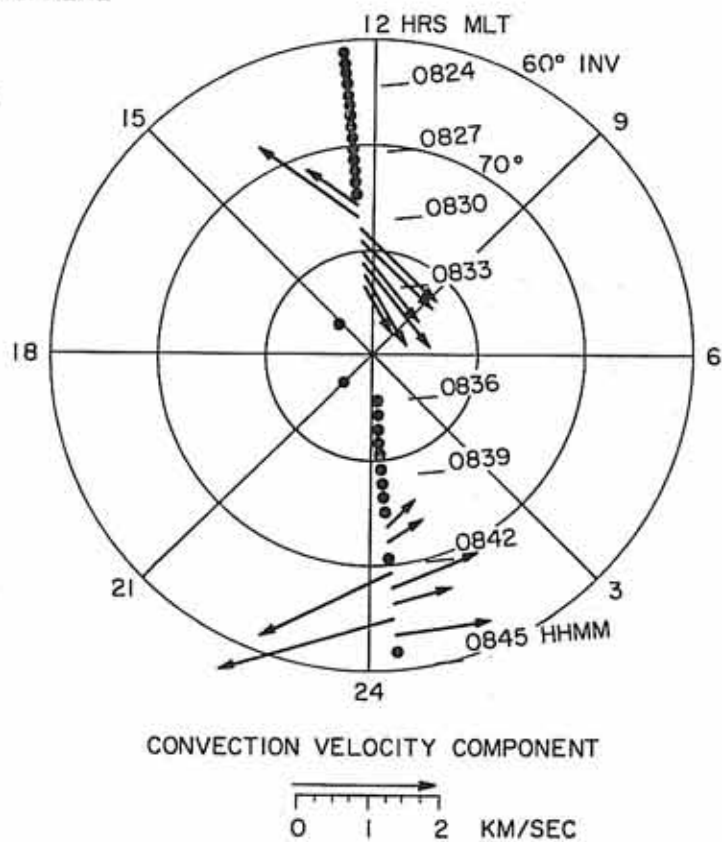


Figure 34

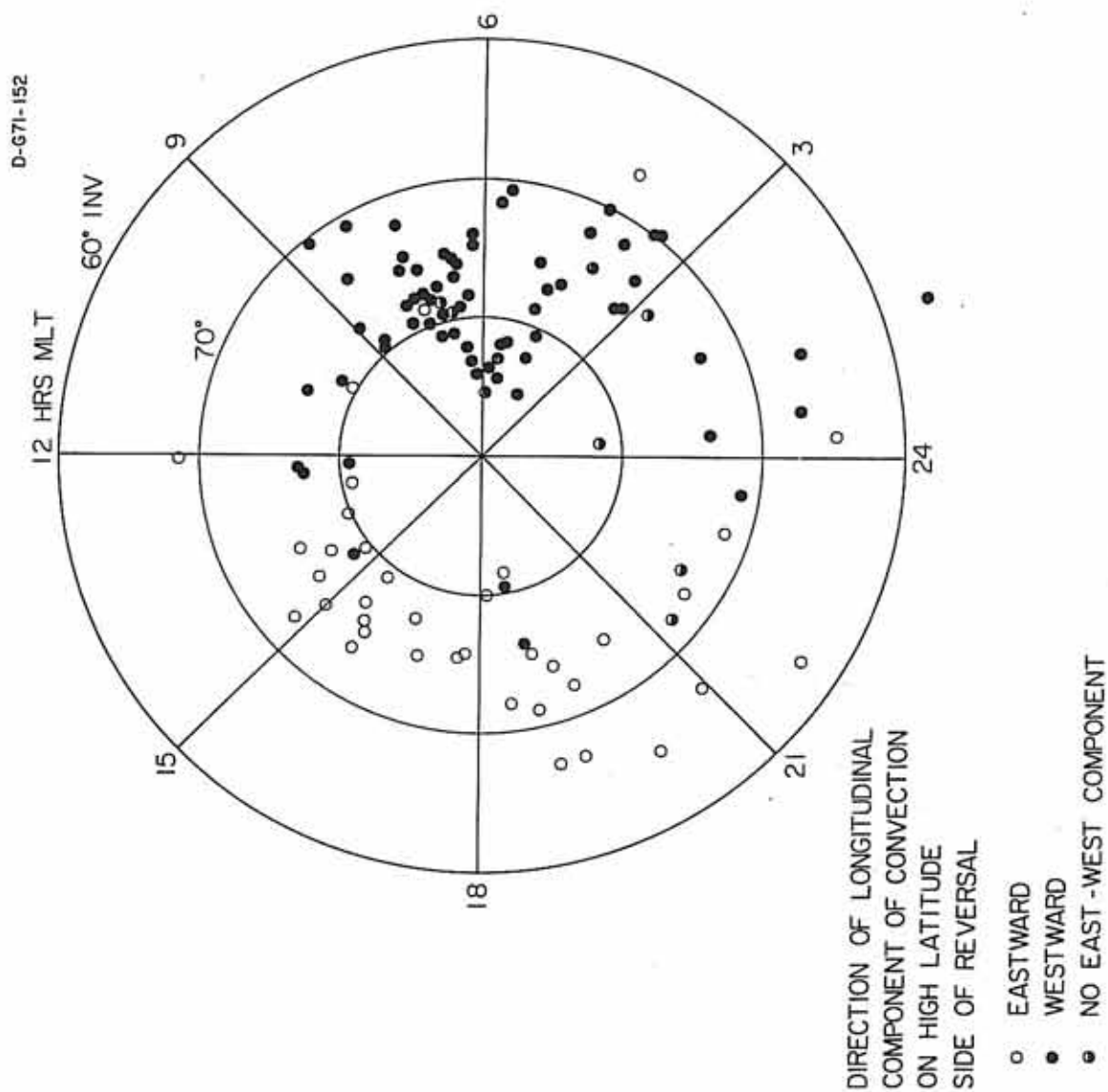


Figure 35

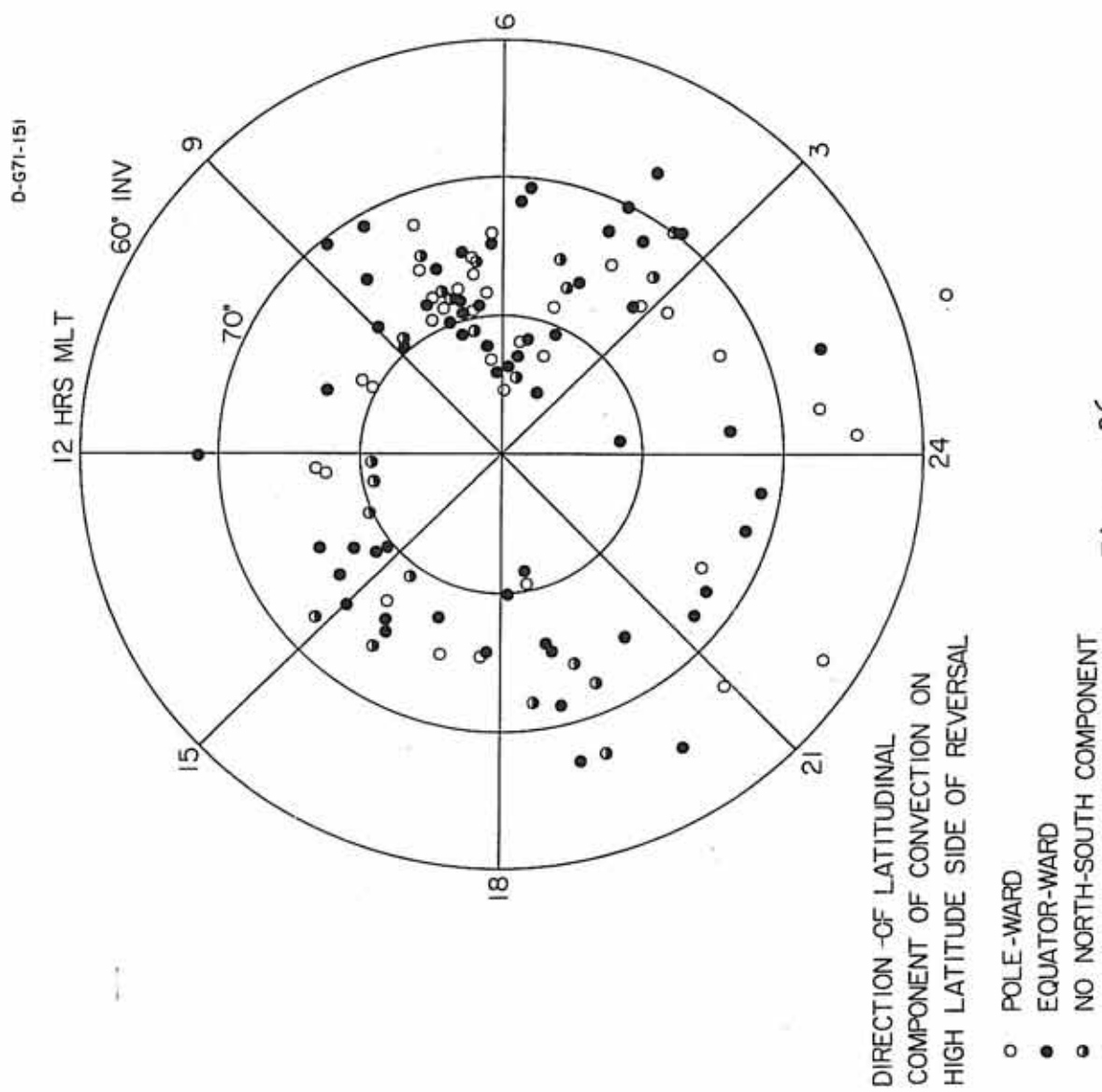


Figure 36

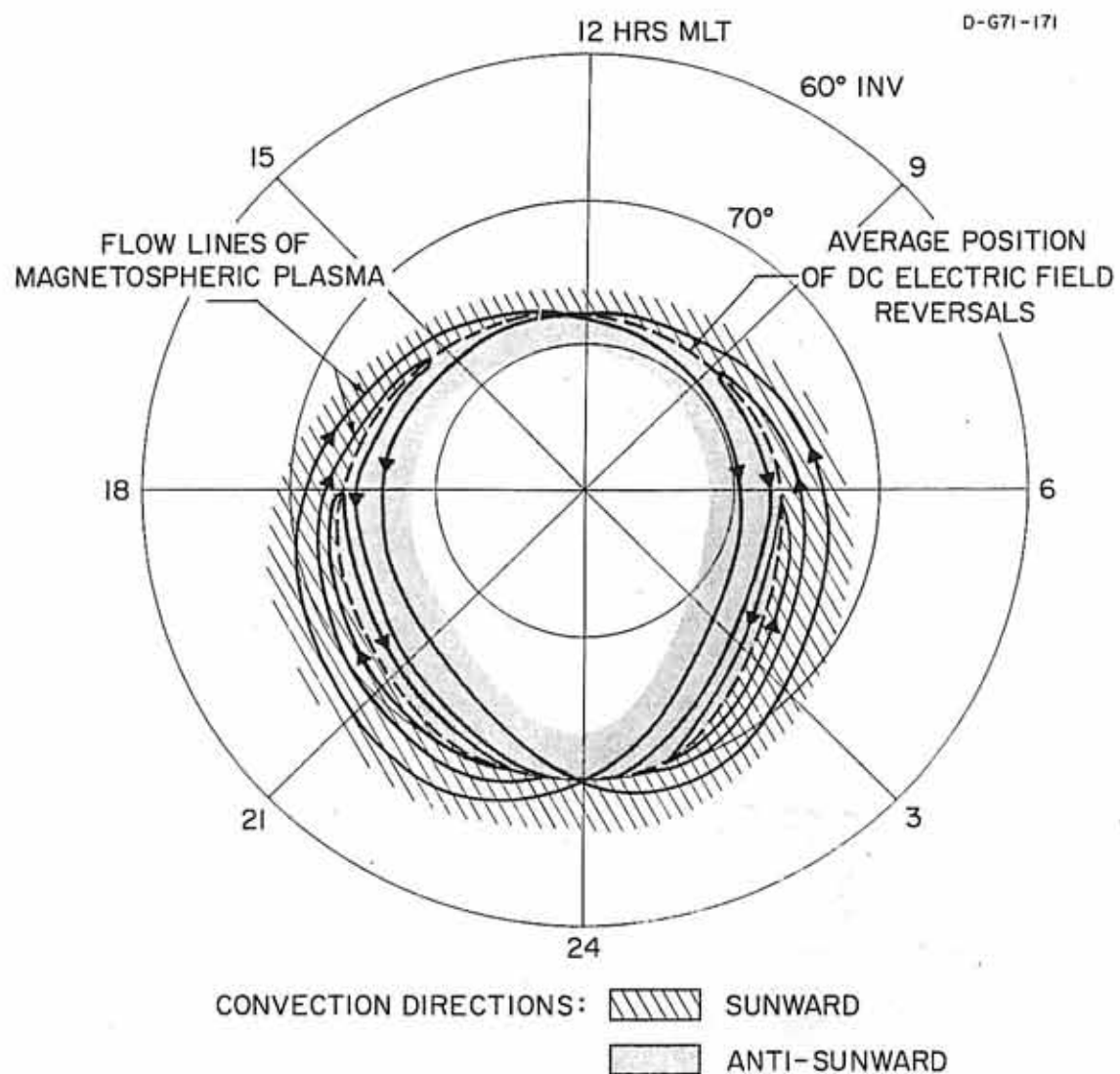


Figure 37

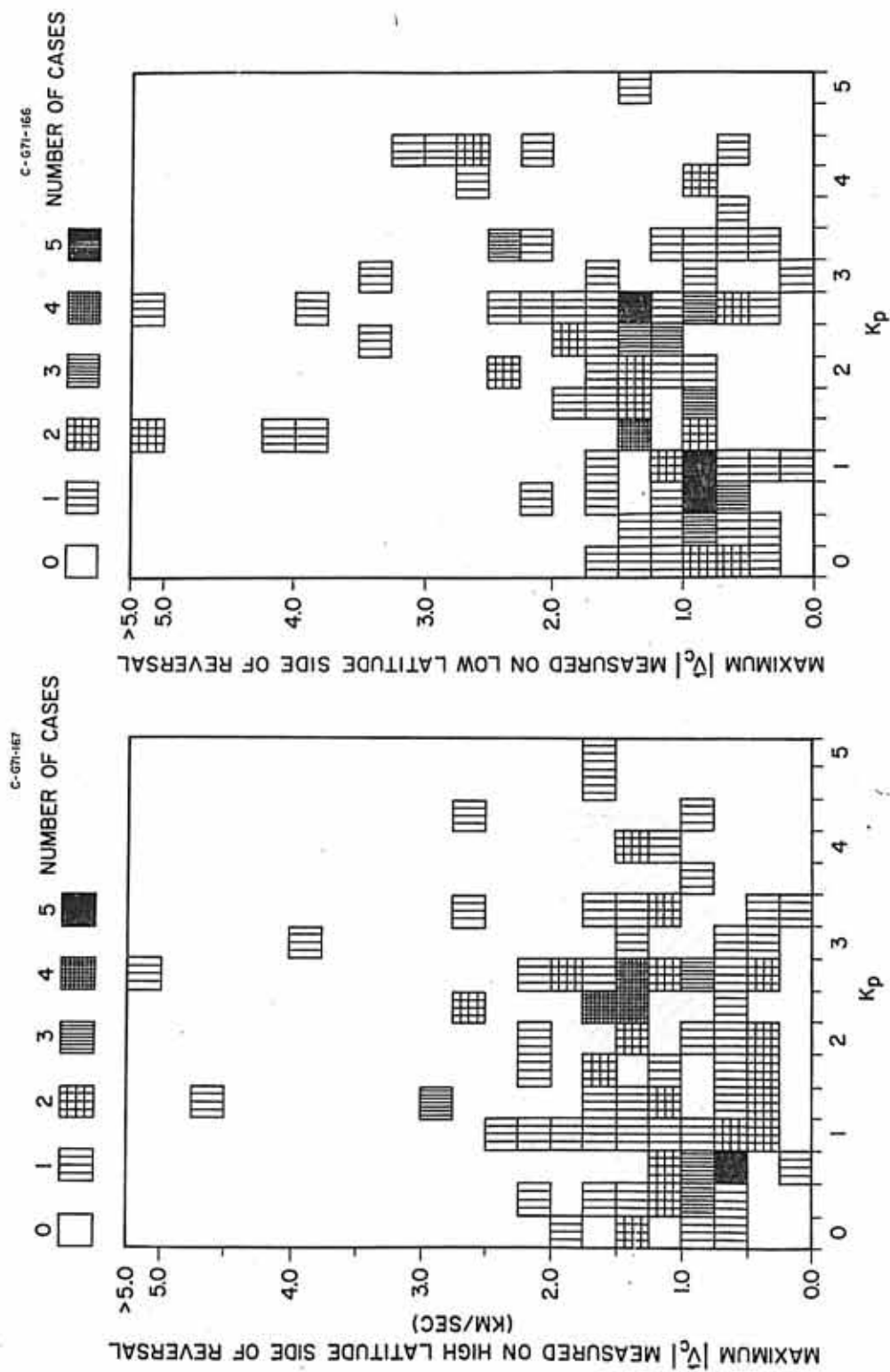
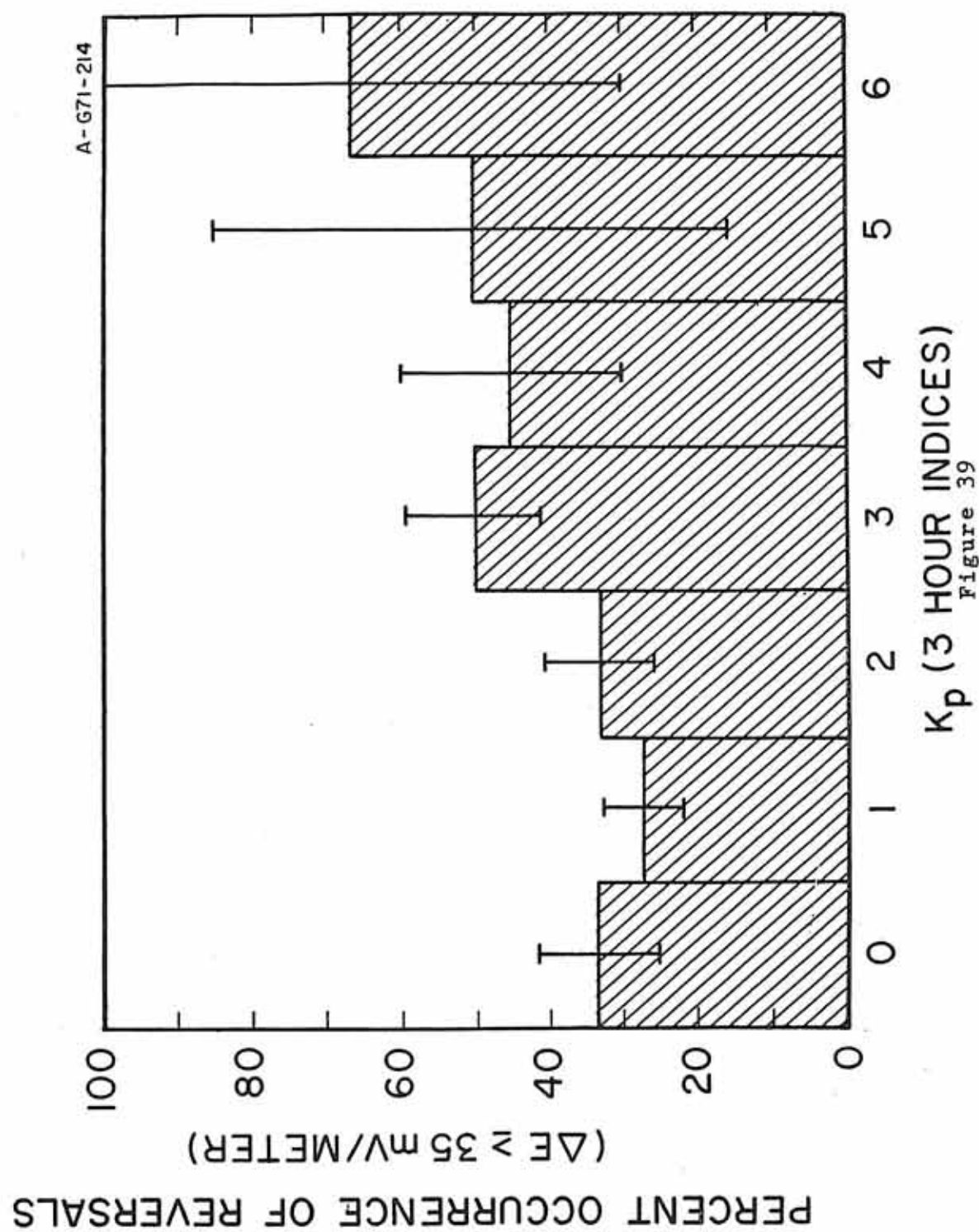
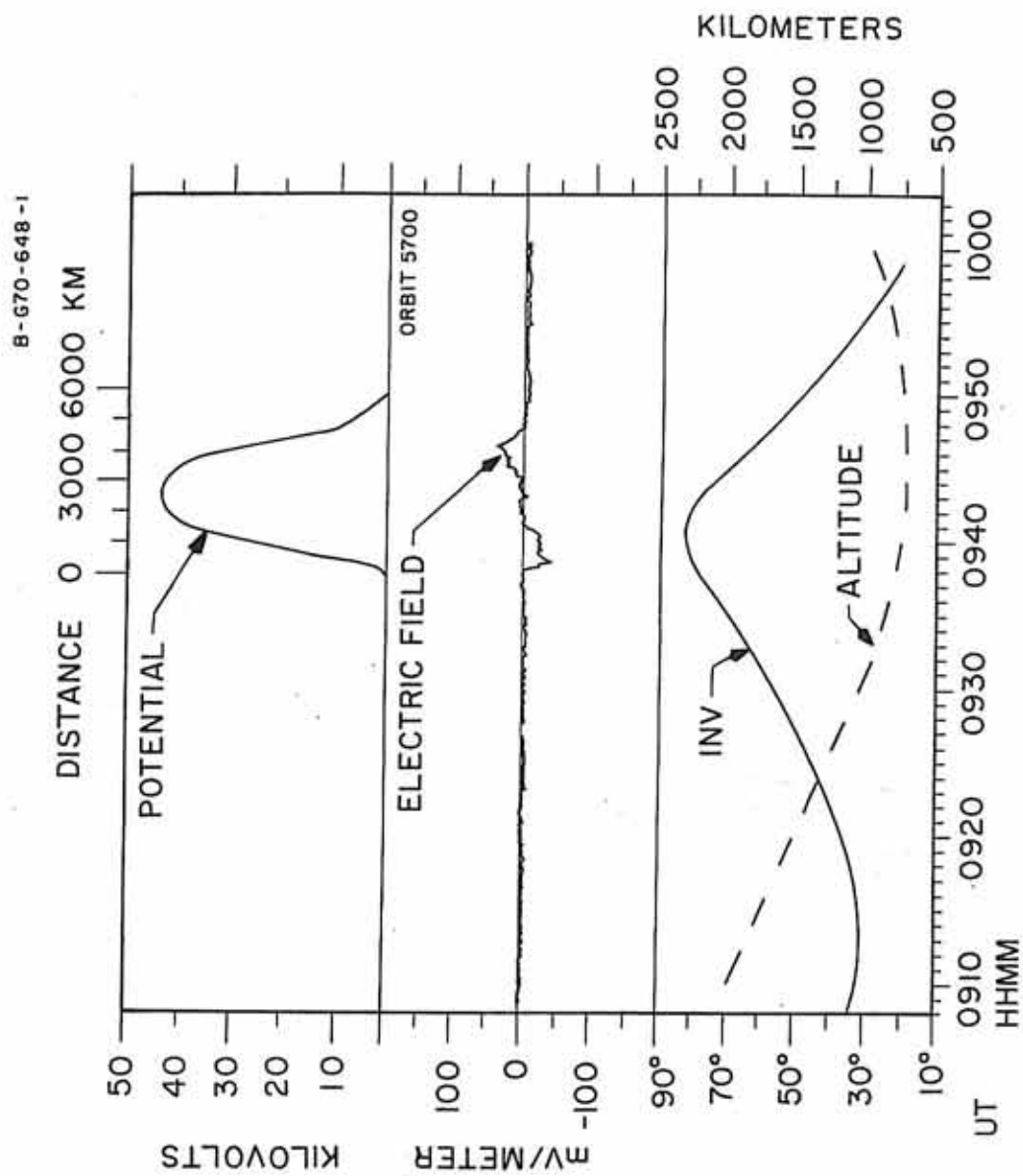


Figure 38





MLT ~ 6.6 HRS MLT ~ 18.6 HRS

$K_p = 1-; K_p \text{ SUM} = 8$

SOUTHERN HEMISPHERE NOV. 20, 1969
Figure 40

B-G70-664-1

12 HRS MLT ORBIT 5700

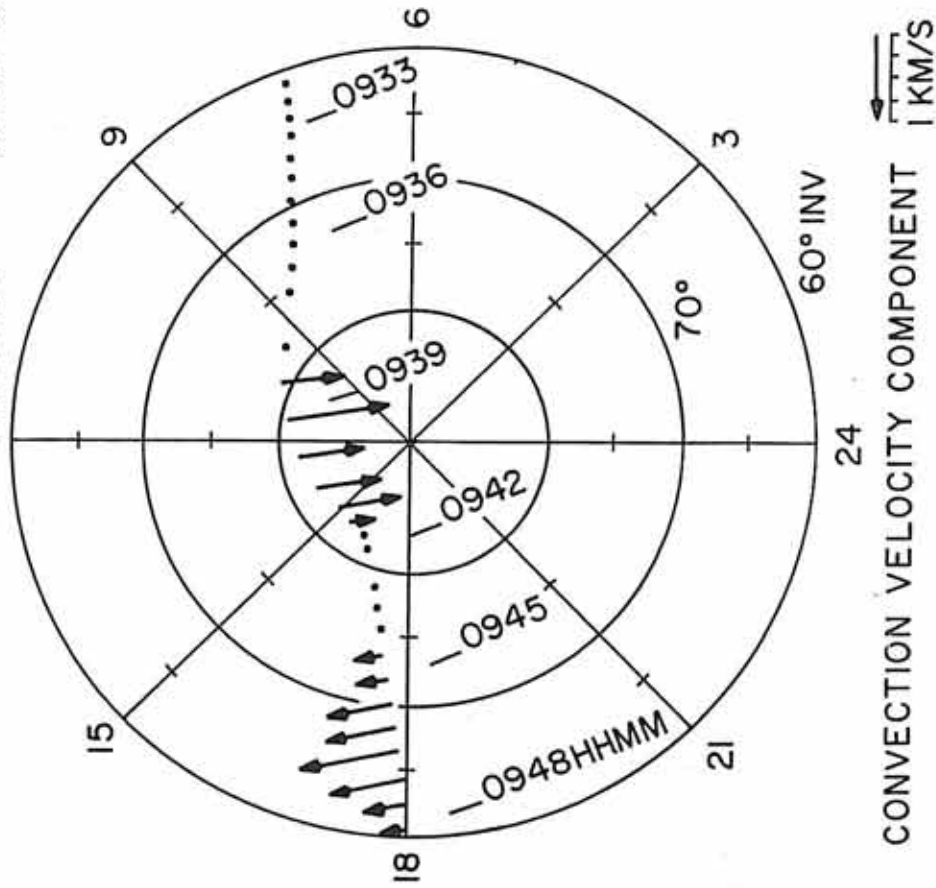
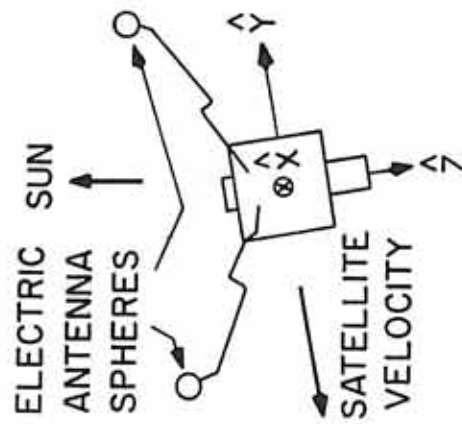


Figure 41

INJUN 5 ORIENTATION
(NON-ROTATING)



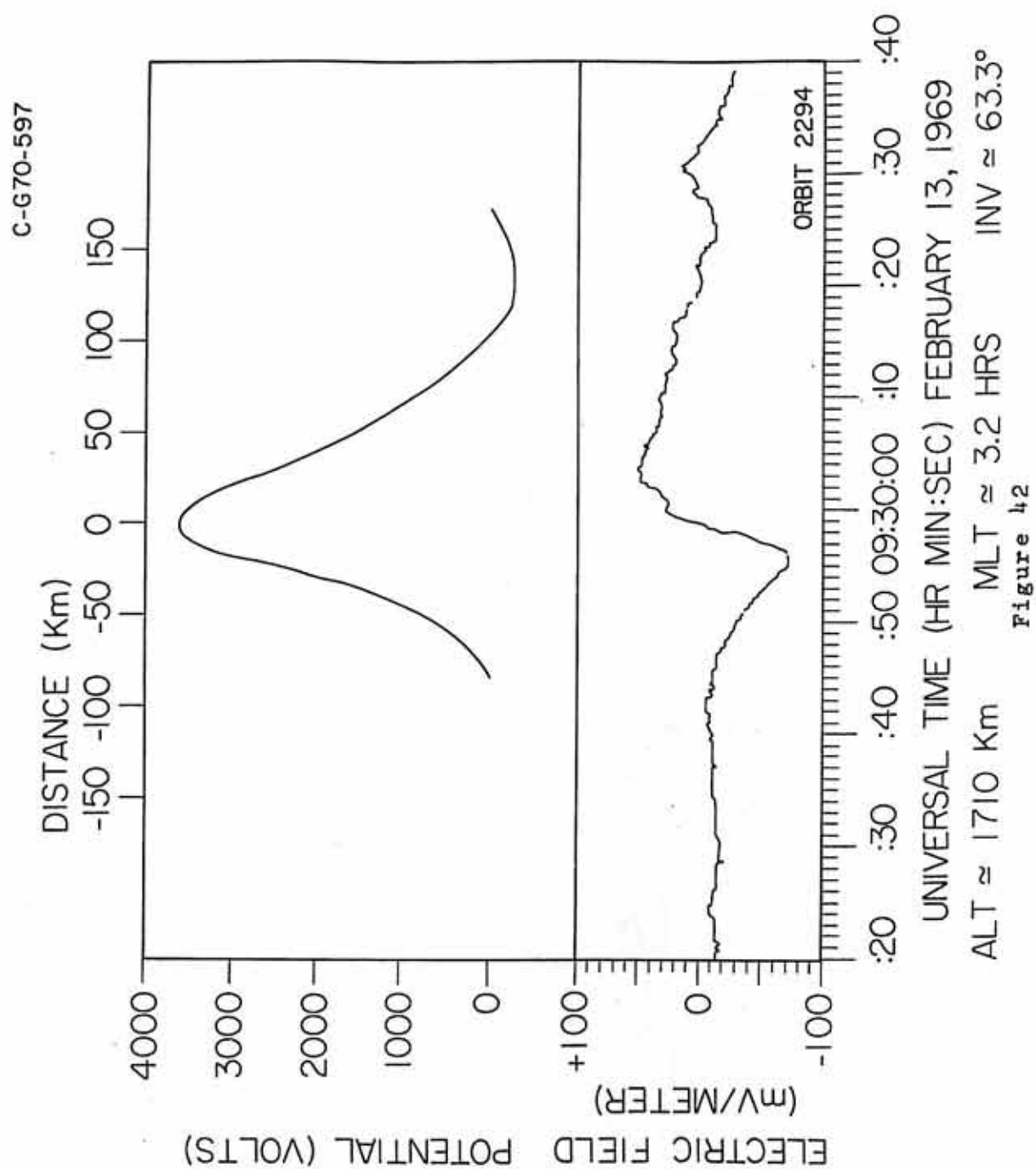
SOUTHERN HEMISPHERE

NOVEMBER 20, 1969

ALTITUDE ~ 750 KM

$K_p = 1-$

$K_p \text{ SUM} = 8, M$



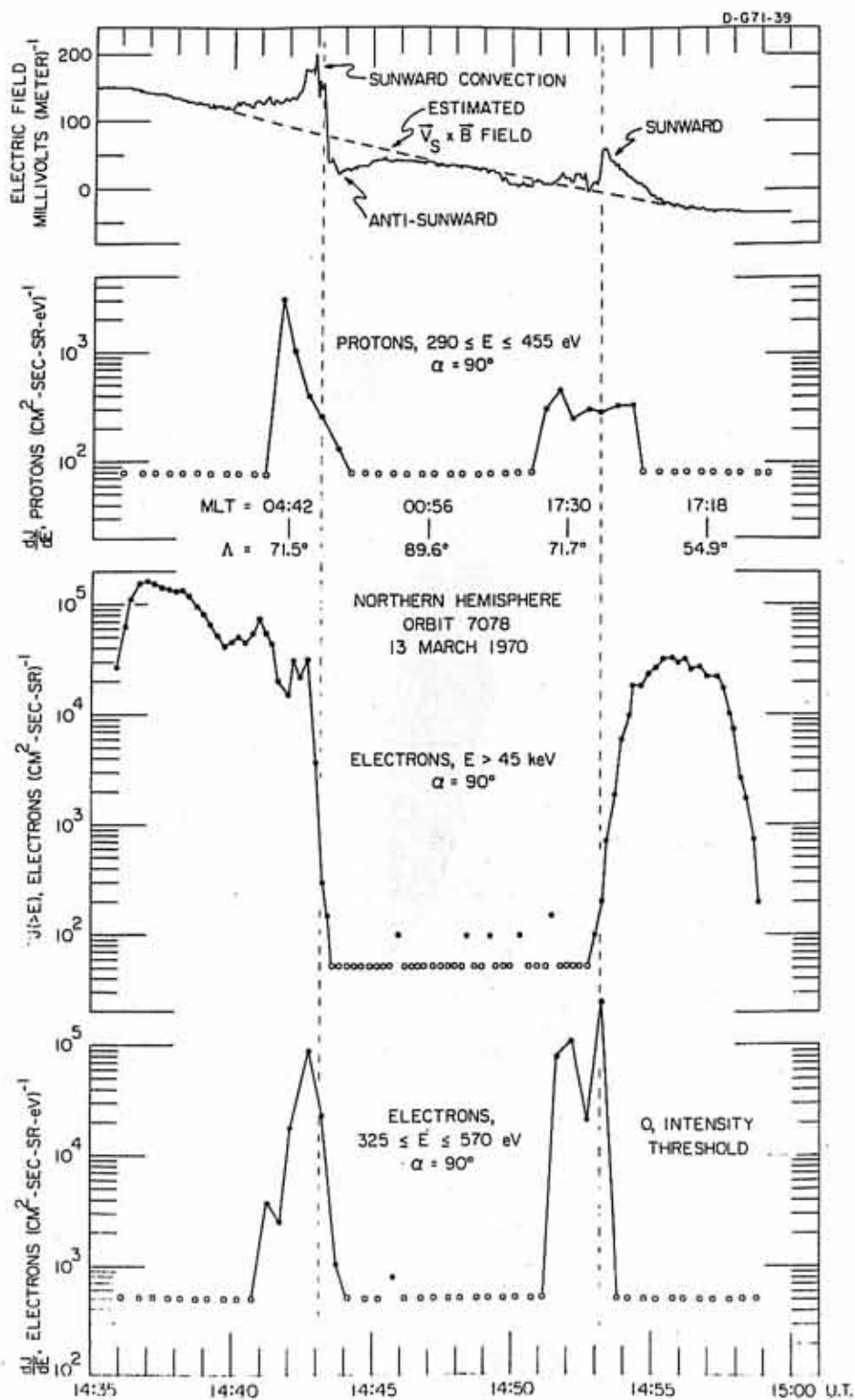


Figure 43

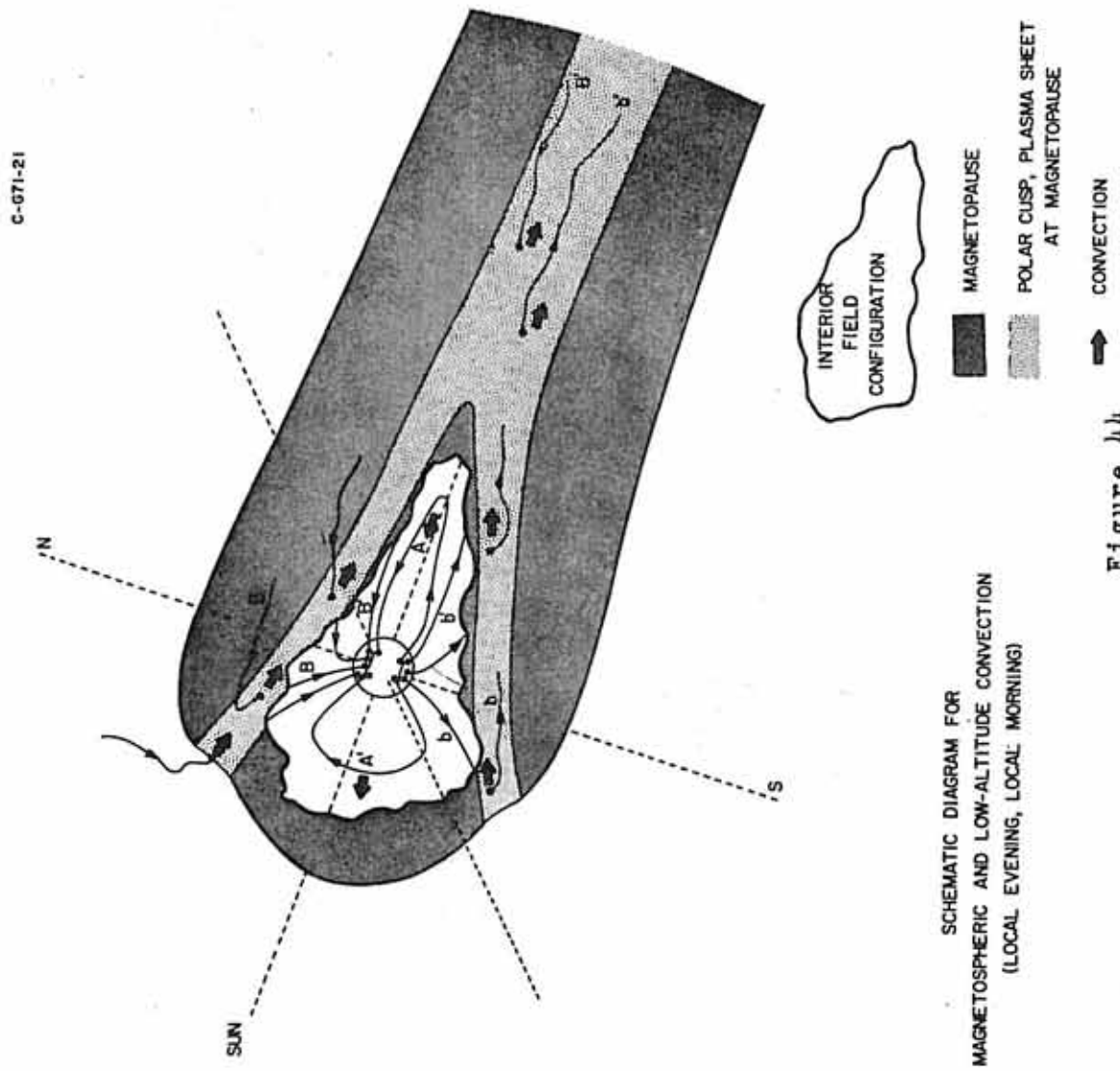


Figure 44